11175

NATIONAL LIBRARY
OTTAWA

CANADA

BIBLIOTHÈQUE NATIONALE
OTTAWA

NAME OF AUTHOR.....John...K....Walker.....

TITLE OF THESIS.....Model....Studies....of.....
..Auroral....Current....Systems
.....

UNIVERSITY....of....Alberta.....

DEGREE FOR WHICH THESIS WAS PRESENTED....Ph..D.....

YEAR THIS DEGREE GRANTED.....1972.....

Permission is hereby granted to THE NATIONAL LIBRARY OF CANADA to microfilm this thesis and to lend or sell copies of the film.

The author reserves other publication rights, and neither the thesis nor extensive extracts from it may be printed or otherwise reproduced without the author's written permission.

(Signed)..J.K.Walker.....

PERMANENT ADDRESS:

.Earth....Physics..Br.
Dept...Energy, Mines & Resources
.OTTAWA.....

DATED.29..March.....1972

NL-91 (10-68)

THE UNIVERSITY OF ALBERTA

MODEL STUDIES OF AURORAL CURRENT SYSTEMS

BY

© JOHN K. WALKER

A THESIS

SUBMITTED TO THE FACULTY OF GRADUATE STUDIES AND RESEARCH

IN PARTIAL FULFILMENT OF THE REQUIREMENTS FOR THE DEGREE

OF DOCTOR OF PHILOSOPHY

DEPARTMENT OF PHYSICS

EDMONTON, ALBERTA

SPRING, 1972

UNIVERSITY OF ALBERTA

FACULTY OF GRADUATE STUDIES AND RESEARCH

The undersigned certify that they have read, and recommend to the Faculty of Graduate Studies and Research for acceptance, a thesis entitled MODEL STUDIES OF AURORAL CURRENT SYSTEMS submitted by John K. Walker in partial fulfilment of the requirements for the degree of Doctor of Philosophy.

Supervisor

Date March 28, 1972

External Examiner

ABSTRACT

Auroral current systems in the ionosphere which link with currents in the magnetosphere were studied using models constructed from observations and from expectations of the current flow. The conductivity of the ionosphere used in the current models was calculated from accurate expressions for the collision frequency. Models of the neutral atmosphere and the earth's magnetic field which enter into the collision and gyro frequencies were calculated for the time, location and conditions of an observed polar magnetic substorm and associated electric fields. The electron density was determined throughout the ionosphere from a functional dependence on the auroral brightness. Theoretical models of eight current systems driven by different electric field configurations were studied. The auroral electrojet was found to be similar to a sheet current a few hundred kilometres in width and to span the arcs. The magnitude of the electrojet depended mainly on the direction of the electric field, as well as showing a linear dependence on the conductivity of the ionosphere and the strength of the electric field. The electrojet for a polar magnetic substorm was found to be "turned on" by the electric field changing to the southwest direction and "turned off" by a slow decrease in the conductivity. The electrojet during the expansive phase of the substorm consisted of equal contributions from Pedersen and Hall currents. From current continuity requirements, field-aligned currents similar to Birkeland currents were determined for the electrojet. Meridional currents flowing across the electrojet required antiparallel currents flowing in field-aligned sheets on either side of the electrojet.

ACKNOWLEDGEMENTS

It is a pleasure to thank Drs. G. Rostoker, J.A. Jacobs and P. Serson for their guidance and assistance during this research. I am also indebted to colleagues J.L. Kisabeth, P.A. Camfield and E.I. Loomer as well as Drs. D. Russell, J.C. Sampson and A. Hruška for many stimulating discussions, helpful suggestions and support of the logistics. The financial and technical support by the Earth Physics Branch of the Department of Energy, Mines and Resources and the Institute of Earth and Planetary Physics at the University of Alberta is gratefully appreciated. The electric field data was kindly provided by Dr. F.S. Mozer. The enduring patience of my wife and family throughout this research is deeply valued.

TABLE OF CONTENTS

LIST OF ILLUSTRATIONS

CHAPTER 1

INTRODUCTION

The aurora and the currents that often flow in the upper atmosphere during the occurrence of auroral displays have been studied for several centuries but still hold many secrets. The cause of an aurora is known to be energetic electrons of a few kev; but the source of these electrons is not known, nor is the mechanism of their precipitation into the upper atmosphere. Magnetic variations have been associated with aurora since 1741 when Celsius and Hiortu independently observed a correlation between visual aurora and magnetic activity. Although the inferred current system has been extensively analyzed from magnetic observations, the driving mechanism of the auroral current system is not known, nor is the location of the complete circuit of the current system. Recently, previously unknown electric fields have been measured in the auroral ionosphere, thus permitting the calculation of auroral current systems from Ohms' law as well as from magnetic field variations. Having both magnetic field observations and electric fields with electron densities permits a cross check on the current calculation by two independent methods.

Historically, the aurora has been observed and recorded as early as the 6th century B.C. by Anaximenes, in 456 B.C. by Anaxagoras, and in 322 B.C. by Aristotle. More recently, Halley in 1715 observed the convergence of corona type of aurora and conceived of it as a flow of magnetic particles along the earth's magnetic field. In a treatise at this time, Jean Jacques d'Ortous de Mairan postulated the sun's atmosphere to extend to the earth causing the aurora and zodiacal light at

both the north and south magnetic poles which has proven to be a remarkably accurate conjecture. Graham in 1729 was the first to observe the geomagnetic variations and distinguish between disturbed and quiet periods. Birkeland (1908, 1913) determined the height of the auroral current system associated with an aurora from the analysis of its magnetic field from two stations located on either side of an arc. The height was 200 km which he thought was too high because he had not corrected for induction in the earth. Birkeland determined the magnitude and direction of the current system, speculated that its origin was tied to currents flowing in the magnetosphere, and modelled the earth and its magnetosphere in the laboratory. The extensive geomagnetic synopsis by Chapman and Bartels (1940) and recently by Akasofu (1968), treated the auroral zone current systems, their variations in space and time, and association with sunspots and aurora. An analytic expression for the east-west auroral current system having an elliptical cross section was developed by Weaver (1960). In the model of Boström (1964) currents were permitted to flow along magnetic field lines into the magnetosphere. Walker (1964) constructed equivalent current systems to determine the magnitude and flow of auroral currents from magnetic variations observed along a geomagnetic meridian, as well as over a large geographic region. However, it is impossible to determine a unique 3 dimensional current system from observations on one plane so further information is necessary. Bonnevier et al. (1970) constructed 3 dimensional models of polar magnetic substorm current systems which fit the gross features of the observed magnetic perturbation pattern. Auroral arcs resulting from the interaction of a dynamic magnetosphere

with the ionosphere are theoretically studied by Atkinson (1970). His analytic model predicts multiple thin arcs with weak electric fields but intense currents within the arcs. Walker (1964) has inferred ionospheric currents covering broad regions, however, analysis at present has not been able to determine if these large current systems consist of many confined currents.

The sequence of events leading to an aurora and finally to auroral currents of approximately 10^6 amperes is a complicated, partially understood chain of plasma phenomena with origins on the sun. Individual auroral storms are associated with sunspots and so called M active regions on the sun, and lag behind these by approximately 1.5 days. At the time of the flare sudden ionospheric disturbances and magnetic crochets occur on the day side of the earth owing to X rays increasing the D region ionization (Figure 1.1). The enhanced flow of solar plasma further compresses the earth's magnetic field configuration causing first an abrupt change (recognized as a sudden commencement on magnetograms) followed by an increase in the magnetic field within the earth's magnetosphere. Some of the solar plasma enters the magnetosphere and eventually flows toward the earth along the neutral sheet which forms in the antisolar direction from the compression and distortion of the earth's polar magnetic field (Axford and Hines, 1961). Particle densities, energies and magnetic and electric fields have all been observed to change by a factor of 10 or more with the onset of a storm. The storm plasma penetrates the dayside magnetosphere to about 4 Re (earth radii) and then circles anticlockwise around the earth causing an electric field, possibly a ring current, and an asymmetric inflation and collapse

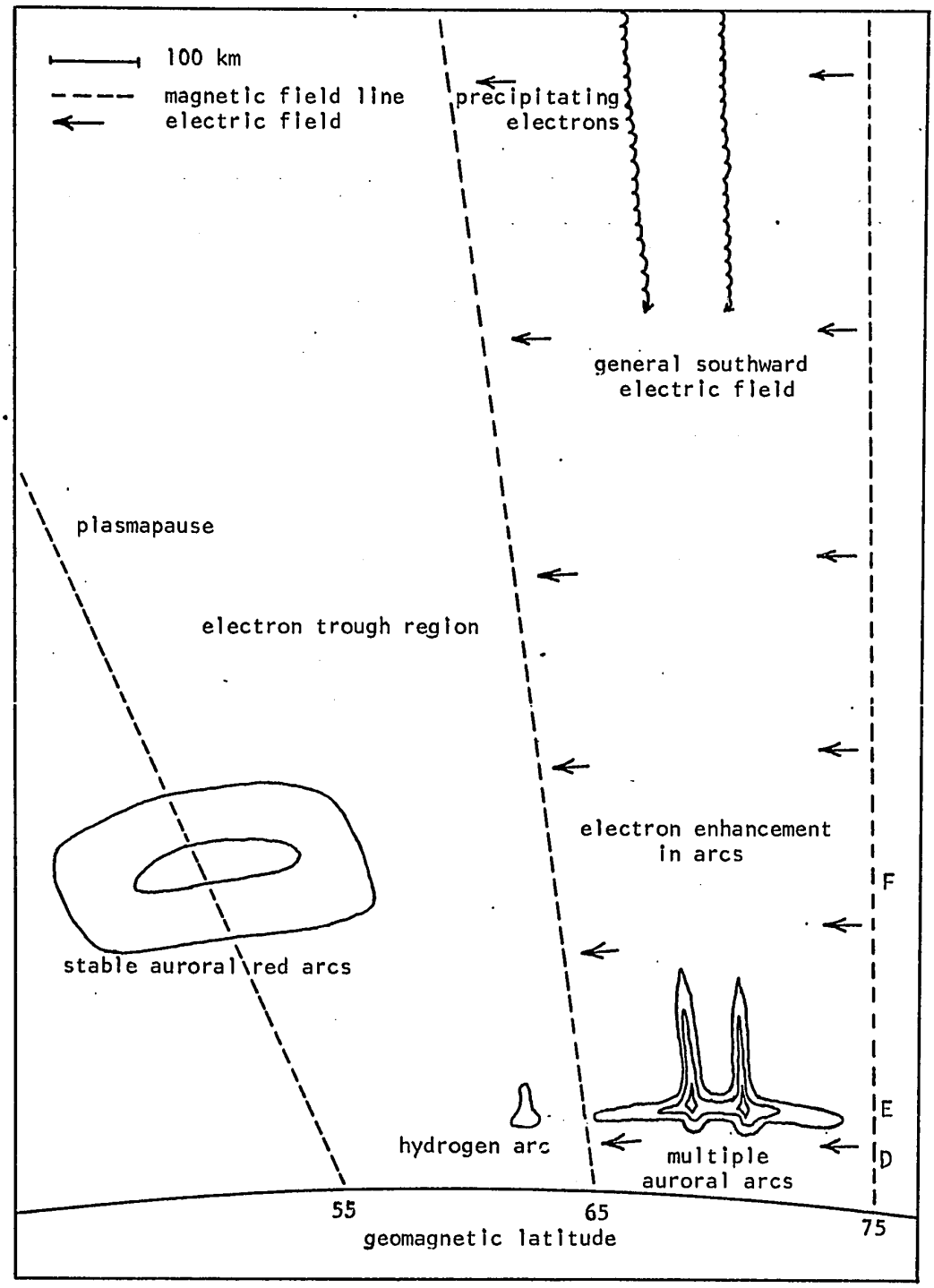

Figure 1.1 A typical meridional cross section of the auroral zone showing the magnetic field lines at 55°, 65° and 75°; contours of relative brightness for multiple arcs of 50 kR(kilorayleighs) and the stable midlatitude auroral red arcs of 2kR; the electric field and the D, E, and F regions of the ionosphere.

of the magnetic field at the antisolar meridian. (Lezniak and Winckler, 1970). Some of the plasma is trapped in the earth's magnetic field; while some is precipitated into the auroral zone atmosphere where the energetic particles excite and ionize the neutral particles, causing the aurora. The general morphology of the aurora follows from quiet steady arcs at approximately 67° invariant latitude before local midnight, which are approximately 10 km wide and 500 km long, to rapid expansion and finally break up into auroral patches after midnight. Associated with the aurora are polar magnetic substorms which have a duration of approximately 1 hour and recurrence frequency of 0.5 to 2 hours (Akasofu and Chapman, 1967; Akasofu, 1968). The auroral particles have energies of a few kev and have probably been accelerated. Proton aurora may occur on the equatorial side of the arcs while high stable auroral red arcs of the oxygen band at λ6300 occur at 55° invariant latitude (Figure 1.1).

The electron density in the ionosphere is increased by factors of 10^2 to 10^4 in the region due to the auroral ionization. The increased electron density enhances the conductivity by a similar amount and facilitates current flow. The auroral electrojet flows in this region, their magnetic perturbation pattern appearing as polar magnetic substorms. The return flow of the electrojet has two possible paths; one in the ionosphere along the polar cap and mid-latitude zones and the other along field lines to the magnetosphere. The two return current systems have similar magnetic perturbation patterns and are difficult to distinguish between using magnetic observations. Magnetic analysis of the current system is further complicated by the integrating feature of a magnetic field from other

nearby sources such as ring current, magnetopause and magnetospheric undulations, field aligned currents, and induction effects. These complications combined with the rapid temporal and spatial variations of a typical auroral event have hindered complete analysis of the electrojet current system. Further, magnetic field analysis of the electrojet cannot distinguish between adjacent parallel currents separated by less than 100 km, which precludes the possibility of ascertaining whether or not line currents are associated with multiple arcs, which are generally 40 km apart. Rocket borne magnetometers flown through multiple arcs might be capable of resolving the currents but the measurements are also ambiguous because of the compounding effect of the spatial variations of the earth's field, the spatial and temporal undulations of the electrojet, and possible field aligned currents. Satellites have the same limitations as ground based observations as well as the restraints of rocket measurements, but have the advantage of being able to measure (detect) field aligned currents.

The calculation of auroral currents from Ohm's law requires a model of the ionosphere electron density and the electric field. The auroral zone electron density can be measured by ionospheric sounders for quiet diffuse faint auroral glows but must be measured by rockets or calculated from measurements of the auroral brightness for bright arcs. The location of the arcs can be determined to within about 1 km and thus the electron density has a similar spatial resolution. The electric field needs to be known only in the horizontal plane because the vertical magnetic field lines in the auroral zone are essentially equipotentials. The electric field appears to have continuous random

variations throughout the ionosphere except immediately within an arc where it has been observed to be lower at times. The electric field can be measured by satellites, rockets, balloon-borne probes or by observing the motion of barium clouds released by rockets above 200 km. The magnitude and direction of the current distribution can then be calculated throughout the ionosphere from observationsof the electron density and electric field and compared with the equivalent line current calculated from magnetic field variations. The vertical electric field cannot be measured because it is below the threshold of present detectors, however the vertical current can be solved by assuming divergence free conditions. The location of the field aligned currents in relation to the aurora and their magnitude are possibly keyed to the physics and driving mechanism of the aurora, and the plasma dynamics in the magnetosphere. The model current systems can be used to study the possible driving mechanism of the auroral electrojet and the relative importance of different electric field configurations. The model current systems can also be used to study the several hypotheses of the auroral electrojet and the contributions of the different currents to the whole system of currents and to the observed magnetic field variations. The effect of the currents heating the upper atmosphere and current induced winds changing the dynamics of the upper atmosphere are significant and possibly contribute to weather patterns.

Computer programs were developed incorporating many of the variables which affect the currents as well as determining the currents' effect on the upper atmosphere and magnetic field observations. The computer programs can be used for studying theoretical systems of current models and for constructing models to fit a set of observations.

CHAPTER 2

CURRENT CALCULATION

Balfour Stewart in 1882 first suggested the upper atmosphere had a significant conductivity because of the correlation of sunspot activity with the daily geomagnetic variation. The ionization density in the upper atmosphere was first deduced by Appleton. In 1927 Pedersen showed that the magnetic field of the earth made the electrical conductivity of the upper atmosphere anisotropic. Cowling in 1933 showed that in the presence of a magnetic field $\vec{B}$ and a transverse electric field $\vec{E}$, a Hall current also flows in the direction $\vec{B} \times \vec{E}$. The conductivity is thus a second order tensor and the current density, $\vec{j}$, is given by the following expression (when the magnetic field is in the -z direction).

$$\vec{j} = \overleftrightarrow{\sigma}.\vec{E} = \begin{pmatrix} \sigma_1 & \sigma_2 & 0 \\ -\sigma_2 & \sigma_1 & 0 \\ 0 & 0 & \sigma_0 \end{pmatrix}.\vec{E} \qquad (2.1)$$

where σ_1 = Pedersen conductivity; σ_2 = Hall conductivity. The coordinate system is x east, y north, and z vertically up. The inclination of the magnetic field is a function of latitude and longitude, and in the auroral zone the field is inclined approximately 12° to the vertical. For currents flowing along horizontal layers, the conductivity needs to be rotated to this plane as calculated by Matsushita (1967); however the currents flowing between the ionosphere and magnetosphere follow the magnetic field lines so the specific conductivity, σ_0, does not

need to be altered. The error from not rotating the tensor is then only in the horizontal components and amounts to $\frac{1}{\sin 78}$ or 2% which is insignificant compared to the uncertainty in the electron density and electric field.

2.1 Conductivity

The expressions for the 3 conductivities in an anisotropic weakly ionized plasma are given by Chapman (1956) for the frequency-independent case. The more generalized frequency-dependent expressions must be considered for events or pulsations with a frequency above 0.1 Hz. These expressions are derived by Watanabe (1962) and are,

$$\sigma_0 = e^2\Sigma_r\left\{\frac{n_r\nu_r}{m_r(w^2+\nu_r^2)} + \frac{i\, n_r\, w}{m_r(w^2+\nu_r^2)}\right\} \tag{2.2}$$

$$\sigma_1 = e^2\Sigma_r\left\{\frac{n_r\nu_r}{m_r}\ \frac{\nu_r^2+\omega_r^2+w^2}{(\nu_r^2+\omega_r^2-w^2)^2+4\nu_r^2\, w^2} + \frac{in_r^2w(\omega_r^2-\nu_r^2-w^2)}{m_r(\nu_r^2+\omega_r^2-w^2)^2+4\nu_r^2w^2}\right\} \tag{2.3}$$

$$\sigma_2 = e^2\Sigma_r\left\{\frac{n_r\omega_r k}{m_r}\ \frac{\nu_r^2+\omega_r^2-w^2}{(\nu_r^2+\omega_r^2-w^2)^2+4\nu_r^2w^2} - \frac{2in_rk\ \nu_r\omega_r}{m_r(\nu_r^2+\omega_r^2-w^2)^2+4\nu_r^2\, w^2}\right\} \tag{2.4}$$

$$k = \begin{cases} +1 \text{ for e, - ions} \\ -1 \text{ for + ions} \end{cases} \qquad r = e, -, + \text{ ions}$$

where e is the electron charge, n is the number density of the r^{th} species given in section 2.4, ν_r is the collision frequency discussed in section 2.3, m_r is the mass, ω_r the gyrofrequency outlined in the next section, and w is the signal frequency. The International System

of Units (SI) and prefixes are generally used. The expressions for the conductivity are only approximate; ideally the calculation should be performed for each constituent in the ionosphere such as O^+, NO^+, e, and negative ions. However, the height distribution and composition of the ions in the ionosphere is not sufficiently known to warrant such an onerous computation. The composition of the neutral atmosphere is known as a function of height and must be included in the calculation of the collision frequency. Negative ions should also be included in the conductivity calculation since they contribute to the night time D region of the ionosphere. The interrelation of the conductivity and the current to the aurora, the magnetic field and the magnetosphere plasma is depicted in Figure 2.1 and discussed in the following sections.

2.2 Gyrofrequency

The gyrofrequency, ω_r, used in the expressions for the conductivity, is the angular speed with which the charges spiral around the lines of magnetic force and is given by,

$$\omega_r = \frac{eB}{m_r} \tag{2.5}$$

where B is the magnetic field strength. The negative and positive ion mass is assumed to be equal to the neutral mass and is calculated from the mean molecular weight which is a function of height. A more accurate calculation would involve the individual ions which have unknown height distributions for even quiet ionosphere conditions. The magnetic field is calculated from the International Geomagnetic Reference Field (IGRF) spherical harmonic coefficients as a function

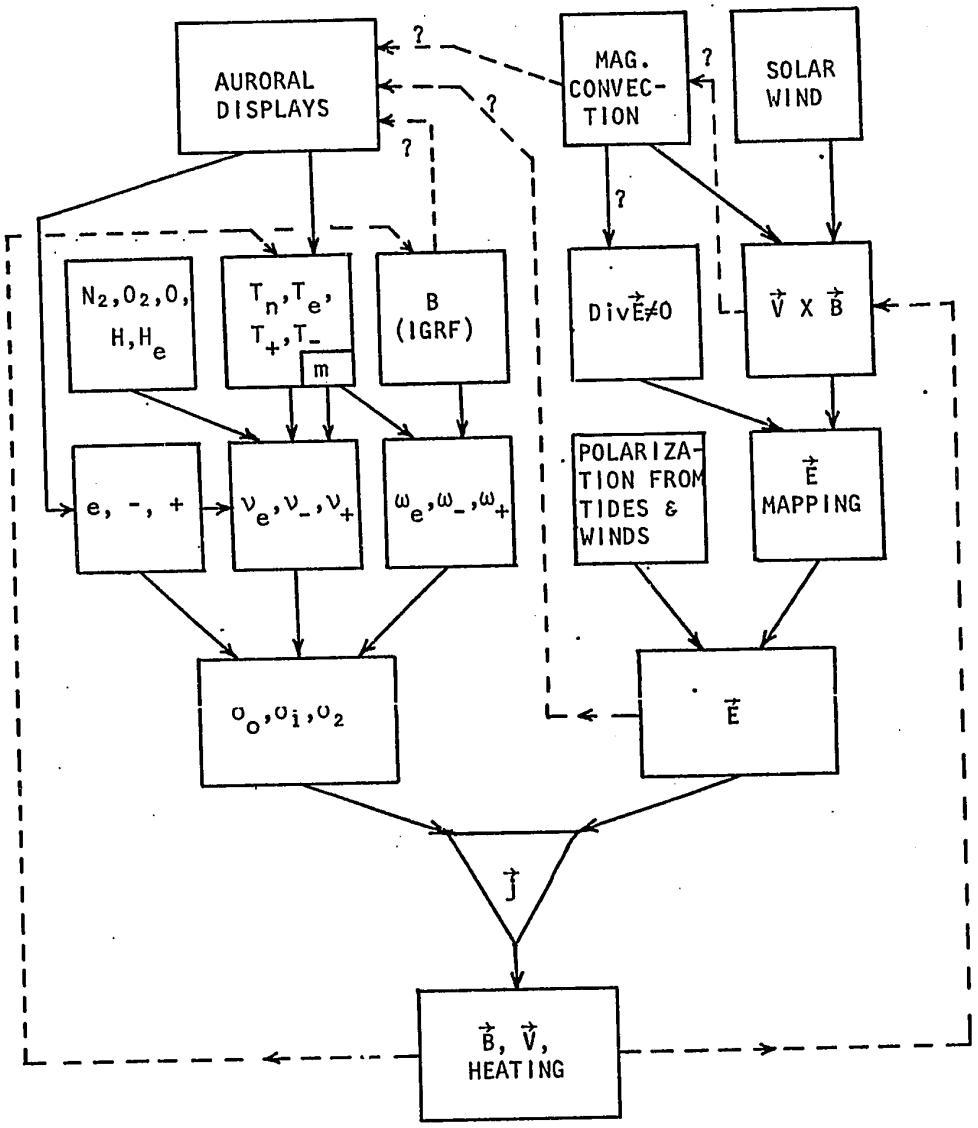

Figure 2.1 Dependence of the auroral electrojet on ionosphere and magnetosphere phencmena. Symbols are explained in the text.

of latitude, longitude, height, and epoch. The components of the magnetic field can be calculated to better than 1% for any location within about 5 R_e. The components in the present coordinate system are,

$$B_x = - \frac{1}{R \sin\theta} \frac{\partial V}{\partial \lambda} \tag{2.6}$$

$$B_y = \frac{1}{R} \frac{\partial V}{\partial \theta} \tag{2.7}$$

$$B_z = - \frac{\partial V}{\partial R} \tag{2.8}$$

$$B = (B_x^2 + B_y^2 + B_z^2) \tag{2.9}$$

where $$V = R \sum_{n=1}^{\infty} \left(\frac{R_e}{R}\right)^{n+1} \sum_{m=o}^{\bar{n}} P_n^{\bar{m}}(\cos\theta)(g_n^{\bar{m}} \cos m\lambda + h_n^{\bar{m}} \sin m\lambda)$$

R is the distance, θ is the latitude, λ is the longitude, $P_n^m(\cos\theta)$ is the Schmidt function of degree n and order m, and g_n^m and h_n^m are the IGRF coefficients. The mass of electrons is much less than any of the ions so the angular speed of the electrons in the ionosphere is much greater than that for ions by a factor of approximately 4×10^4.

2.3 Collision Frequency

The collision frequencies are important parameters in the calculation of the conductivity, but are difficult to calculate accurately because of the uncertainty in the momentum transfer cross section. The collisions for different types of encounters involve varying kinds of interacting forces as well as temperature and energy dependence. Electrons and ions collide with each other and with neutral particles, as in the following expressions,

$$\nu_e = \nu_{en} + \nu_{e+} + \nu_{e-} + \nu_{ee} \tag{2.10}$$

$$\nu_+ = \nu_{+n} + \nu_{+-} + \nu_{++} + \nu_{+e} \tag{2.11}$$

$$\nu_- = \nu_{-n} + \nu_{--} + \nu_{-+} + \nu_{-e} \tag{2.12}$$

where e, +, - and n are electrons, positive and negative ions, and neutrals. The ion collision frequency with electrons are insignificant because of the much greater ion mass. The negative ion collision frequency term ν_{--} can also be neglected because of the low number density of negative ions in the D and E region of the ionosphere. The neutral composition of the upper atmosphere is known; thus the interacting force and momentum transfer cross section for the electron-neutral and ion-neutral collision frequency can then be calculated for each constituent of the upper atmosphere,

$$\nu_{en} = \Sigma_{i=1}^{m} \nu_{ei} \qquad i = \text{atmosphere constituent}$$

$$\nu_{+n} = \Sigma_{i=1}^{m} \nu_{+i}$$

2.3.1 Electron Collision Frequency

The collision frequency between an electron and one of the atmosphere's constituents involves the relative velocity of the particles and the cross sections of the particles. The average collision frequency is of the form (Banks, 1966),

$$\nu_{12} = \frac{4}{3} n_2 \, g \, Q_{e,n}$$

where n_2 is the number density of the neutrals, g is the Maxwellian average relative velocity between the two particles, and Q is the average momentum transfer cross section for thermal nonequilibrium conditions. Expanding to include the thermal nonequilibrium cases, the electron neutral collision frequency is given by,

$$\nu_{12} = \frac{4}{3} n_2 \left(\frac{8k}{\pi}\right)^{\frac{1}{2}} \left(\frac{T_1}{m_1} + \frac{T_2}{m_2}\right)^{\frac{1}{2}} Q \qquad (2.13)$$

where k is the Boltzmann constant. For the case of electrons (m_e) and ions (m_i) in the ionosphere $\frac{T_e}{m_e} >> \frac{T_2}{m_2}$ and the equation is then $\frac{4}{3}$ larger than Chapman's (1956) expression for the electron neutral collision frequency which is,

$$\nu_{en} = 5.4 \times 10^{-10} \, n \, T_e^{\frac{1}{2}} \qquad (2.14)$$

While Dalgarno (1961) used the expression,

$$\nu_{en} = 1.5 \times 10^{-11} n T_e \tag{2.15}$$

Wagner (1968) used a more refined expression from Möhlmann for the electron neutral collision frequency which is,

$$\nu_{en} = \frac{1}{2} nQ \left| \frac{8kT_e}{\pi m_e} \right|^{\frac{1}{2}} + \left[\left| \frac{n}{2} Q \right|^2 \frac{8kT_e}{\pi m_e} \right.$$

$$\left. + nQ \frac{m}{m_e} \beta \left| \frac{2}{\sqrt{\pi}} - 1 \right| \left| \frac{8kT_e}{\pi m_e} \right|^{\frac{1}{2}} \right]^{\frac{1}{2}}$$

where $Q = 5.09 \times 10^{-16} \text{ cm}^2$

$$\beta = 1.6 \times 10^{-8} \pi^{3/2} n_e \tag{2.16}$$

The collision frequencies calculated for these expressions have been plotted in Figure 2.2a. The cross sections for the momentum transfer differ for each constituent and are a function of temperature. The number density of the constituents and the ratios vary with height in the ionosphere so this should be accounted for in the calculation of the collision frequency. Figure 2.2 b shows the average momentum transfer cross section for electrons with the neutral constituents of the upper atmosphere (Banks, 1966). The collision frequency for each of the constituents is given by (Banks, 1966). The cross sections

have an experimental uncertainty of less than 20%.

$$N_2: \quad \nu_e = 2.33 \times 10^{-11}\, n(N_2)[1-1.21 \times 10^{-4} T_e]T_e$$

$$O_2: \quad \nu_e = 1.82 \times 10^{-10}\, n(O_2)[1+3.6 \times 10^{-2} T_e^{\frac{1}{2}}]T_e^{\frac{1}{2}}$$

$$O: \quad \nu_e = 2.8 \times 10^{-10}\, n(O)T_e^{\frac{1}{2}}$$

$$H: \quad \nu_e = 4.5 \times 10^{-9} n(H)[1-1.35 \times 10^{-4} T_e]T_e^{\frac{1}{2}}$$

$$He: \quad \nu_e = 4.6 \times 10^{-10} n(He)T_e^{\frac{1}{2}} \qquad (2.17)$$

The electron neutral collision frequency is the sum of the individual collision frequencies and is plotted in Figure 2.2a for comparison with the collision frequency expressions of Chapman, Dalgarno and Möhlmann. The expressions are quite similar but the Bank's values are about 20% less than Chapman's or Dalgarno's expressions.

The electron-ion collision frequency can also be simplified by using the condition $\frac{T_e}{m_e} >> \frac{T_i}{m_i}$ which occurs in the ionosphere, giving the collision frequency (Banks, 1966),

$$\nu_{ei} = (34 + 4.10 \log_{10}\left\{\frac{T_e^3}{n}\right\}) \frac{n}{T_e^{3/2}} \qquad (2.18)$$

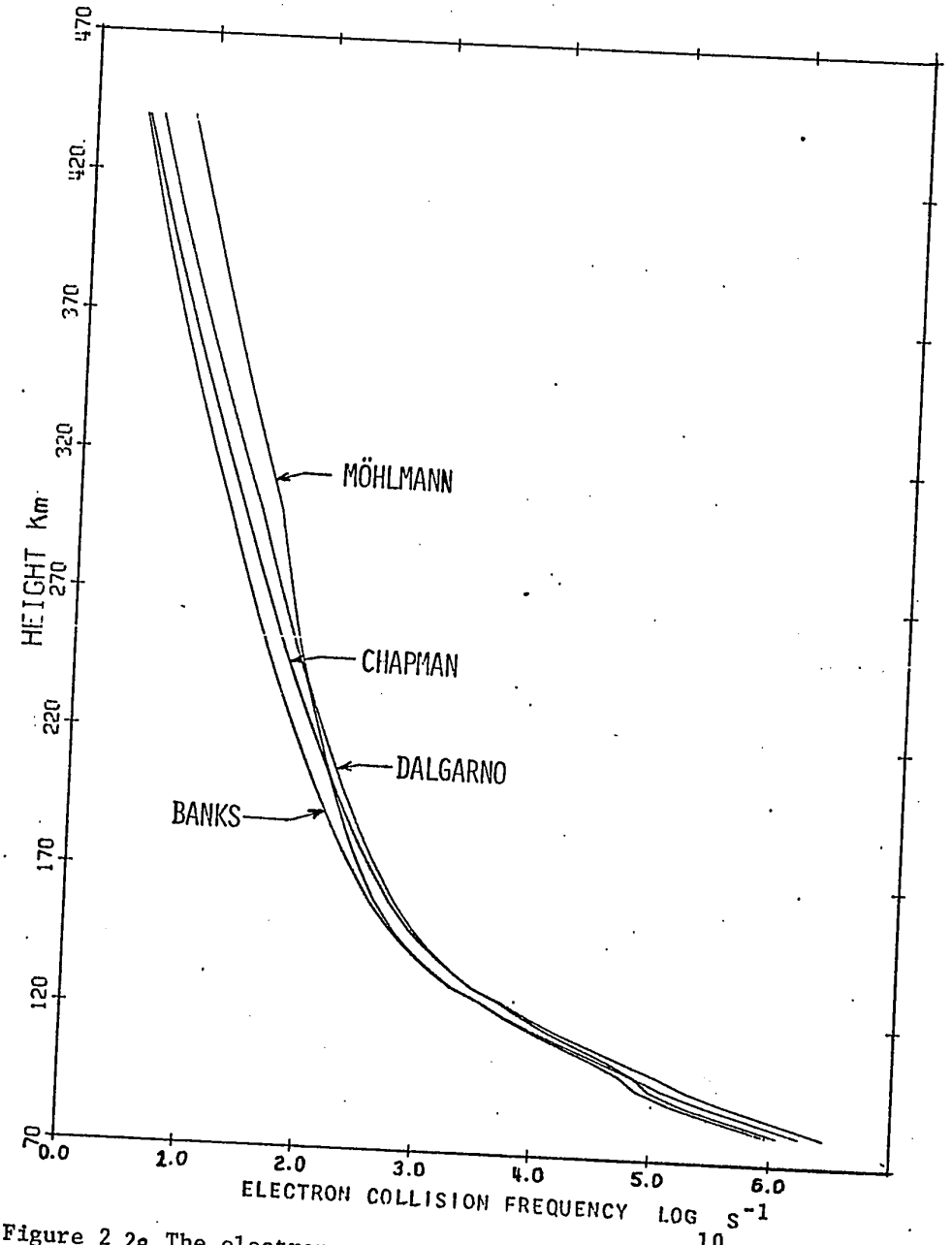

Figure 2.2a The electron neutral collision frequency for various expressions mentioned in the text.

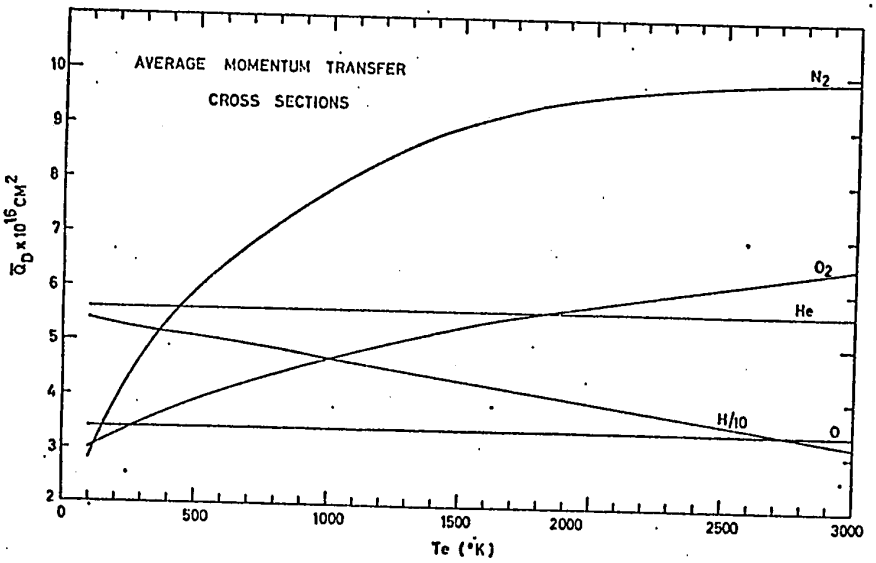

Figure 2.2b The average momentum transfer cross section for electrons with the neutral constituents of the upper atmosphere (after Banks, 1966).

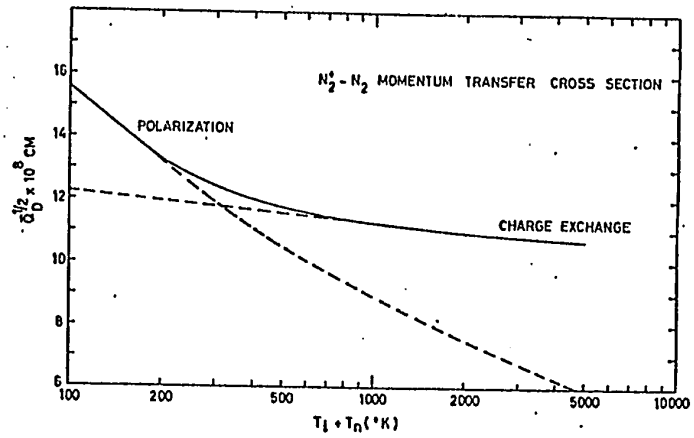

Figure 2.2c The momentum transfer cross section for $N_2^+ - N_2$ collisions showing the transition from polarization dominance below 300°K to that of charge exchange above 700°K (after Banks, 1966).

Experimental observations have confirmed the accuracy of this expression to within 6%.

The collision frequency for electrons with electrons is a similar expression or it can be expressed in terms of the electron ion collision frequency as,

$$\nu_{ee} = \left(\frac{m_i}{m_e}\right)^{1/2} \left(\frac{T_i}{T_e}\right)^{3/2} \nu_{ei} \qquad (2.19)$$

2.3.2 Ion Collision Frequency

Banks (1966) discusses the collision frequency for elastic ion-neutral and ion-ion collisions for conditions of gaseous thermal nonequilibrium. For ions, there also exists a second method of energy loss by means of resonance charge exchange. The resonant collision cross sections have been summarized by Banks (1966). The ion neutral collision frequency (Rees and Walker, 1968) is given by,

$$\nu_{in} = \frac{4}{3} \frac{\mu_{in}}{m_i} n \left(\frac{8k}{\pi}\right)^{1/2} \left(\frac{T_i}{m_i} + \frac{T_n}{m_n}\right)^{1/2} Q_{in} \qquad (2.20)$$

where $\mu_{in} = \dfrac{m_i \, m_n}{m_i + m_n}$ is the reduced mass and Q_{in} is the velocity average momentum transfer cross section.

Two methods of energy loss for ions in collision with neutrals exist, firstly, by elastic collisions, and secondly, by resonance charge exchange between ions and their parent neutral particles. At low temperatures the ion-neutral interaction is from an induced dipole attraction causing the neutral atom to become polarized, while at high

temperatures the polarization contribution is negligible so that the collision frequency varies as $T^{\frac{1}{2}}$. For the nonresonant interactions Qin was taken as 8×10^{-15} cm^2 (Dalgarno, 1961).

Charge exchange between two colliding ions and parent molecules enhances the momentum transfer cross section and becomes the dominant effect at temperatures above ~500°K (Figure 2.2c). The momentum transfer cross section for $N_2^+ - N_2$ collisions is shown to illustrate the dominance of the polarization effect below 300°K and the transition to the charge exchange region above 700°K. Banks (1966) gives the expressions pertaining to the ion and parent neutral particles in the upper atmosphere for resonance momentum transfer collision frequency,

where $\Gamma = T_i + T_n$

H^+,H	$\Gamma > 470°K$	$\nu = 1.9 \times 10^{-12}\, n\,(H)\, \Gamma^{\frac{1}{2}}(14.4 - 1.15 \log_{10} \Gamma)^2$
O^+,O	$\Gamma > 470°K$	$\nu = 4.7 \times 10^{-13}\, n\,(O)\, \Gamma^{\frac{1}{2}}(10.5 - 0.67 \log_{10} \Gamma)^2$
	$\Gamma < 470°K$	$\nu = 8.6 \times 10^{-10}\, n\,(O)$
N^+,N	$\Gamma > 550°K$	$\nu = 5.2 \times 10^{-13}\, n\,(N)\, \Gamma^{\frac{1}{2}}(10.3 - 0.64 \log_{10} \Gamma)^2$
	$\Gamma < 550°K$	$\nu = 1.0 \times 10^{-9}\, n\,(N)$
H_e^+,H_e	$\Gamma > 100°K$	$\nu = 8.7 \times 10^{-13}\, n\,(H_e)\Gamma^{\frac{1}{2}}(11.6 - 1.04 \log_{10} \Gamma)^2$
O_2^+,O_2	$\Gamma > 1600°K$	$\nu = 3.4 \times 10^{-13}\, n\,(O_2)\Gamma^{\frac{1}{2}}(10.6 - 0.76 \log_{10} \Gamma)^2$
	$\Gamma < 1600°K$	$\nu = 8.2 \times 10^{-10}\, n\,(O_2)$
N_2^+,N_2	$\Gamma > 340°K$	$\nu = 3.6 \times 10^{-13}\, n\,(N_2)\Gamma^{\frac{1}{2}}(14.2 - 0.96 \log_{10} \Gamma)^2$

(2.21)

The expression developed by Chapman (1956) for the ion-neutral collision frequency is,

$$\nu_{in} = 2.6 \times 10^{-9} \frac{n}{M^{\frac{1}{2}}} \qquad (2.22)$$

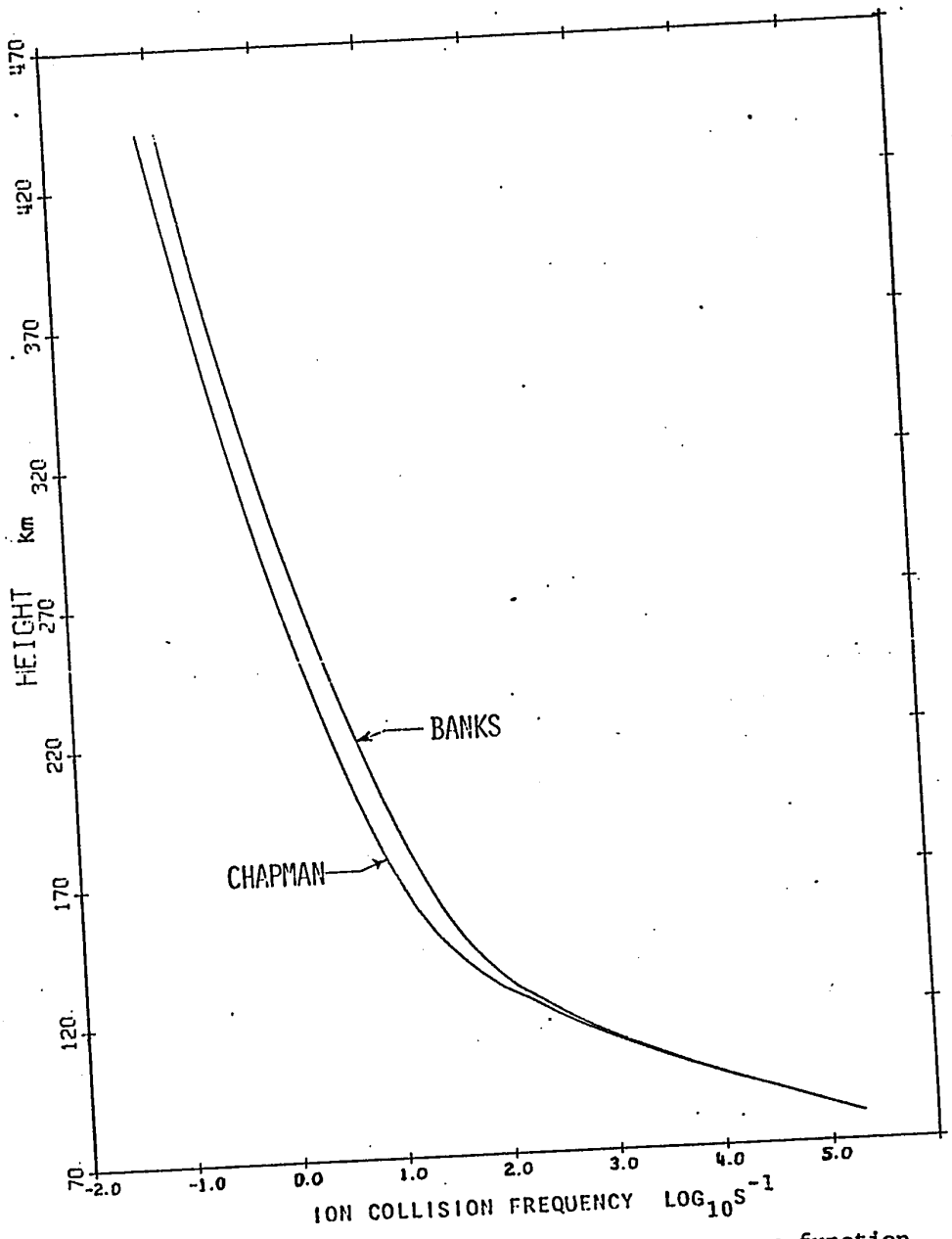

Figure 2.3 The ion neutral collision frequency as a function of height for the expressions of Chapman and of Banks.

where M is the mean ion and neutral mass expressed in A.M.U. The final values for an ion neutral collision frequency calculated from the expressions of Banks and Chapman are shown in Figure 2.3. They are nearly the same to 120 km but the collision frequency is approximately 50% greater at 160 km for the calculations from Banks' expression.

For the ion-ion collision frequency all the ions were assumed to have the same temperature but the mass was assumed equal to that of the neutral particles. The ion temperature, T_i, discussed in Section 2.6, was calculated independently from thermal equilibrium between the electrons and neutrals. The ion-ion collision frequency is given by Hochstim (1969),

$$\nu_{ii} = \frac{4}{3}(2\pi)^{\frac{1}{2}} n_i \left(\frac{e^2}{kT_i}\right)^2 \left(\frac{kT_i}{m_i}\right)^{\frac{1}{2}} \ln \Lambda \qquad (2.23)$$

where $$\Lambda = \frac{kT}{e^2}$$

The positive ion with negative ion collision frequency, ν_{+-}, is small because of the number density of negative ions; however, the negative ion with positive ion, ν_{-+}, and the positive ion with positive ion, ν_{++}, is significant because of the higher positive ion density. The collision frequency of negative ions and neutral particles was calculated from equation 2.22, to complete the calculation of the ion collision frequencies.

2.4 The Atmosphere

The expressions for the collision frequency are dependent on the number density of the neutral particles and their temperature. The neutral atmosphere is a complex function of the diurnal, seasonal, latitudinal, and solar variations. The seasonal variation at 60° latitude and auroral heights of 110 km is 70% greater in the winter, and 30% less during summer, than the United States standard atmosphere. The temperature of the exosphere varies from 700°K to 1800°K from quiet to active solar conditions (Figure 2.4a), which causes the specific conductivity to vary by a factor of 5. The diurnal variation of the thermopause temperature is approximately 500°K with the maximum being in the local afternoon. Variations in the density occur with temperature changes because the atmosphere is in mechanical equilibrium. Density variations have also been correlated with magnetic activity.

An atmosphere appropriate to the location and time of the auroral event must thus be calculated to obtain reasonable values for the conductivities. A neutral atmosphere density and temperature height profile is seldom, if ever, obtained simultaneously with the ionospheric electron density and electric field observations, so a model must be constructed. The computer program of Pitts (1968) was used for the calculation of the earth's atmosphere with modifications to calculate the exospheric or thermopause temperature from solar flux, magnetic activity and diurnal expressions, or from satellite observations. The model atmosphere is calculated from a temperature and mean molecular weight profile with boundary conditions such as at the earth's surface. The model is self-consistent, based on the equation of state and the assumption of mechanical equilibrium.

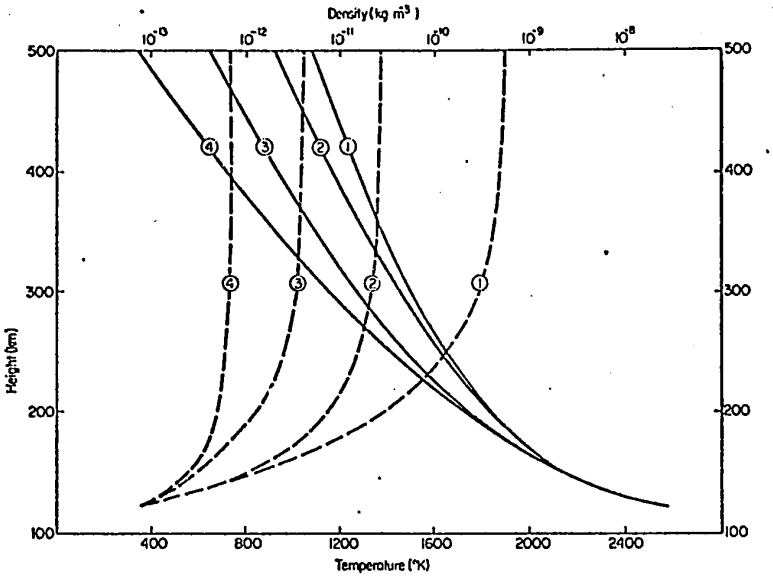

Fig. 2.4a Cospar International Reference Atmosphere (1965). Vertical distribution of density and temperature for high solar activity (10 cm solar flux $S = 250$) at noon (1) and midnight (2); and for low solar activity ($S = 75$) at noon (3) and midnight (4). These models assume the pressure, composition, and temperature at 120 km to be invariant.

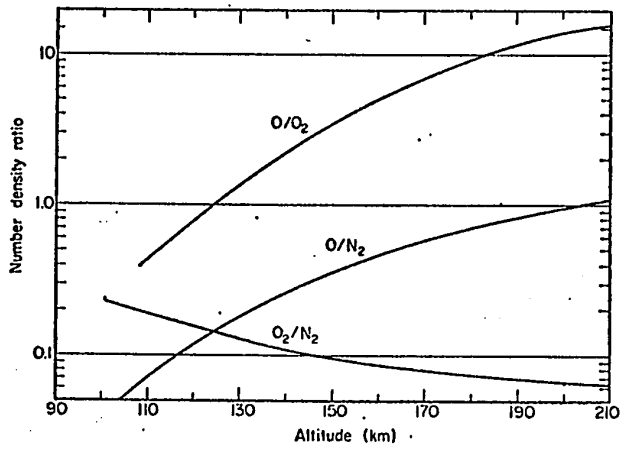

Fig. 2.4b Ratios of the concentrations of the major neutral constituents of the upper atmosphere as functions of altitude [after Nier *et al.* (1964)].

The atmosphere of a planet can be defined by the density ρ, pressure P, temperature T, and molecular weight M, as well as the acceleration due to gravity g and height z. The equations which relate these are the equation of state,

$$\rho = \frac{PM}{RT} \tag{2.24}$$

and mechanical equilibrium,

$$\frac{\partial P}{\partial z} = -\rho g \tag{2.25}$$

where R is the universal gas constant.

The temperature is generally known as a function of height so the equation of state is substituted in the last equation, following Pitts (1968), giving,

$$\frac{\partial P}{\partial z} = -\frac{PM}{RT}\, g \tag{2.26}$$

The variables M, T and g are functions of height which can be reduced to two variables by reducing the height z, to a geopotential height H, and the temperature to a molecular scale temperature. The geopotential altitude is,

$$dH = \frac{g}{g_o}\, dz \tag{2.27}$$

where g_o = acceleration of gravity at earth's surface and is given by $g_o = 978.0496\ (1+0.0052934\ \sin^2\phi - 0.0000059\ \sin^2 2\phi)$, ϕ = latitude.

The acceleration due to gravity at a height z is then,

$$g = \frac{g_o \ R_e}{(R_e + z)} \tag{2.28}$$

where R_e = earth's radius

and thus the geopotential height, H, becomes,

$$H = R_e^2 \int_0^z \frac{dz}{(R_e + z)^2} = \frac{z \ R_e}{R_e + z} \tag{2.29}$$

The temperature and molecular weight can also be reduced to one variable by the molecular scale temperature, T_m,

$$T_m = \frac{Mo}{M} \ T \tag{2.30}$$

where M_o is the molecular weight at the earth's surface. Substitution into equation 2.26 gives,

$$\frac{1}{P} \ \frac{\partial P}{\partial z} \ dz = \frac{-M_o \ g_o \ dH}{RT_m} \tag{2.31}$$

If $\frac{\partial T}{\partial H}$ is constant then solutions of the following forms are possible, going from height a to b,

$$P_b = P_a \left[\frac{T_{mb}}{T_{ma}} \right]^{\frac{g_o M_o}{R \frac{\partial T_m}{\partial H}}} \quad \text{for} \quad \frac{\partial T_m}{\partial H} \neq 0 \qquad (2.32)$$

$$P_b = P_a \exp \left[\frac{-g_o M_o (H_b - H_a)}{R T_{ma}} \right] \quad \text{for} \quad \frac{\partial T_m}{\partial H} = 0 \qquad (2.33)$$

If the surface conditions and the molecular scale temperature as a function of height are known, then the pressure and density can be calculated as a function of height. Provision is made in the program for these calculations from the height distributions of the kinetic temperature and molecular weight. Linear interpolation between the data points of the temperature, molecular scale temperature, and molecular weight observations is performed at 1 km intervals for the calculation of the atmosphere parameters.

The atmosphere no longer behaves hydrostatically in the exosphere so Pitts (1968) calculates the density in terms of the density at the base of the exosphere by an elaborate analytic expression.

The thermopause temperature is a function of solar activity, seasonal and diurnal time, and geomagnetic activity. Jacchia(1964) has developed an expression to calculate the thermopause temperature as functions of these variables. Temperature variation due to the solar cycle and solar rotation in terms of the 10.7 cm solar flux is given by,

$$T_2 = 357°K + 3.6 < F_{10.7} > + 1.8 \, (F_{10.7} - < F_{10.7} >) \qquad (2.34)$$

where $\langle F_{10.7} \rangle$ is the solar flux averaged over the last 2 or 3 solar rotations.

and $F_{10.7}$ is the solar flux one day delayed.

The temperature due to semiannual variation is given by,

$$T_3 = T_2 + (0.37 + 0.14 \sin 2\pi \frac{D-151}{365}) \langle F_{10.7} \rangle \sin 4\pi \frac{D-59}{365} \quad (2.35)$$

where D is the day of the year from 1st January. The variation in the exospheric temperature with the 3 hour geomagnetic Ap index is given by,

$$T_4 = T_3 + 1.0 \quad Ap + 100 \ (1-\exp(-0.08\ Ap)) \quad (2.36)$$

The diurnal temperature has 3 hours maximum delay with respect to the sun's culmination and a geographic variation. The daytime and nightime temperature maximum and minimum are given by,

$$T_D = T_4(1 + 0.25 \sin^{2.5} N) \quad (2.37)$$

$$T_N = T_4(1 + 0.25 \cos^{2.5} \theta) \quad (2.38)$$

where $N = \frac{1}{2}$ (geographic latitude − solar declination)

and $\theta = \frac{1}{2}$ (geographic latitude + solar declination)

The solar declination is given by,

$$S = 23.5 \cos\left(\frac{D-192}{91}\right)$$

The temperature for any time, t, can then be calculated from,

$$T_\infty = T_N(1 + A \cos^{2.5}\frac{\tau}{2}) \qquad (2.39)$$

where $$A = \frac{T_D - T_N}{T_N}$$

and $$\tau = 15\ t - 225 + 12 \sin(15\ t - 135)$$

Having calculated P, T, ρ and M as functions of height, additional quantities are calculated such as the speed of sound, the collisional diameter, the collision frequency for the neutral particles, the mean free path and the mean particle velocity. Up to 10 gas species are used for the calculation of the molecular weight, the coefficient of viscosity, the specific weight, the pressure and density scale height, the number density, the kinematic viscosity and the columnar mass. The equations are programmed in standard fortran on the computer so that a model atmosphere can be constructed for a large range of conditions and variables but requiring a minimum amount of data and thus easy to use.

The chemical composition of the neutral atmosphere varies with height above 100 km because mixing gives way to diffusion and chemical conversion. The ratios of the major constituents do not change

significantly with time so expressions were developed to calculate the number densities of the constituents as a function of height. From the diagram of Nier et al. (1964) Figure 2.4b, the approximate ratios of oxygen to nitrogen and molecular oxygen to nitrogen are,

$$R(O/N_2) = e^{0.003(Z-110) + 0.6} \tag{2.40}$$

$$R(O_2/N_2) = e^{0.0122(Z-100) - 2.78} \tag{2.41}$$

The conservation of mass then requires,

$$n_t = n(N_2) + n(O_2) + n(O) \tag{2.42}$$

where n_t is the total number density and n(x) is the number density of the x th constituent. The equations 2.40 and 2.41 can be substituted into equation 2.42 to give the following solutions,

$$n(N_2) = \frac{n_t}{1 + R(O/N_2) + R(O_2/N_2)} \tag{2.43}$$

$$n(O) = R(O/N_2)\ n\ (N_2) \tag{2.44}$$

$$n(O_2) = R(O_2/N_2)\ n\ (N_2) \tag{2.45}$$

The number density of helium is considerably less than any of the other constituents up to 700 km, and consequently it can be calculated quite accurately from the expression of Reber and Nicolet (1965) for diffusive equilibrium as,

$$n(H_e) = \frac{n(0)^{2} + \frac{7\alpha}{3}}{C_r\, n(N_2)^{1} + \frac{4\alpha}{3}}$$

where $\alpha = -0.36$ and $C_r = 0.16$. Hydrogen becomes important only above 1800 km which is beyond the region of the aurora. The constituent number density can now be used for the electron and ion neutral collision frequency calculations in sections 2.31 and 2.32.

An event is analyzed in section 5 for which a model atmosphere was calculated. The polar magnetic substorm occurred on the night of August 3, 1969 at approximately 67° (60° north geographic latitude). Model atmosphere and ionospheres were calculated from 50° geographic to 60° geographic (the auroral zone in central Canada). The U.S. Supplemental Atmosphere (1966) for summer, 60° north, which was used for the first 80 km of the atmosphere also lists the surface boundary conditions and the percent composition of the model atmosphere. For the 80 to 120 km region, the seasonal and latitudinal variation of temperature and density in the lower thermosphere and obtained from Champion (1967). The temperature profile from 120 to 160 km was taken from the auroral N_2^+ rotational temperature profile observed by Hunten et al. (1963). The temperature profile was extrapolated from 160 km to the thermopause at 300 km, and was calculated for a 10.7 cm solar flux of 188 and an Ap of 14. The mean molecular weight is constant to 100 km then decreases gradually with height. Champion's summer model also was used for the molecular weight profile to 120 km while the model of Hinteregger et al. (1965) was used for the exosphere. The model atmosphere (Table 1) is in hydrostatic equilibrium and takes

TABLE 1

MODEL ATMOSPHERE AND IONOSPHERE FOR EARTH

MODEL = NASA18NA LATITUDE = 59° LONGTITUDE = -113° DATE 215.000, 1969

PARAMETERS AT SURFACE

Pressure	= 1010.00 mbar	Temperature	= 287.15 K	Density	= 0.12E-02 gm/cm^3
% Oxygen	= 20.947	Weight	= 29.004	Gravity	= 981.919 gm/s^2
% Hydrogen	= 0.005	% Nitrogen	= 78.084	% CO2	= 0.031
% Helium	= 0.052	% Argon	= 0.934	% Neon	= 0.182

TEMPERATURE AND MOLECULAR WEIGHT DISTRIBUTION
IONOSPHERE ELECTRONS AND ELECTRON TEMPERATURE DISTRIBUTION

Height km	Temperature K	Mole Scale Temp K	Mole Wt	Pressure mbar	Electrons/cm^3	Electron Temp K
11.0	225	225	28.96	2.311E 02	0.0	0
23.0	225	225	28.96	3.770E 01	0.0	0
32.0	238	238	28.96	1.010E 01	0.0	0
49.0	277	277	28.96	1.084E 00	0.0	0
53.0	277	277	28.96	6.671E-01	0.0	0
80.0	171	171	28.95	1.091E-02	0.0	0
85.0	161	162	28.95	4.007E-03	6.000E 02	0
90.0	161	162	28.93	1.433E-03	2.500E 03	0
95.0	178	181	28.57	5.429E-04	7.000E 03	0
100.0	195	200	28.23	2.272E-04	9.000E 03	0
105.0	234	256	27.81	1.095E-04	1.000E 04	0
110.0	285	302	27.39	6.040E-05	1.200E 04	0
115.0	348	373	27.01	3.696E-05	1.500E 04	0
120.0	411	445	26.75	2.467E-05	2.000E 04	0
125.0	478	525	26.37	1.755E-05	2.300E 04	0
130.0	525	590	25.79	1.306E-05	2.900E 04	800
135.0	585	673	25.20	1.007E-05	3.500E 04	1000
140.0	645	760	24.59	8.004E-06	4.200E 04	1500
150.0	760	914	24.09	5.408E-06	4.500E 04	1700
160.0	860	1066	23.39	3.887E-06	5.100E 04	1900
180.0	950	1241	22.20	2.210E-06	5.900E 04	2100
200.0	1040	1422	21.20	1.360E-06	7.900E 04	2200
250.0	1060	1537	20.00	4.617E-07	8.500E 04	2600
300.0	1070	1659	18.70	1.724E-07	9.500E 04	2700
325.0	1071	1706	18.20	1.085E-07	1.100E 05	2730
350.0	1072	1756	17.70	6.949E-08	1.350E 05	2700
375.0	1073	1809	17.20	4.520E-08	1.300E 05	2630
400.0	1074	1865	16.70	2.987E-08	1.200E 05	2500
500.0	1077	1928	16.20	6.177E-09	1.000E 05	2400
600.0	1080	2409	13.00	1.611E-09	8.800E 04	2200
800.0	1080	3132	10.00	2.138E-10	2.800E 04	1950
1000.0	1080	4474	7.00	5.283E-11	1.300E 04	1900

CALCULATED QUANTITIES

Height km	Temp K	Density gm/cc	Molecular Weight	Number Density per cm^3	Coll. Freq. Per Sec	Electron Density per cm^3
0	287	1.23E-03	29.004	2.55E 19	6.89E 09	-
25	228	4.27E-05	28.964	8.87E 17	2.14E 08	-
50	277	1.21E-06	28.964	2.51E 16	6.67E 06	-
75	190	5.02E-08	28.961	1.04E 15	2.30E 05	1.00E 02
100	195	3.95E-10	28.230	8.43E 12	1.91E 03	9.00E 03
120	411	1.93E-11	26.760	4.35E 11	1.46E 02	2.00E 04
130	525	7.72E-12	25.800	1.80E 11	6.99E 01	2.90E 04
140	645	3.67E-12	24.600	8.99E 10	3.96E 01	4.20E 04
150	760	2.06E-12	24.100	5.15E 10	2.49E 01	4.50E 04
160	860	1.27E-12	23.400	3.27E 10	1.71E 01	5.10E 04
170	905	8.76E-13	22.754	2.32E 10	1.26E 01	5.50E 04
180	950	6.21E-13	22.200	1.69E 10	9.48E 00	5.90E 04
190	995	4.50E-13	21.665	1.25E 02	7.29E 00	6.85E 04
200	1040	3.33E-13	21.200	9.47E 09	5.70E 00	7.90E 04
210	1044	2.62E-13	20.943	7.54E 09	4.58E 00	8.03E 04
220	1048	2.07E-13	20.695	6.03E 09	3.69E 00	8.15E 04
230	1052	1.64E-13	20.456	4.84E 09	2.98E 00	8.27E 04
240	1056	1.31E-13	20.224	3.90E 09	2.42E 00	8.39E 04
250	1060	1.05E-13	20.000	3.15E 09	1.97E 00	8.50E 04
260	1062	8.41E-14	19.722	2.57E 09	1.62E 00	8.71E 04
270	1064	6.77E-14	19.454	2.10E 09	1.33E 00	8.91E 04
280	1066	5.48E-14	19.194	1.72E 09	1.10E 00	9.11E 04
290	1068	4.45E-14	18.943	1.41E 09	9.13E-01	9.31E 04
300	1070	3.62E-14	18.700	1.17E 09	7.59E-01	9.50E 04
310	1070	2.97E-14	18.496	9.68E 08	6.33E-01	1.01E 05
320	1070	2.44E-14	18.297	8.04E 08	5.29E-01	1.07E 05
330	1071	2.01E-14	18.097	6.70E 08	4.44E-01	1.15E 05
340	1071	1.67E-14	17.896	5.60E 08	3.73E-01	1.25E 05
350	1072	1.38E-14	17.700	4.70E 08	3.14E-01	1.35E 05
360	1072	1.15E-14	17.496	3.94E 08	2.65E-01	1.33E 05
370	1072	9.54E-15	17.297	3.32E 08	2.25E-01	1.31E 05
380	1073	7.96E-15	17.097	2.80E 08	1.91E-01	1.28E 05
400	1074	5.59E-15	16.700	2.01E 08	1.39E-01	1.20E 05
450	1075	2.47E-15	16.444	9.04E 07	6.28E-02	1.09E 05
500	1077	1.12E-15	16.200	4.15E 07	2.91E-02	1.00E 05
550	1078	4.86E-16	14.411	2.03E 07	1.51E-02	9.35E 04
600	1080	2.33E-16	13.000	1.08E 07	8.47E-03	8.80E 04
650	1080	1.23E-16	12.075	6.12E 06	4.98E-03	6.38E 04
700	1080	6.81E-17	11.284	3.63E 06	3.06E-03	4.75E 04
750	1080	3.95E-17	10.599	2.24E 06	1.95E-03	3.61E 04
800	1080	2.38E-17	10.000	1.43E 06	1.28E-03	2.80E 04
850	1080	1.43E-17	9.014	9.55E 05	8.98E-04	2.27E 04
900	1080	9.05E-18	8.215	6.64E 05	6.54E-04	1.86E 04
950	1080	5.99E-18	7.555	4.78E 05	4.91E-04	1.55E 04
1000	1080	4.12E-18	7.000	3.54E 05	3.78E-04	1.30E 04

account of the known influences on the neutral atmosphere; thus it is adequate for the present analysis. A more detailed atmosphere might include dynamical aspects such as neutral winds, turbulence, solar and lunar tides, and gravity waves. These neutral atmospheric motions also transport the charge across magnetic field lines causing an electric field from the charge separation due to the $\vec{V} \times \vec{B}$ force, and consequently currents such as the Sq current system (Stening, 1970).

2.5 Auroral Zone Ionosphere

The ionosphere which extends from 60 km, the D region, to above 600 km, the F2 region, has been probed extensively by ionospheric sounders. This probe is a type of radar which obtains echoes from the ionosphere over a large frequency range giving a height versus electron density profile. The bottom side ionograms give the electron density only to successive peaks in the height profile and requires probes on the topside of the layers such as the topside of the F2 layer. The Alouette and Isis satellites have successfully studied the topside ionosphere for nearly a decade. Ionospheric sounder signals are absorbed in an aurora, thus necessitating other probe techniques. However, reflections are obtained near quiet auroral arcs which indicate electron densities up to $10^5/cm^3$ for the E region at 100 km where the auroral enhancement occurs. Rocket probes have measured electron densities in disturbed aurora but are spatially and temporally limited in the data obtained; furthermore, measurements to date can only be obtained along the trajectory of the rocket during its flight of a few minutes. The rocket and ionospheric sounder data have been of limited use for the construction

of model ionospheres for the auroral zone because little information had been obtained simultaneously on the aurora's brightness and position. Other electromagnetic wave probes are the Gordon (Thomson) scattering and partial reflection which are effective above and below 100 km respectively but require expensive installations. The electron density can also be determined from the auroral brightness volume emission rate by ion chemical equilibrium or by electron continuity equilibrium considerations. The electron density could be determined throughout a cross section by fitting an auroral arc model to the observation of the auroral brightness obtained by two station triangulation of arcs. Although the aurora and the auroral zone ionosphere have been extensively studied no observational or theoretical models of electron density in an arc and its environs are known.

The physical processes which control the ionosphere are production (q), destruction or loss (ℓ) and velocity of ionization ($\vec{V}$) which can be combined in the electron (Ne) continuity equation as follows,

$$\frac{\partial Ne}{\partial t} = q - \ell(Ne) - \text{div}\ (Ne\ \vec{V}) \qquad (2.47)$$

The production of electrons in day time is by absorption by the neutral particles of extreme ultraviolet and X-ray radiation, while at night electron production is by collisions with energetic charged particles (Belon et al., 1966; Rees, 1969). Intense ionization in arcs causes sufficient excitation which is seen as auroral emissions. The loss processes in the ionosphere are atomic,

molecular ion and electron recombination, and attachment of electrons to neutrals (Rishbeth and Garriott, 1969). Transport terms such as those from diffusion, electromagnetic drifts, or neutral winds are of less importance in the lower ionosphere over short periods of time and quiet conditions. The time for the electron density to reach equilibrium is much more rapid for an increase in the ionization rate than for a decrease such as a fading or moving arc. The ionization rate is proportional to the volume emission rate or brightness of an arc which for some aurora varies rapidly, spatially and temporally. Because the electron density is not directly proportional to the ionization rate the history of the volume emission rate is required for a complete determination of the electron density for nonsteady state conditions. The equilibrium time for the electron continuity equation is of the order of a minute when the ionization rate is increasing and twenty minutes when decreasing. Superimposed on this generally turbulent ionosphere in the immediate vicinity of arcs is a latitudinal variation in the electron density (Eather and Mende, 1971). The E region electron density is approximately a hundred times less in the midlatitude and polar cap regions. The topside F2 region has a major trough in the electron density at the equatorial edge of the auroral zone, an enhancement above the auroral zone, and a depletion in the polar cap as well as other redistributions caused by winds (Brace et al, 1970).

2.5.1 Observed Auroral Zone Ionospheres

The midlatitude side of the auroral zone night time ionosphere has a height profile shown in Figure 2.5 (43°) (Large and Wait, 1968), which was extended beyond their 250 km limit to fit the F2 layer observed by Alouette and Isis satellites for the same latitudinal regions (Chan and Colin, 1969). The stable midlatitude ionosphere abruptly changes at about 58° invariant latitude with the depletion of the electron density to form a trough above the F2 peak. The high stable auroral red arcs also occur here during auroral displays and magnetic substorms. (Norton and Findlay, 1969). The electron density in the E region and the night sky brightness (Gattinger, 1971) both apparently increase as an arc is approached as surmised from a brief study of AFCRL airborne ionospheric sounder data crossing the auroral zone. The topside ionosphere electron density also increases from the trough to about the value of the midlatitude electron density as auroral arcs are approached; however the electron density can vary by a factor of 5 at 400 km during a major auroral disturbance (Warren, 1969; Arendt, 1969). The spatial and temporal relationship between the auroral brightness and the electron density in the E layer and topside F2 layer is not known; nevertheless, it should vary with the enhanced night sky brightness. The auroral zone E layer probably begins in the vicinity of the red arcs at 58° invariant latitude with the height profile shown in Figure 2.5 (60°). An electron density profile obtained by a rocket-borne detector NASA 18:02 flown at Ft. Churchill in the middle of the auroral zone under magnetically quiet conditions with no visible aurora is also shown in Figure 2.5 (68°).

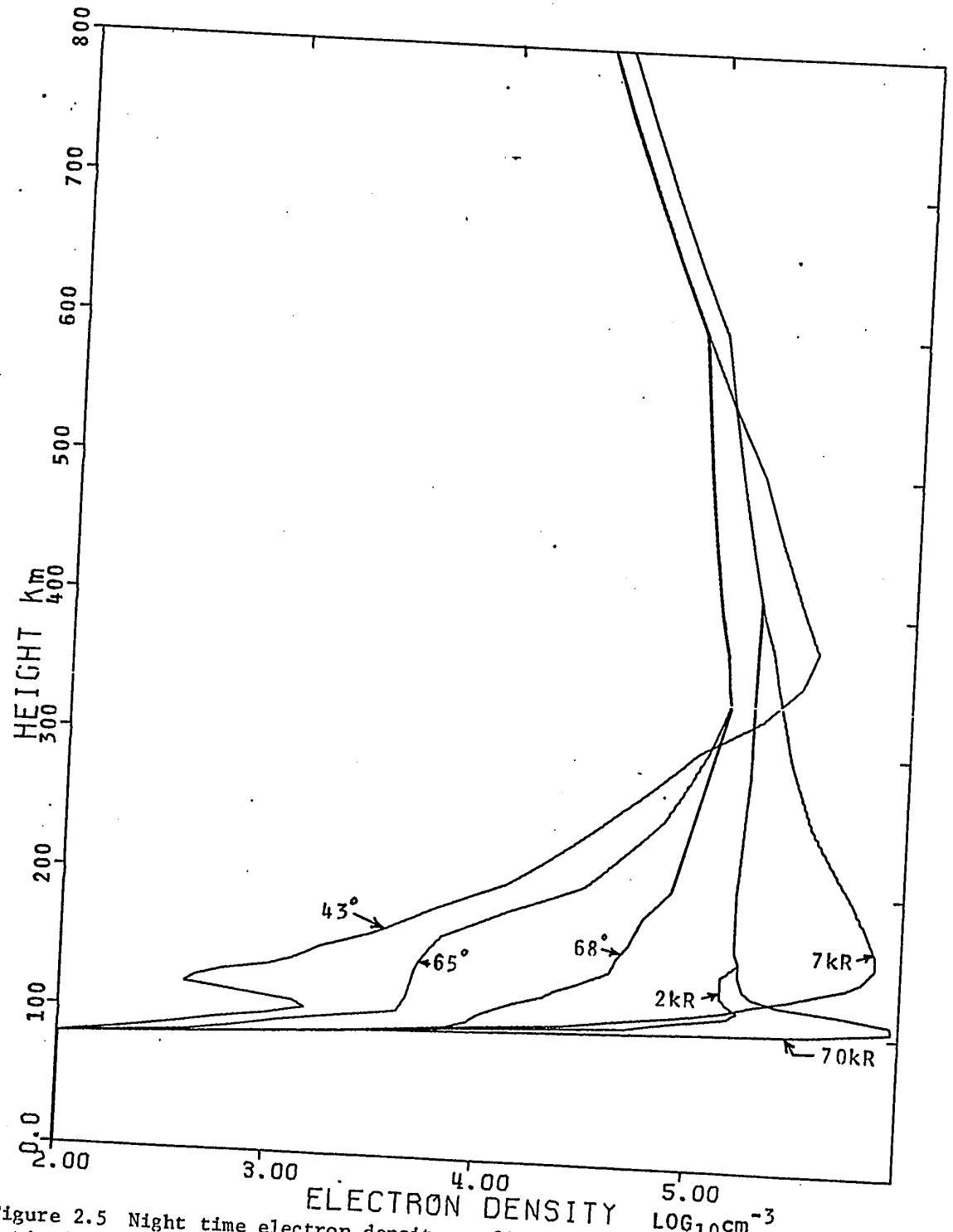

Figure 2.5 Night time electron density profiles as a function of geomagnetic latitude and the auroral brightness. The profiles are explained in the text.

The electron density in the auroral zone ionosphere during disturbed conditions has been extensively studied by rocket borne probes. The ascent and descent height profiles can vary by a factor of ten in one rocket flight over distances of 100 km and a duration of 3 minutes (Jacobs et al., 1969). Variations by a factor of 8-10 have been observed by Reddy et al., (1969) from quiet arcs to very disturbed conditions with a general combined increase in brightness and magnetic activity. The rocket flights show electron density fluctuations of $\Delta Ne/Ne<1$ and little variation with height above the E region (Föppl et al., 1968). An exception is the descent flight of McNamara (1969), Figure 2.5, (70kR), which passed through an enhanced region at 108 km that correlated with ground based and on-board photometer measurements of auroral brightness. The ascent profile is also shown in Figure 2.5 (2kR) with extrapolation for the F2 layer. The rocket-borne probes have produced considerable data on the electron density in the disturbed ionosphere but the information is limited to the trajectory and duration of the flight. This data has been further limited for making models by the scant information obtained simultaneously on the location and brightness of the arc.

The amount of input data required for the computer to construct a profile from observation or calculation was reduced by interpolation between the data points. An exponential interpolation formula was developed to fit the interpolated profile smoothly to a few data points over large height intervals in the topside of the F2 layer and is given by,

$$Ne(z) = Ne(z_a) \exp\left(\frac{dNe}{dz} (\ln(z) - \ln(z_a))\right) \qquad (2.48)$$

where

$$\frac{dNe}{dz} = \frac{\ln (Ne(z_b)) - \ln(Ne(z_a))}{\ln (z_b) - \ln (z_a)} \qquad (2.49)$$

and z_a and z_b are the heights at which the electron density is known.

2.5.2 Theoretical Auroral Ionospheres

The ionosphere electron density throughout the volume of the ionosphere occupied by a substorm current system and over the substorm's duration is required to permit adequate modelling of an event. Obviously rockets are inadequate for the task. A promising technique would be to use the ion or the electron continuity equation and calculate the ionization rate from the volume emission rate. The volume emission rate can be obtained from ground based photometers measuring the auroral brightness while scanning the sky and fitting this to models of arcs (Belon et al., 1966). Walker and Rees (1968) calculated the ionization rate from the volume emission rate profiles deduced by Belon et al., (1966) and then calculated the electron density from ion chemical equilibrium considerations. Their calculation is dependent on the reaction rates and number densities of the ions, both of which are not well known. One of their profiles is shown in Figure 2.5 for a 7 kR aurora. Their profiles correspond to the center of the arcs and often featured peak electron densities at 150 km, 30 km above that typically observed by rockets.

The electron density can also be calculated from the electron continuity equation as a function of time and height for given ionization (production), recombination (loss), and diffusion (transport) rates. The calculation can be repeated until the electron density reaches its new equilibrium state, taking care that the time increment is suitably short so that oscillation or over estimation does not occur. An increment of 2 seconds was found to be optimum. The brightness of an arc is proportional to the product of the volume emission rate and the optical path length through the arc. From analysis of cross sections for the process,

$$e + N_2 \rightarrow e + N_2^+ + e + \lambda 3914 \qquad (2.50)$$

Walker and Rees (1968) determined,

$$n\ (N_2^+) + n\ (N^+) = 17\ n(\lambda 3914) \qquad (2.51)$$

where n(X) is the rate of production of species X and n(λ3914) is the volume emission rate of N_2^+ at λ3914.

The ionization rate for atomic oxygen $n(O^+)$ and molecular oxygen $n(O_2^+)$ can be calculated from the nitrogen ionization rate and the oxygen and nitrogen number density in which case,

$$n(O_2^+) = 0.8\ [n(N_2^+) + n(N^+)]\ \ n(O_2)\ /\ n(N_2) \qquad (2.52)$$

$$n(O^+) = 0.5\ n(O_2^+) + 0.5\ [n(N_2^+) + n(N^+)]\ n(O)\ /\ n(N_2) \qquad (2.53)$$

to give the total production.

To determine the amount of ionization in terms of λ3914 emission only, the ratio of the oxygen to nitrogen ionization rates can be determined, which at 110 km is,

$$\frac{n(O^+) + n(O_2^+)}{n(N^+) + n(N_2^+)} = 0.3 \qquad (2.54)$$

From $q = n(N_2^+) + n(N^+) + n(O_2^+) + n(O^+)$

then $q = 1.3\ [n(N_2^+) + n(N^+)] = 22.4\ n(\lambda 3914) = 11.7\ n(\lambda 5577).$ (2.55)

The volume emission rates of λ5577 to λ3914 have a ratio of 2:1.

The ionization rate height profile is a function of the energy distribution and pitch angle of the precipitating particles as well as the density and composition of the neutral atmosphere (Rees, 1969). Auroral displays differ considerably in detail due to varying ionization rates. Bryant et al., (1970) calculated the ionization rate from energy distribution measurements, and made auroral brightness and electron density observations. Their profile is shown in Figure 2.6 along with profiles 0.1 times smaller and 10 times greater. The volume emission rate for λ5577 is shown in the same Figure 2.6 on the top scale, and agrees with that calculated by Belon et al., (1966) for an aurora of the same brightness.

The loss process of electrons is complicated, involving the equilibrium of atomic and molecular ions as well as the electrons. The loss of electrons by the dissociative recombination reaction with

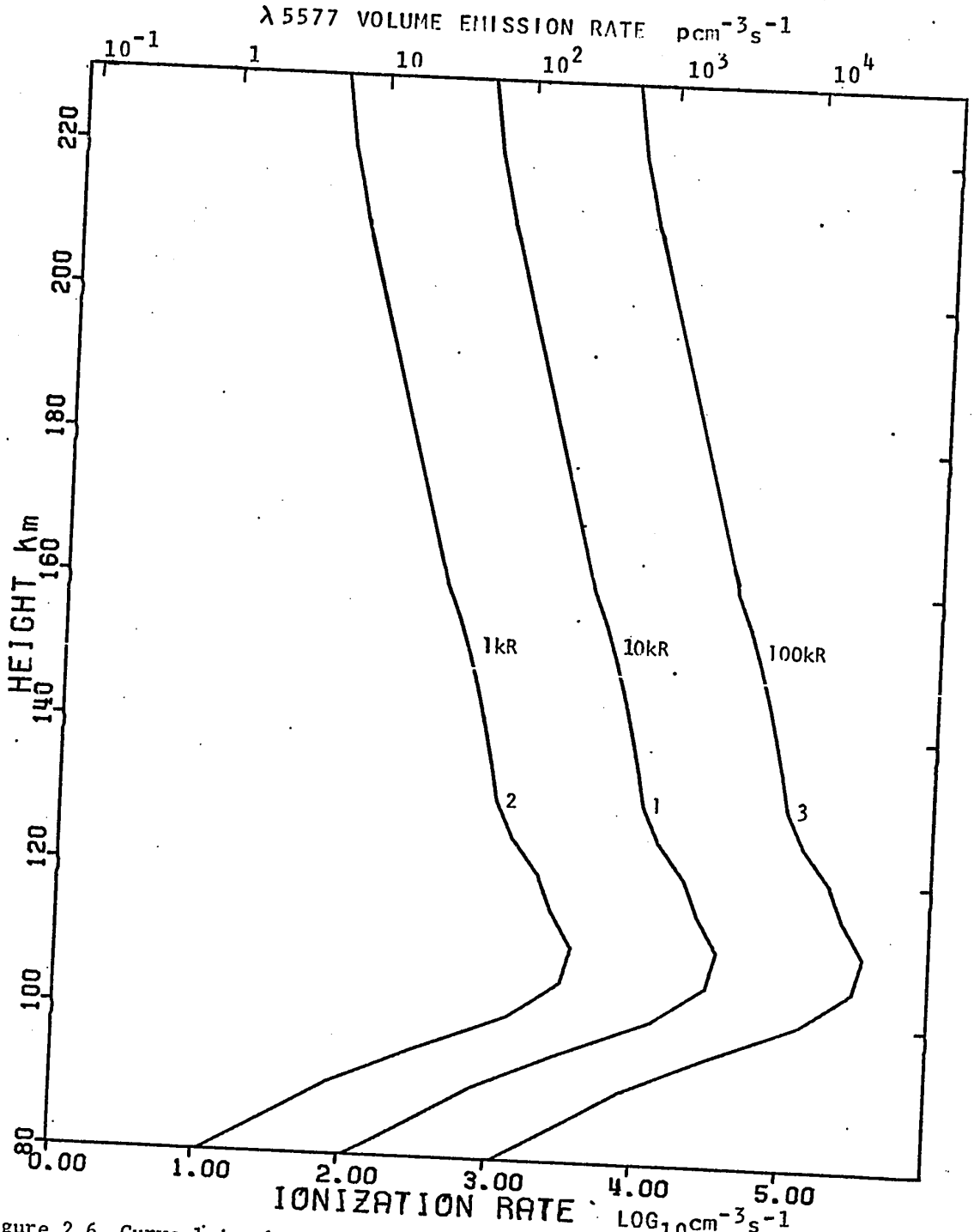

Figure 2.6 Curve 1 is the ionization rate measured by Bryant et al.(1970) for a 9.8kR arc, which is extrapolated above 120km. Curve 2 corresponds to a 1kR arc while curve 3 is equivalent to a very bright 100kR arc. The volume emission rate for the arcs is on the top scale.

molecular ions is of the form αN_e^2 and has a linear relationship β Ne for the ion - atom interchange reaction (Rishbeth and Garriott, 1969). The α coefficient is temperature dependent only, while β varies as the molecular concentration. The electron continuity equation, 2.5, can be written as (Ratcliffe, 1956),

$$\frac{dNe}{dt} = q - \frac{Ne}{\frac{1}{\beta} + \frac{1}{\alpha Ne}} - Da \frac{d^2Ne}{d z^2} - Dp \frac{d^2Ne}{d y^2} \qquad (2.56)$$

where Da, Dp are the diffusion coefficients along and across the magnetic field respectively. Bryant et al., (1970) calculated an average α in an aurora of 3×10^{-7} cm^3/s while β has been calculated from the expression of Quinn and Nisbett (1965) for summer and a thermopause temperature of 1025°K.

$$\beta(z) = 1.1 \times 10^{-4} \exp [(300 - z)/27] s^{-1} \qquad (2.57)$$

Solving for the electron density for a time increment from the continuity equation, and neglecting transport terms, gives

$$Ne\ (z,\ t + \Delta t) = \frac{q(z)\ \Delta t + Ne\ (z,t)}{1 + \frac{\beta(z)\ \alpha\ (z)\ Ne(z,t)\Delta t}{\beta(z) + \alpha(z)\ Ne(z,t)}} \qquad (2.58)$$

The plasma in an arc will diffuse because of its greater density. The electrons will diffuse faster than the ions because of their greater mobility in the E region, but become retarded as a differential electric field is created resulting in an intermediate or ambipolar diffusion rate. The ambipolar diffusion coefficient in a lightly ionized plasma is given by (Holt and Haskell, 1965),

$$Da = \frac{kT_i}{m_i \nu_{in}} \tag{2.59}$$

where T_i, m_i, and ν_{in} are the ion temperature, mass, and collision frequency. Diffusion will occur across the field lines as well as ambipolar diffusion along the magnetic field. The diffusion coefficient across the magnetic field is given by (Holt and Haskell, 1965),

$$Dp = \frac{Da}{1 + \frac{\omega_e \omega_i}{\nu_e \nu_i}} \tag{2.60}$$

where $\omega_{e,i}$ and $\nu_{e,i}$ are the electron and ion, gyro and collision frequencies defined in section 2.2 and 2.3 respectively. The effect of diffusion on the redistribution and depletion of electrons in an arc can be calculated for a time increment from,

$$Ne\ (z,t+\Delta t) = \frac{Da(z)\Delta t}{z^2}\ [Ne\ (z,t) + Ne\ (z+\Delta z,t) - 2Ne(z-\Delta z,t)]$$

$$+ \frac{Dp(z)\Delta t}{\Delta y^2}\ [2\ Ne\ (z,t) - 2\ Ne\ (z,t)] + 2\ Ne\ (z,t) \tag{2.61}$$

where z and t are the height and time, Δy is the width of the arc and Ne° is the electron density outside the arc.

Electric fields will also cause drifts across magnetic field lines, but mainly above 200 km. A southward electric field in the northern hemisphere which is generally observed, will cause the plasma to drift westward, along an arc, while a westward electric field would cause a northward drift. Neutral winds will also redistribute the plasma (Stubbe and Chandra, 1970; Brace et al., 1970).

The height profiles of the electron density in Figure 2.7 were calculated at 2 second intervals from the electron continuity equation. The three ionization profiles in Figure 2.6 were used together with the above α and β coefficients for recombination and the ambipolar diffusion coefficients for components along and perpendicular to the magnetic field. The initial profile at $t = 0$ in Figure 2.7 was observed from the NASA 18.02 rocket flight for quiet auroral conditions while the lowest ionization rate was used corresponding to a very weak aurora of approximately 1kR brightness. The electron density height profile reached near equilibrium after 20 seconds, at which time the ionization was increased by a factor of 10 corresponding to a 10 kR aurora. The equilibrium electron density at 40 seconds agrees with that observed by Bryant et al. (1970) for the same conditions. A further increase in the ionization rate by a factor of ten causes the electron density to eventually reach a peak of nearly 3×10^{6} /cm^{3} for a very bright aurora of 100 kR.

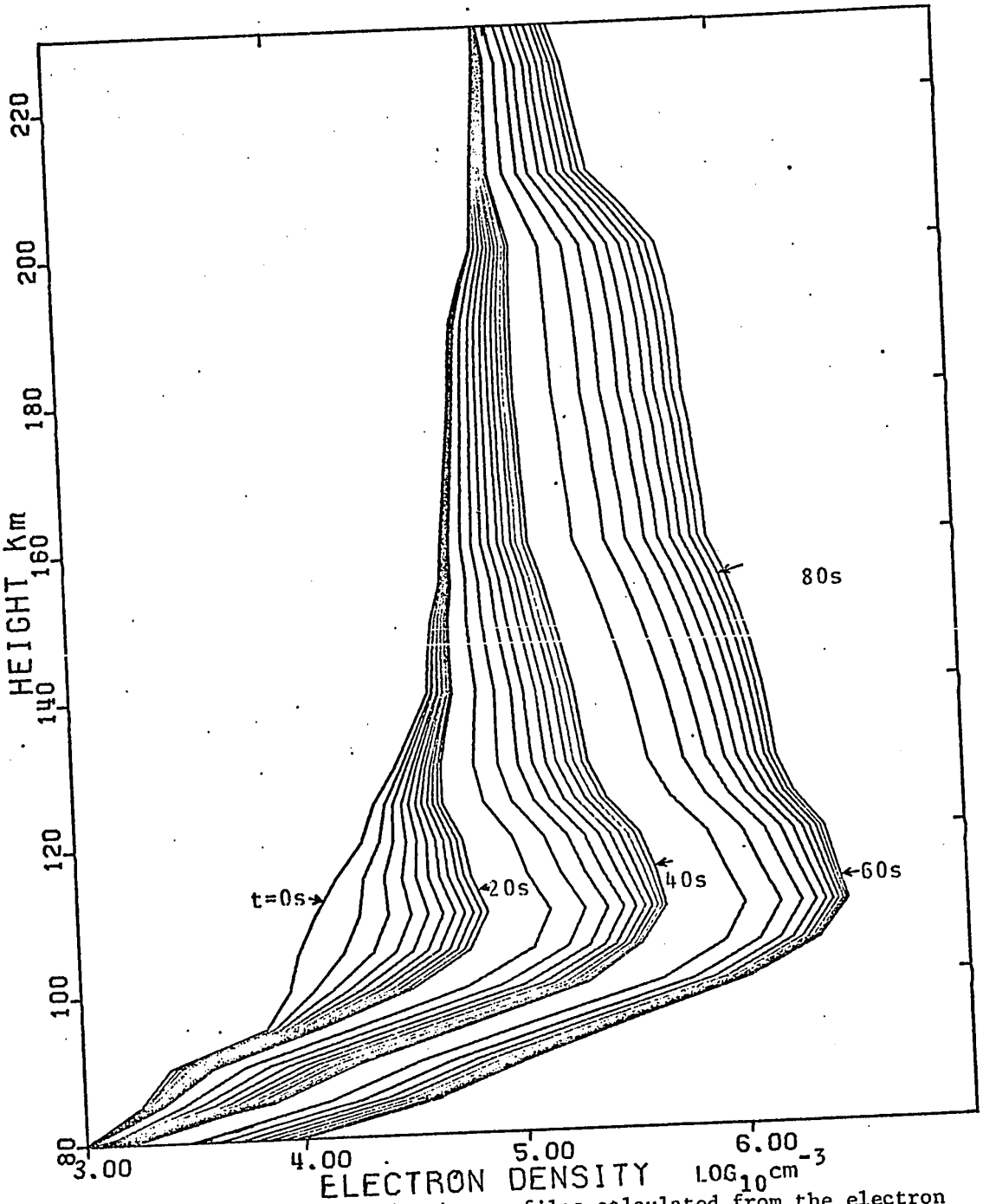

Figure 2.7 Dynamic electron density profiles calculated from the electron continuity equation at 2 second intervals. The initial profile at t=0s is for no aurora while at 20s,40s and 60s the electron density corresponds to arcs of 1kR, 10kR and 100kR.

The rate of loss of electrons after an arc has passed through the observing region or disappeared is slower than the rate of increase in the electron density when an arc brightens. The electron density profile shown in Figure 2.7 at 80s is the same profile 20 seconds after the ionization rate has been reduced by 100 times for the 60s profile. The time required for the ionosphere to reach the original equilibrium electron density profile at t = 0s from t = 60s is of the order of 1/2 to 1 hour, which is the duration of a substorm. This slow decay rate explains why intense auroral electrojets can be found after the auroral display has passed, as was observed by Walker (1964).

Ionization profiles are dependent on the energy distribution and pitch angle of the precipitating particles which vary considerably, resulting in different ionization profiles which in turn produce different electron density profiles.

2.5.3 Analytic Auroral Ionosphere

The method of determining the electron density from the continuity equation as outlined in section 2.52 is necessary for a dynamic ionosphere but is tedious and expensive for models of a quiescent aurora. An explicit expression for calculation of an ionosphere as a function of height and auroral brightness for steady arcs is desirable. The auroral ionosphere appears to have a height profile consisting of a Chapman layer for both the F2 region and the aurora in the E region. The volume emission rate is proportional to the ionization rate which in turn appears to have a 1/2 power relationship with the peak of the equilibrium electron density profile as shown in Figure 2.7. This fact was used to determine

the peak of the electron density in the E region as a function of aurora brightness. The F2 layer is only slightly enhanced, probably due to both ionization and diffusion from the F1 layer, thus the 0.15 power of the volume emission rate is reasonable. An expression was developed to calculate the electron density as a function of height and the volume emission rate of λ5577 (I) for the auroral zone, and is,

$$Ne\ (z,I) = AI^{\frac{1}{2}}\ 10^5 \exp 1/2\ (1 - Za - \exp\ (-Za)) \qquad (2.62)$$

$$+ I^{0.15}\ 10^5 \exp 1/2\ (1 - 1.4\ Zf - \exp\ (-0.75\ Zf))$$

where

$$Za = (z - Za^{\circ} + I^{\frac{1}{2}})/Ha$$

$$Zf = (z - Zf^{\circ} + I^{3/5})/(Hf + 4Zf^2)$$

$$A = 1.2\ (\lambda 5577),\ A = 1.6\ (\lambda 3914),\ A = 2.8\ (\lambda 4278)$$

I is in units of kilophotons/cm^3s (Gp/m^3s), Za and Zf are the reduced height for an arc and for the F2 layer. Both the arc and the F2 layer occur at lower heights with increasing brightness which is accounted for by the 1/2 and 3/5 powers of I in the reduced height expressions. The exponential decay of the F2 topside layer decreases with height which is affected by increasing the scale height of Hf by $4Zf^2$. The scale height of an arc is approximately 10, depending on the type of aurora, while F2 layers are ~75. The bottom side of the

F2 layer was modified by the factor 0.75 in the exponent and by 1.4 in the expression to conform with observation of a continuum there. The initial height of the maximum of the arc and F2 layers are at Za° (118 km) and Zf° (450 km). The electron density as a function of height and peak volume emission is shown in Figure 2.8 for 0.3, 1, 3, 10, 30 and 100 kR arcsof 10 km width. The expression can be used for any of the three commonly measured auroral emissions λ5577,λ3914 and λ4278.

The theoretical expression produces ionospheres which are in agreement with observations of Bryant et al., (1970) and Walker and Rees (1968); furthermore it is a reasonable fit to most types of aurora and is adequate for models of electrojets. The functions in the parameters in the expression can readily be adjusted to fit new simultaneous rocket or ionospheric sounder and auroral brightness observations. The expression can be used to model the broad enhanced nightglow region on either side of the auroral arcs and a large range of arcs with varying size, brightness, and form. Provision was made in the computer program for calculation of the ionosphere from either observations or the above analytic expression.

2.5 Negative Ions

The lower part of the ionosphere, the D region, probably contains negative ions which can contribute to the conductivity. Little is known about these ions because of the difficulty of making any measurements in this region, however some theoretical calculations suggest approximately 100/cm^3 (Danilov, 1970). A simple Chapman layer was used to construct a negative ion (Ni) height profile with

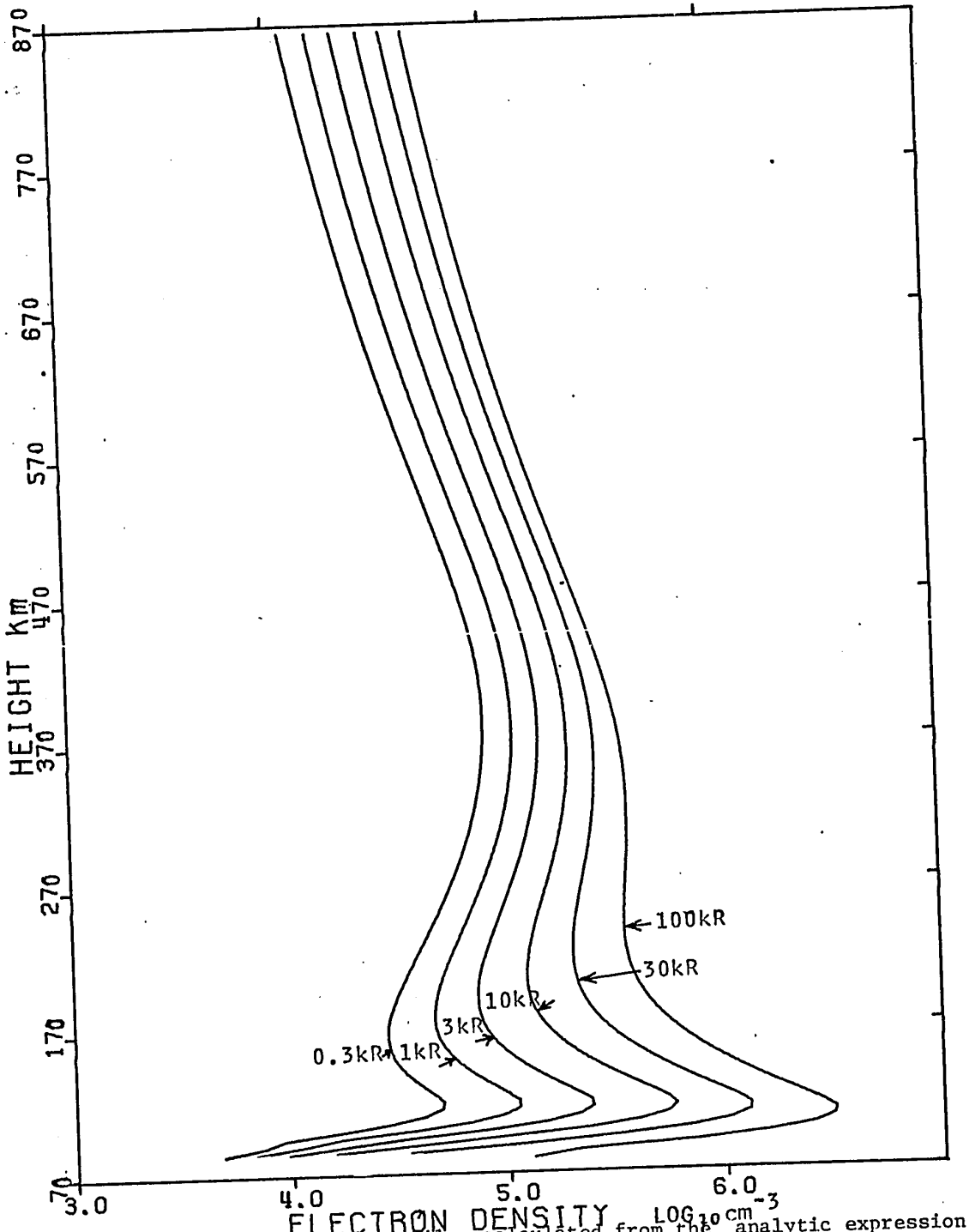

Figure 2.8 Electron density profiles calculated from the analytic expression 2.62 for auroras ranging in brightness from 0.3kR(night sky) to 100kR.

maximum at 85 km and a scale height of 5 km with the following form,

$$Ni\ (z) = 100 \exp\ (1 - Zi - \exp\ (-Zi)) \qquad (2.63)$$

$$Zi = (z - 85)/5$$

where Zi is the reduced height. Swider (1971) gives an expression for the ratio of negative ions to electrons for a PCA of $\lambda = 10^{(13 - \frac{z}{5})}$ where $80 > z > 40$ km.

2.6 Electron and Ion Temperatures

Below the E region the electrons, ions and neutrals are kept in thermal equilibrium by the high collision frequency. The collision frequency is dependent on the number density, and the cross-section, which is smaller for electrons than for ions; consequently the electrons can maintain a separate temperature from that of ions or neutrals at a lower altitude. The electrons are heated at night primarily by suprathermal energetic particles (Maier and Narasinga Rao, 1970). These electrons can then have temperatures of 3000 - 8000°K in the F2 region compared with 1000°K for the neutrals. Walker and Rees (1968) calculated the electron temperature from thermal equilibrium considerations for five arcs and found the maximum temperature to range from 2920 °K to 3511 °K. An empirical electron temperature profile was developed to fit these observations so that the electron temperature could be calculated as a function of height and volume emission rate or auroral brightness and is given by,

$$Te\ (z,\ I) = 3000\ I^{0.15}\ \exp\ 1/2\ (1 - 2.5\ \tanh(\frac{Zt}{2.5}) - \exp(-Zt))$$

where

$$Zt = (z - 350)/150 \qquad (2.64)$$

Te is the electron temperatures, I is the volume emission rate of oxygen λ5577, and z is the height. Provision was made in the computer program to calculate the electron temperature height profile directly from observations or from the above expression. The amount of data for the calculation of the electron temperature profiles from observations was reduced by linear interpolation between the measurements. The electron temperature profiles are shown in Figure 2.9 for the aurora as used for the electron density profile in Figure 2.8.

The ion temperature can be computed from the balance between the rate at which ions are heated by Coulomb collisions with the electrons and cooled by elastic collisions with the neutrals. The rate of heating, Q, and cooling, L, is taken from Rishbeth and Garriott (1969).

$$Q = 7.6 \times 10^{-6}\ \frac{Ne\ Ni}{Mi\ Te^{3/2}}\ (Te - Ti) = R(e)(Te - Ti) \qquad (2.65)$$

$$L = Ni\ Uin\ Ni\ (Ti - Tn) = R(n)\ (Ti - Tn) \qquad (2.66)$$

where Uin is the sum of the neutral particle collision coefficents given by Dalgarno and Walker (1967); Ne, Ni, and Mi are the number densities of electrons, ions, and the mass of ions in atomic mass units, (A.M.U.) respectively. The ion temperature is then given by,

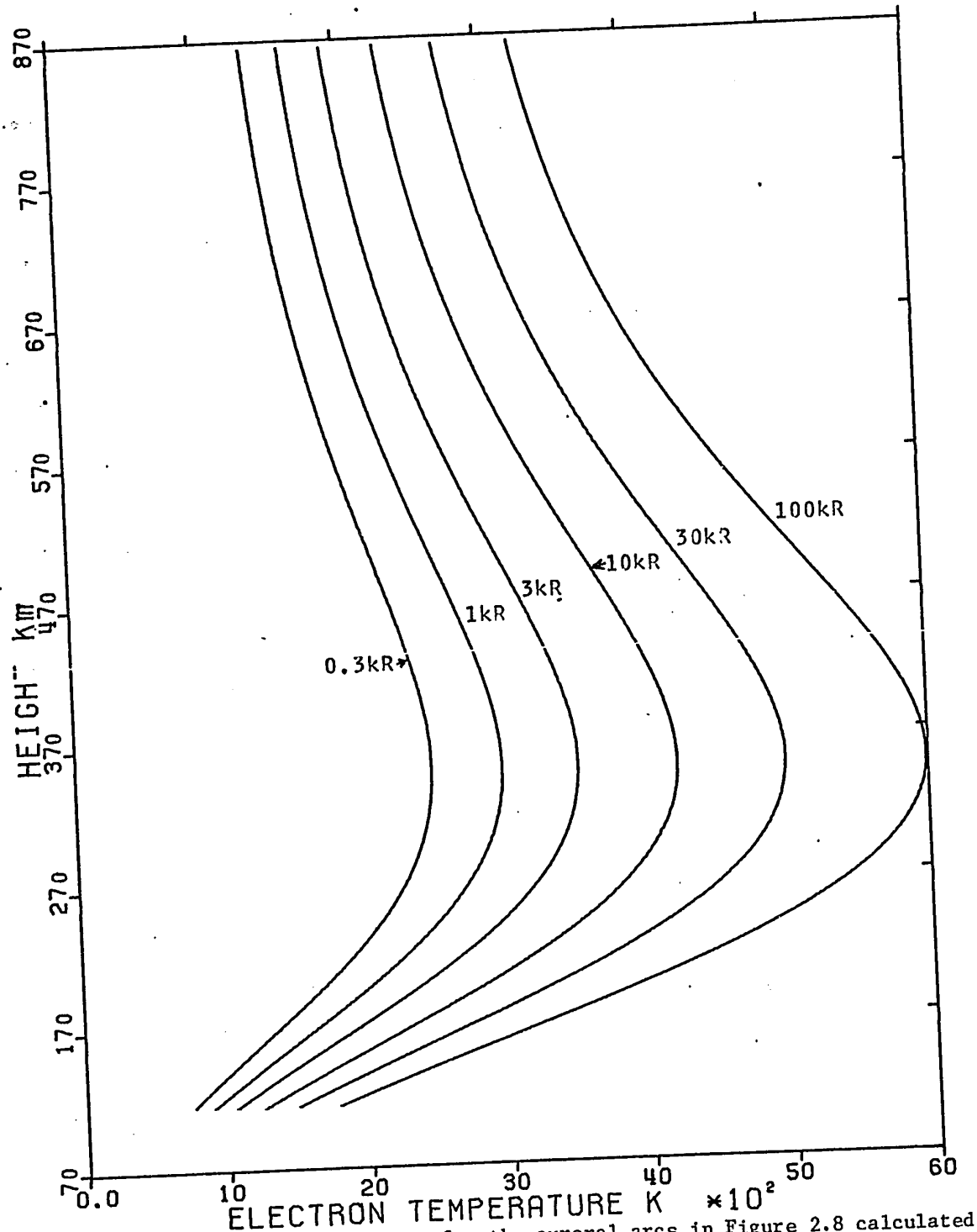

Figure 2.9 Electron temperatures for the auroral arcs in Figure 2.8 calculated from the analytic expression 2.64.

$$Ti = \frac{R(n)\ Tn + R(e)\ Te}{R(n) + R(e)} \qquad (2.67)$$

The ion temperature is shown in Figure 2.12 for the corresponding different electron temperature profiles in the same figure. Good ion thermal coupling maintains the ion temperature near the neutral temperature up to 250 km. At this height ion-electron coupling becomes significant and eventually dominant, resulting in the ion temperature approaching the electron temperature.

2.7 Calculation of the Atmosphere and Ionosphere

The parameters for the calculation of a neutral atmosphere and ionosphere from approximate temperature and electron density height profiles were programmed in standard fortran on a computer. Part of the neutral atmosphere calculation was taken from Pitts (1968) with the thermopause temperature and the neutral constituent density added to this part of the program. The parameters of the ionosphere were calculated from electron density and temperature profiles which could be obtained from either the developed empirical expressions or as input to the program at several heights. The expressions for the electron density and the electron temperature are functions of the peak volume emission rate of the aurora. The magnetic field which is used in the calculation of the electron and ion gyrofrequency is calculated from the International Geomagnetic Reference Field spherical harmonic coefficients as a function of latitude, longtitude and height. The negative ion density is calculated from an empirical expression developed from an appropriate Chapman layer. The ion

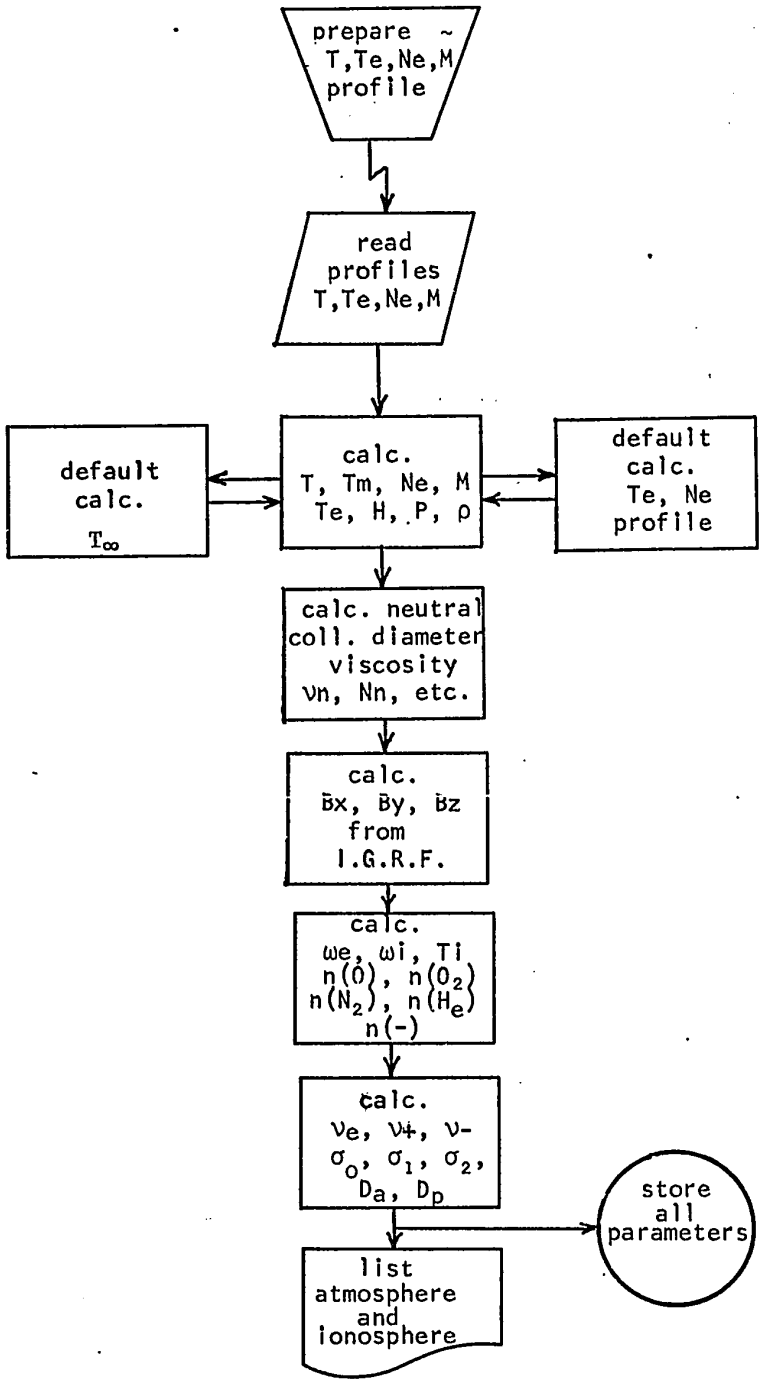

Figure 2.10 Flow chart of the computer program for the calculation of an atmosphere and ionosphere and related parameters.

temperature was calculated from thermal equilibrium conditions between the electrons and neutrals. The electron neutral and ion neutral collision frequencies are calculated for each of the constituents of the atmosphere and then combined with the electron ion and ion-ion collision frequencies to obtain the overall electron and ion collision frequency. The specific, Pedersen, and Hall conductivities and the ambipolar diffusion coefficients are then calculated for each of the height levels. The atmosphere and ionosphere parameters are listed and stored on a suitable computer medium such as magnetic tape or disk for use by other programs. The flow chart highlights of the computation are shown in Figure 2.10. Profiles of the ionosphere conductivity tensor and temperature are shown in Figures 2.11 and 2.12 respectively.

2.8 The Electric Field

The electric field in the ionosphere that drives the auroral current system probably has its origin in plasma moving in the magneosphere; however, neutral winds in the E region of the ionosphere and the streaming of solar wind across the magnetosphere and magnetotail can also cause an electric field. The electric field is caused by the $\vec{V} \times \vec{B}$ force when a plasma is moving across a magnetic field and is given by Block (1965) and Mozer (1970),

$$E = -\vec{V} \times \vec{B} \tag{2.68}$$

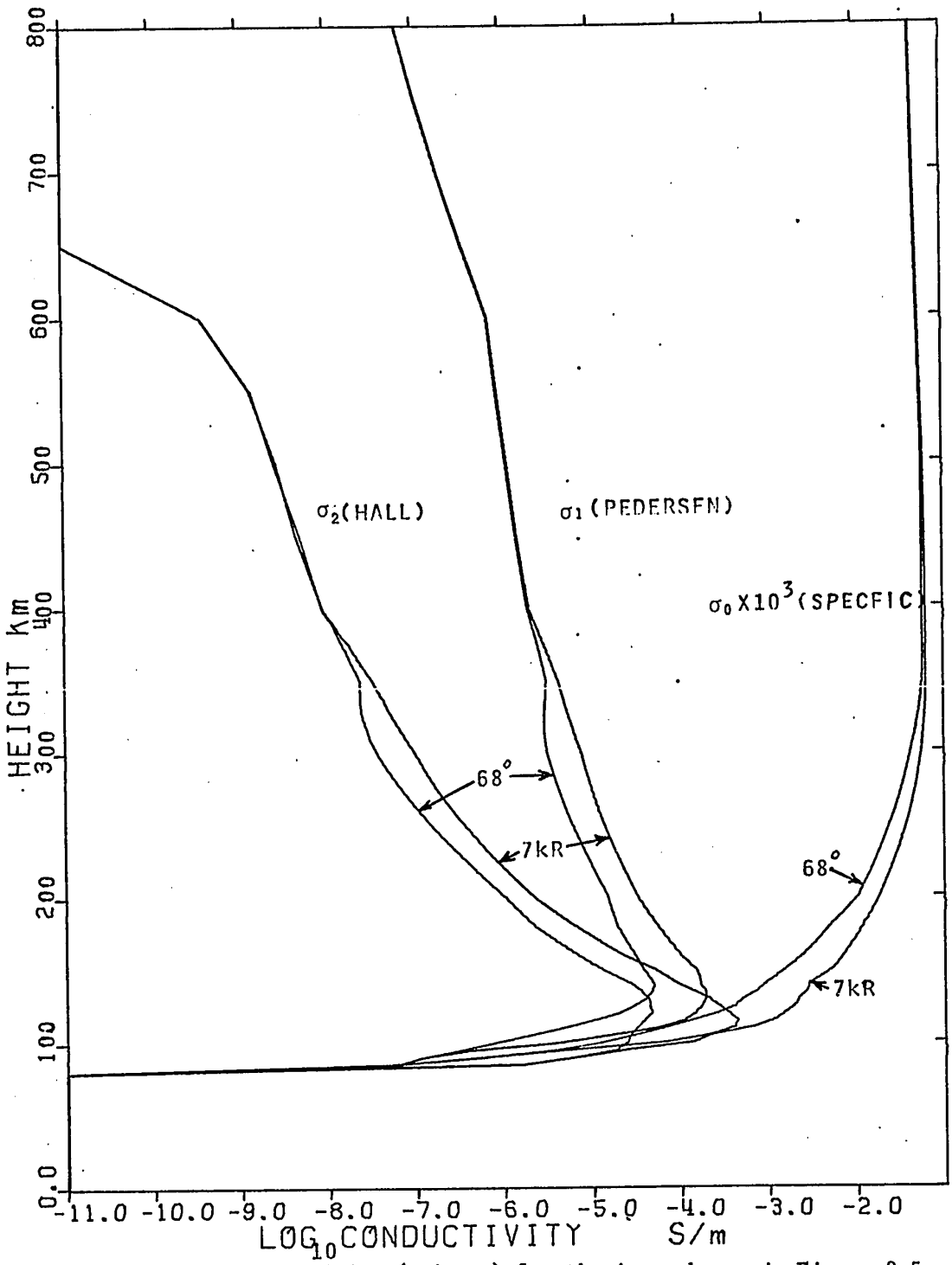

Figure 2.11 The conductivities (seimens) for the ionospheres in Figure 2.5.

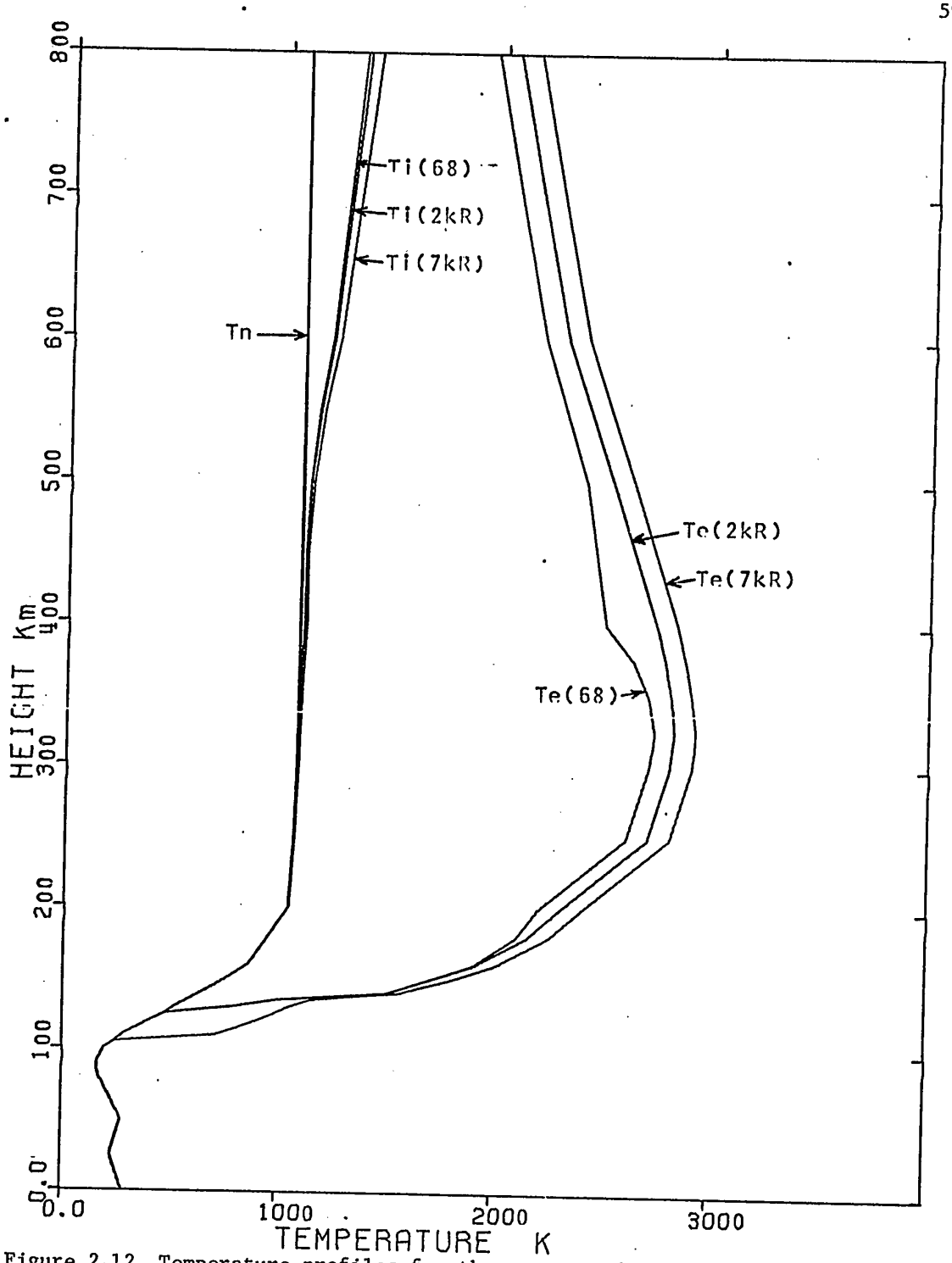

Figure 2.12 Temperature profiles for the corresponding ionospheres in Figure 2.5.

An electric field can also be induced by the motion of field lines such as during the compression and inflation of the magnetosphere during substorms (Lezniak and Winckler, 1970). Another possible source of an electric field is charge displacement occurring when the neutral plasma flowing up the plasma sheet in the tail of the magnetosphere encounters the earth's dipole field (Hruška, 1971). The conductivity along the magnetic field is several siemens per meter making the ionosphere and magnetosphere good conductors in the direction parallel to the field lines or equipotentials. The conductivity across the field lines is highest in the auroral E layer but this is still a factor 10^4 less than the specific conductivity. The electric field will be projected along a flux tube because of the high specific conductivity, Mozer and Serlin, (1969), and the electric field will thus be the vector sum of all the electric field sources along a given magnetic flux tube. The flux throughout a magnetic tube of force in the earth's geomagnetic field is constant so the electric field must change with the flux density. The mapping of the electric field from one region of the magnetosphere along a flux tube to another region is different for the two orthogonal electric field components. Ideally, this mapping would require following two adjacent field lines to calculate the electric field components at the new location; hence necessitating a model of the magnetic field throughout the magnetosphere. The expressions for the electric field components for a centered dipole representation of the geomagnetic field have been derived by Matsushita and Tarpley (1970) as,

$$\frac{Ex\ (M)}{Ex\ (I)} = \left(\frac{\sin\theta_I}{\sin\theta_M}\right)^3 \qquad (2.69)$$

$$\frac{Ey\ (M)}{Ey\ (I)} = \left(\frac{1 + 4\ \cot^2\theta_M}{1 + 4\ \cot^2\theta_I}\right)^{\frac{1}{2}} \quad \frac{\mathrm{cosec}^2\theta_M}{\mathrm{cosec}^2\theta_I} \qquad (2.70)$$

where M and I are the magnetosphere and ionosphere; θ_M and θ_I are the colatitudes to the magnetosphere and ionosphere locations which are along the same field line. At 65° geomagnetic latitude the ratio of Ex component in the ionosphere and magnetosphere equatorial plane is 13 while the Ey component ratio is 25. The components of an electric field in the magnetospheric equatorial plane would be multiplied by these values and because the products are unequal the electric field would rotate to the meridional plane in the ionosphere. The electric field can thus be measured in one region of the magnetosphere or ionosphere and mapped to another region along the same magnetic field line by the above expressions, assuming the absence of parallel electric fields.

The electric field in the ionosphere has been the major unknown to date. Johnson and Kavadas (1963) made the first measurements; since then the ionospheric electric field has been measured numerous times but no systematic distribution of the electric field across the auroral zone has yet been observed. Mozer and Fahleson (1970) and Potter (1970) observed an increase in the electric field near an arc while Wescott et al., (1969) and Aggson (1969) have observed a decrease in the electric field inside arcs. The measured horizontal electric fields are from a few millivolts per meter to perhaps 150 mV/m while the vertical field is probably less than .01 mV/m. The electric fields have been measured by rockets and balloon-borne probes and by the method of

ionized barium clouds and by airglow excitation Walker (1970). Rockets and satellites give good spatial distribution but only for a few minutes, while the barium clouds generally move parallel to the arcs for a few tens of minutes. Balloon-borne probes (Mozer and Serlin, 1969) provide good temporal measurements for approximately one day. No relationship between the electric field and other auroral zone parameters has been established for model construction so the electric field distribution must be measured at the same time as the electron density and magnetic field variations are measured.

Estimates of the direction and magnitude of the electric field can be obtained from known winds and plasma convection patterns. Poleward winds of about 100 m/s have been observed in the auroral zone which produce an eastward electric field of a maximum of 5 mV/m. The geometry of plasma convection in the tail of the magnetosphere is very complex. The dynamics include motions of the magnetic field as well as spatial and temporal variations of the plasma in the magnetotail during substorms. Detailed analysis of the plasma motion and magnetic field configuration are necessary for the calculation of the electric field and mapping it into the ionosphere. Axford (1969) discusses an electric field in the magnetotail of $\sim$1mV/m from general flow considerations for the plasma which agrees with the mapped observations of Mozer and Serlin (1969) and Mozer (1971). The general pattern Mozer (1971) sees is a large southward electric field developing around local midnight in the ionosphere; this southward electric field disappears by morning and is preceded by a northward field before midnight. A small eastward field is occasionally present before local midnight; this is displaced at approximately local midnight by a large westward field which generally disappears by morning.

CHAPTER 3

CURRENT FLOW AND INTERACTION

3.1 Current Flow

The horizontal currents in the ionosphere can be calculated from approximate models or observations of the electron density and the electrical fields, but the vertical current is generally indeterminate because the vertical electric field is unknown. A model of the auroral zone can be constructed and the known horizontal electric fields applied to calculate the horizontal current flow throughout the region. The vertical current can be solved from the divergence-free condition for the current. The calculation of the vertical current from $\vec{\nabla}.\vec{J} = 0$ requires a 3 dimensional model of the auroral zone ionosphere and horizontal components of the electric fields at one instant in time; such observations are difficult to obtain. Some information along a meridian through the auroral zone during a magnetic storm is available from the August 1969 joint observations of Drs. F. Mozer and G. Rostoker. The time dependent cross sections can provide information on the spatial variation since the approximate size of the auroral electrojet is known from simultaneous observations of the magnetic field such as those carried out by Walker (1964). The cross section is sufficiently thin that the divergence of the current can be solved independently of the east-west current in the 3 dimensional model. Having determined the current flow in several cross sections for an auroral substorm the Birkeland field-aligned current flow can then be solved by applying divergence-free conditions to the 3 dimensional model.

The auroral zone ionospheres are constructed by combining appropriate height profiles calculated in the previous chapter to model the temporal and spatial variations of the electron density. The dynamic arcs can be modelled and combined with various electric fields to produce many current systems. Effects of the currents can then be calculated and compared with magnetic field observations to check the model, and also calculate possible current interactions with the atmosphere and ionosphere. Some effects which can readily be calculated for comparison are magnetic fields, current induced neutral winds, and Joule heating.

Assuming a cross section for an auroral zone ionosphere model constructed from a grid as in Figure 3.1, then the horizontal current flowing at height u and in the middle of block ℓn at m is,

$$j_x^{um} = \sigma_1^{um} E_x^{um} + \sigma_2^{um} E_y^{um} \tag{3.1}$$

$$j_y^{um} = -\sigma_2^{um} E_x^{um} + \sigma_1^{um} E_y^{um} \tag{3.2}$$

From the divergence equation for current block ℓn(uv)

$$\frac{\partial J_x}{\partial x} + \frac{\partial J_y}{\partial y} + \frac{\partial J_z}{\partial z} = 0 \tag{3.3}$$

where J_x, J_y and J_z are the total currents entering the sides of the block. The auroral zone cross section is thin compared to the size or length of a substorm current system which may be a few thousand kilometers long. Assuming $\frac{\partial J_x}{\partial x} \simeq 0$ within the section, J_z is then given by,

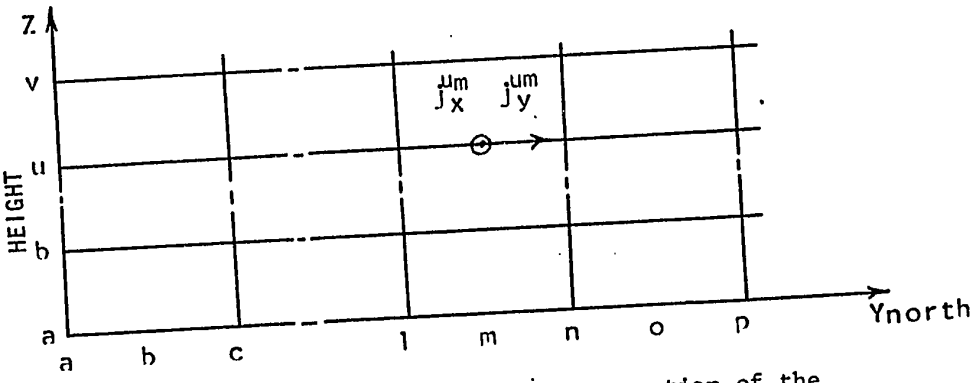

Figure 3.1 Schematic meridional cross section of the ionosphere grid for calculating the current density.

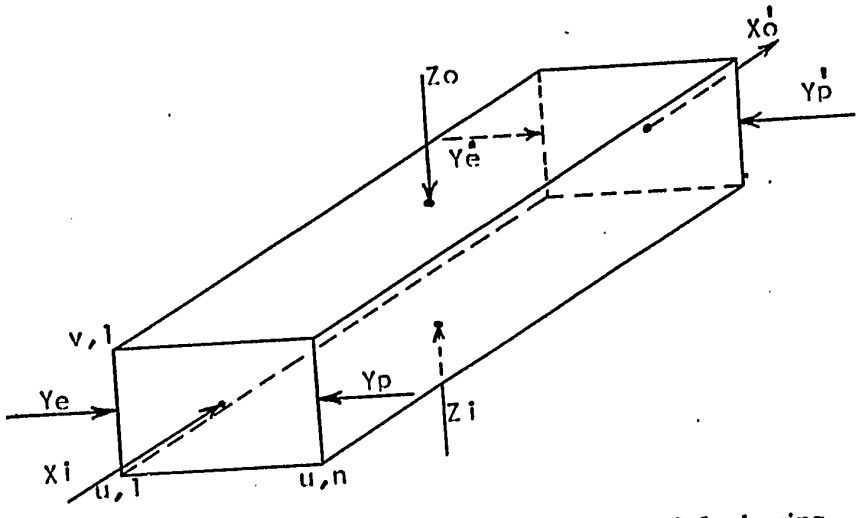

Figure 3.2 One block of the grid of Figure 3.1 showing the 3 dimensional currents.

$$J_z^{um} = - \int_{z=a}^{u} \frac{\partial J_y}{\partial y} \, dz \tag{3.4}$$

The vertical current flowing into the lowest layer, J_z^{am} is assumed to be zero as the layer is at 80 km where the specific conductivity is very low. The gradient of the current across the block was obtained by linear extrapolation from the calculation for current at the center of the block where the observations were assumed to be made so that,

$$j_y^{un} = 2 \, j_y^{um} - j_y^{u\ell} \tag{3.5}$$

The specific current flowing through the top of the block at layer v is then given by,

$$j_z^{vm} = \Sigma_v \, (j_y^{un} + j_y^{vn} - j_y^{v\ell}) \, \frac{\Delta z}{2\Delta y} \tag{3.6}$$

The components of all the currents can thus be obtained for a column independent of adjacent columns, enabling a larger number of ionospheric profiles to be in the cross section without requiring correspondingly larger storage in the computer. The integration was checked for each column by comparing the total flow of current into the column with that flowing out and was found to be within .01%.

Boundary requirements between blocks can be used to calculate currents for several different assumptions about current flow or conditions in the block. One assumption might be that no current flows in the meridian direction out of a column on the equatorial or poleward sides of the auroral zone due to a low ionization density or weak electric fields. This assumption appears to hold when the cross section coincides with the demarcation line of a substorm (Rostoker, 1966; Kisabeth and Rostoker, 1971) and can also be seen in the current flow diagrams of Walker (1964). At the boundary between blocks the tangential electric fields, E_x and E_z, and the perpendicular current j_y, are continuous. The current at the boundary n, Figure 3.1, is given by expression 3.5, while the electric field at n is given by,

$$E_x^{un} = 2\,E_x^{um} - E_x^{ul} \tag{3.7}$$

for $$j_y^{up} = 0 \tag{3.8}$$

then $$j_y^{uo} = 1/2\; j_y^{un} = j_y^{um} - 1/2\; j_y^{ul} \tag{3.9}$$

$$E_x^{uo} = 1/2\; E_x^{un} = E_x^{um} - 1/2\; E_x^{ul} \tag{3.10}$$

$$E_y^{uo} = \frac{j_y^{uo}}{\sigma_1^{uo}} + \frac{\sigma_2^{uo}\; E_x^{uo}}{\sigma_1^{uo}} \tag{3.11}$$

and hence $$j_x^{uo} = \sigma_1^{uo}\; E_x^{ou} + \sigma_2^{uo}\; E_y^{ou} \tag{3.12}$$

A second possibility is for the current flowing across the arc to remain constant and cause polarization, as suggested by the models of Armstrong and Zmuda (1970) and Boström (1964). For the j_y current in block npuv to be constant and equal to that in the previous block at the boundary n we require,

$$E_x^{uo} = E_x^{un} = 2\,E_x^{um} - E_x^{u\ell} \tag{3.13}$$

$$E_y^{o} = E_y^{n} = \frac{\Sigma\, j_y^n}{\Sigma\, \sigma_1^o} + \frac{\Sigma\, \sigma_2^o\, E_x^o}{\Sigma\, \sigma_1^o} \tag{3.14}$$

The components of the current can then be calculated from expressions 3.1, 3.2 and 3.6.

The 3 dimensional flow of current in the ionosphere can be determined by the superposition of cross sections to model the complete electrojet flow at any instant in time. The cross sections, constructed as a function of time for an event along a meridian, are assumed typical of the spatial variation across the electrojet. The horizontal flow of current from the polar cap and the midlatitude regions towards the auroral electrojet is known from the cross sectional models so the application of the divergence-free requirement will give any vertical or Birkeland type field-aligned flow of current. Consider Figure 3.2 which now represents a layer for an arc a few hundred kilometers long.

Vectors X,X^1 and Y and Y^1 have been determined by expressions 3.1 and 3.2 at each end of the block. The Y vector or meridional current is the current determined along the ends of the cross sections

in Figure 3.1 and does not include the field-aligned currents calculated by 3.4 or 3.6 The current entering side Ye Ye^1 and YY^1 can be calculated knowing the dimensions of the model in the x direction so that the vertical component Z_o can be determined if Z_i is known. Z_i can be assumed zero for the bottom layer, thus,

$$J_z = -\int_{z=a}^{u} \left(\frac{\partial J_x}{\partial x} + \frac{\partial J_y}{\partial y}\right) dz \qquad (3.17)$$

3.2 Magnetic Fields

The magnetic fields of the auroral electrojets have been extensively used as the main method of studying the physics and dynamics of the current system. Magnetic field variations can be misleading because they are a superposition of all ambient current flow and main field motions, which may be caused by magnetospheric fluctuations, making analysis of the current system difficult. This type of analysis is further complicated by the rapid spatial and temporal variations of the auroral current system and the limited resolution of magnetometers. For example, ground based magnetic observations cannot resolve simple line currents less than 100 km apart while multiple auroral arcs where currents are thought to flow are typically 40 km apart. The auroral electrojet may be driven by two antiparallel current sheets on either side of the electrojet which ideally cannot be detected by ground measurements but have been seen by satellites (Armstrong and Zmuda, 1970). The return current system also cannot be uniquely analyzed because the ionosphere return path and the Birkeland field-aligned return current

system have similar magnetic variation patterns at the earth (Fukushima, 1969). Ring currents at a few earth radii, induction, and induction anomalies also distort and confuse the auroral electrojet magnetic variation picture. The magnetic field is thus of limited use in explaining ionospheric and field-aligned currents and can be quite deceptive; but it is a valuable tool for studying the dynamics of electrojets and as a restraint for current models. However, when the driving mechanism of the auroral electrojet and the entire current flow path become known then magnetic field variations can be used to delineate the ionosphere current system and its interaction with the magnetosphere.

The magnetic field of a distributed current system can be calculated from the Biot-Savart law for comparison with the observed magnetic field. The expression for the magnetic field throughout the region both inside and outside of the current is given by Stratton (1941),

$$\vec{B} = \frac{1}{4\pi} \int_v \vec{j} \times \vec{\nabla} \left(\frac{1}{\ell}\right) dv \qquad (3.18)$$

where ℓ is the radial distance from the point of observation to the current element j. The expression requires a prohibitive amount of computation if the magnetic field is to be determined over the volume occupied by the distributed current system and observational sites. The calculation along a meridian for a cross section is less onerous and can be performed for comparison with the observations of a rocket-borne magnetometer passing through the current system of a

substorm. The magnetic fields that a rocket-borne magnetometer might see could be very complex, consisting of a nearly equal contribution from distributed Hall or Pedersen electrojets, field-aligned sheets, and Birkeland currents; and would thus require information of the magnitude and spatial and temporal extent of these currents for any models.

The model for the calculations of the magnetic field of the electrojet current system for comparison with ground based measurements of the magnetic field can be much simpler and the field need only be calculated along one dimension. The electrojet can be modelled by a distribution of currents along one dimension which for example is the sum of the east-west currents in each column and is,

$$Ji_m = \int dj_{im} \quad i = x,y \tag{3.19}$$

The components of the magnetic field are then given by,

$$B_x = \Sigma_i \frac{Jy_i\, h_i}{2\pi\, \ell_i^2} \sin\alpha \tag{3.20}$$

$$B_y = \Sigma_i \frac{Jx_i\, h_i}{2\pi\, \ell_i^2} \sin\alpha \tag{3.21}$$

$$B_z = \Sigma_i \frac{Jx_i\, d_i}{2\pi\, \ell_i^2} \sin\alpha \tag{3.22}$$

$$\ell = (h_i^2 + d_i^2)^{1/2} \sin\alpha \tag{3.23}$$

where Jx_i, Jy_i are the currents integrated over the column of equation 3.19, h_i is the height of the maximum current in the column while d_i is the distance to the column, and i for a typical cross section for the auroral zone might consist of 30 sections or columns of current. The angle α to the end of the line current corrects for end effects and need only be considered at the ends when a significant amount of current changes from horizontal to vertical flow.

The magnetic field of field-aligned currents is more complex but has been calculated by a method of elementary loops by Bonnevier et. al., (1970). The field can also be calculated from a dipole model with line currents flowing along the field lines. The magnetic field is then

$$\vec{B} = \frac{J}{4\pi} \int_c \frac{\vec{ds} \times \vec{\ell}}{\ell^3} \tag{3.24}$$

In a spherical coordinate system the components of ℓ and ds in the "observer's" coordinates are given by (Kisabeth, 1972),

$$\ell_\gamma = \gamma_0 \cos L - \gamma \tag{3.25}$$

$$\ell_\theta = \gamma_0 \cos\theta \sin\theta_0 \cos(\lambda-\lambda_0) - \gamma_0 \sin\theta \cos\theta_0 \tag{3.26}$$

$$\ell_\lambda = \gamma_0 \sin\theta_0 \sin(\lambda-\lambda_0) \tag{3.27}$$

$$ds_\gamma = ds_{\gamma_0} \cos L + ds_{\theta_0} (\sin\theta \cos\theta_0 \cos(\lambda-\lambda_0) - \cos\theta \sin\theta_0) \tag{3.25a}$$

$$ds_\theta = ds_{\gamma_0} (\cos\theta \sin\theta_0 \cos(\lambda-\lambda_0) - \sin\theta \cos\theta_0) + \tag{3.26a}$$

$$ds_{\theta_0} (\cos\theta \cos\theta_0 \cos(\lambda-\lambda_0) + \sin\theta \sin\theta_0)$$

$$ds_\lambda = ds_{\gamma_0} (-\sin\theta_0 \sin(\lambda-\lambda_0)) + ds_{\theta_0} (-\cos\theta_0 \sin(\lambda-\lambda_0)) \tag{3.27a}$$

where $\cos L = \cos\theta \cos\theta_0 + \sin\theta \sin\theta_0 \cos(\lambda-\lambda_0)$

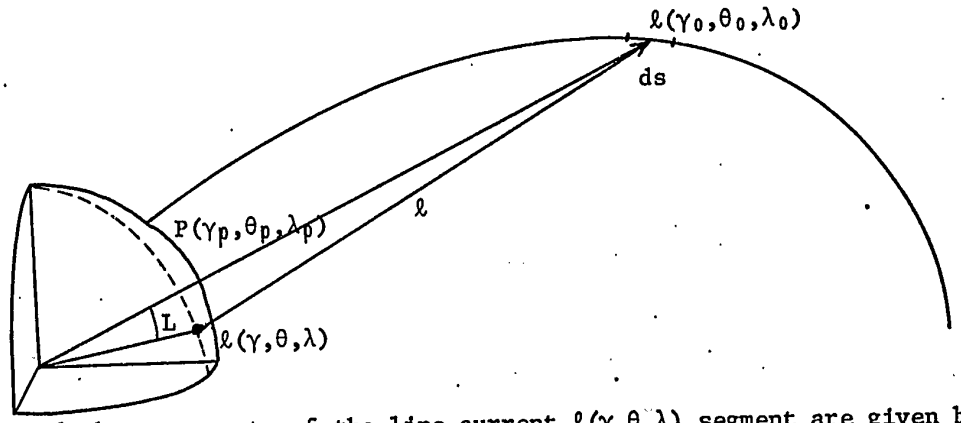

and the components of the line current $\ell(\gamma,\theta,\lambda)$ segment are given by,

$$ds = ds\left(\frac{df}{d\theta_0}\, d\theta_0,\ \gamma_0 d\theta_0, 0\right) \tag{3.28}$$

where the distance to the field line is a function of θ_0 and for a dipole field is given by,

$$\gamma_0 = f(\theta_0) = \gamma_r \sin^2\theta_0 \tag{3.29}$$

λ_0 is constant

where γ_r is the equatorial distance to the ring current. The magnetic field components of the field-aligned currents are,

$$B_x = B_\lambda = \frac{J}{4\pi} \int_c \frac{1}{\ell^3} (ds_\gamma \ell_\theta - ds_\theta \ell_\gamma) \tag{3.30}$$

$$B_y = B_\theta = \frac{J}{4\pi} \int_c \frac{1}{\ell^3} (ds_\lambda \ell_\gamma - ds_\gamma \ell_\lambda) \tag{3.31}$$

$$B_z = B_\gamma = \frac{J}{4\pi} \int_c \frac{1}{\ell^3} (ds_\theta \ell_\lambda - ds_\lambda \ell_\theta) \tag{3.32}$$

The magnetic field components of the field-aligned current in terms of the observer and the field-aligned current coordinates are,

$$B_x = \frac{J}{4\pi} \int_{\theta_0=\theta_p}^{\pi/2} \frac{1}{\ell^3} ((\cos\theta \sin\theta_0 \cos(\lambda-\lambda_0) - \sin\theta \sin\theta_0) \gamma_0 \, ds_\gamma$$

$$- (\gamma_0 \cos L - \gamma) \, ds_\theta) \tag{3.33}$$

$$B_y = \frac{J}{4\pi} \int_{\theta_0=\theta_p}^{\pi/2} \frac{1}{\ell^3} ((\gamma_0 \cos L - \gamma) \, ds_\lambda - \gamma_0 \sin\theta_0 \sin(\lambda-\lambda_0) \, ds_\gamma) \tag{3.34}$$

$$B_z = \frac{J}{4\pi} \int_{\theta_0=\theta_p}^{\pi/2} \frac{\gamma_0}{\ell^3} (\sin\theta_0 \sin(\lambda-\lambda_0) \, ds_\theta - (\cos\theta \sin\theta_0$$

$$\cos(\lambda-\lambda_0) - \sin\theta \sin\theta_0) \, ds_\lambda) \tag{3.35}$$

$$\text{where } \ell^3 = (\gamma_0^2 + \gamma^2 - 2\gamma_0\gamma (\cos\theta \cos\theta_0 + \sin\theta \sin\theta_0 \cos(\lambda-\lambda_0)))^{3/2} \tag{3.36}$$

and cosL, ds_γ , ds_θ and ds_λ are given by the above expressions.

When the plane of observation coincides with that of the field-aligned current, only the horizontal component B_x is present with a consequent reduction in calculation. The field-aligned current has a concentric circular magnetic field pattern in the horizontal plane which is enhanced on the equatorial side due to the inclination and curvature of the dipole field line. The contribution of the B_z component is small.

The ring current or the partial ring current of the magnetosphere return current path of the electrojet is at approximately 5 R_e and contributes a smooth latitude variation pattern at the earth's surface. This north-south or B_y component decreases with increasing

latitude and is zero at the poles for a symmetric ring current. The line current segment of a ring current and the magnetic field components are given by,

$$ds = ds\ (0,0,\gamma_0 d\lambda_0) \tag{3.37}$$

$$\theta_0 \approx \frac{\pi}{2} \tag{3.38}$$

$$\ell_\gamma = \gamma_0 \sin\theta \cos(\lambda-\lambda_0) - \gamma \tag{3.39}$$

$$\ell_\theta = \gamma_0 \cos\theta \cos(\lambda-\lambda_0) \tag{3.40}$$

$$\ell_\lambda = \gamma_0 \sin(\lambda-\lambda_0) \tag{3.41}$$

$$\ell^3 = (\gamma_0^2 + \gamma^2 - 2\gamma_0\gamma \sin\theta \cos(\lambda-\lambda_0))^{3/2} \tag{3.42}$$

$$B_x = 0 \tag{3.43}$$

$$B_y = \frac{J\gamma_0}{4\pi} \int_{\lambda_0=\lambda}^{\lambda_p} \frac{1}{\ell^3} (\gamma_0 \sin\theta \cos(\lambda-\lambda_0) - \gamma)\, d\lambda_0 \tag{3.44}$$

$$B_z = \frac{J\gamma_0}{4\pi} \int_{\lambda_0=\lambda}^{\lambda_p} \frac{1}{\ell^3} \gamma_0 \cos\theta \cos(\lambda-\lambda_0)\, d\lambda_0 \tag{3.45}$$

The east-west or B_x component of a symmetric ring current is also zero as is the B_x component along the demarcation line of a partial ring current. The demarcation line is where there is no east-west (B_x or D) variation for a polar substorm (Rostoker, 1966). For accurate comparison of the electrojet calculated solely from ionospheric measurements with that determined from ground based magnetic observations, corrections for induction must be made. These induced currents which arise from the varying source fields contribute to the magnetic variation and it is desirable to separate the induced and electrojet effects. The separation can be performed by potential theory or by reiteration which is probably more appropriate for limited data. However, for completeness, the expression for a potential separation of two dimensional fields is given by (Price, 1967),

$$(By_e - By_i)p = -\frac{1}{\pi} \int_{-\infty}^{\infty} \frac{B_z(y)\, dy}{y - y_p} \tag{3.46}$$

$$(Bz_e - Bz_i)p = -\frac{1}{\pi} \int_{-\infty}^{\infty} \frac{B_y(y)\, dy}{y - y_p} \tag{3.47}$$

where e, i refer to the external and internal components at the location p. A simple method was developed using reiteration, a fixed depth for the induced currents and line and sheet current models for both the source current and the induced current. The method was to fit a sheet current to the external and internal models then fit line currents to the difference and repeat the process, normally

5-10 times, until the magnetic fields from the two current systems were within a few nanoteslas (gammas) of the observed field.

The sheet current calculated in the first part of the iteration loop for each observation is,

$$J(y) = J(y)^1 + \frac{1}{2\pi} (By_o - By_c) \tag{3.48}$$

where $J(y)^1$ is the current calculated from the previous iteration and o and c are the observed and calculated field from the old iteration. The magnetic field is then calculated for each of the observations from the expression 3.21 for multiple line currents. In the next step the current is calculated at each station, assuming line sources above and below the station, from,

$$J(y) = J(y)^1 + 2\pi (By_o - By_c) h \tag{3.49}$$

where h is the distance to the current source, which was taken as the height at which the maximum current occurred, generally 110 km, while the depth for induction was 200 + h. The magnetic field was again calculated for the new system of currents then the iteration continued with the sheet current model. The sheet current model was found necessary to prevent the method from oscillating. The method fits a line current at each observation. For a smooth distribution across an auroral zone section, observations approximately every 100 km are necessary so an interpolation was performed on the sparse magnetic observations. The interpolation consists of approximation

by ratios of polynomials to obtain the magnetic field components at intervals of 100 km from the observations which were often separated by 200 km or more. The IBM scientific subroutine ACFI (1970) would fit a polynomial to within a few percent of the observations across the magnetic profile section. The above induction correction was then performed on the interpolated data to obtain the smoothed latitudinal distribution of the electrojet current system.

3.3 Current Interactions with the Ionosphere

The electric field that penetrates the ionosphere causing currents in the E region will also cause winds in the F region by means of ion drag forces, which in turn will affect the distribution of ionization in the F layer. In the lower E region neutral winds are caused by the currents which also heat the ionosphere. Significant heating also occurs during auroral displays by the absorption of energy from the precipitating charged particles. The winds and heating effects of currents and electric fieldscan be significant and are important parameters in the physics and dynamics of the upper atmosphere; as well, they can have a feedback effect on the currents by altering the conductivity. The general influence can be calculated from approximate expressions but the hydrodynamic equations of motion, which are coupled by the drag terms, must be solved for a more complete understanding.

From an alternative expression, an ionospheric current is given as,

$$\vec{J} = \sigma_1 \vec{E}^1 + \frac{\sigma_2}{B} \vec{B} \times \vec{E} \tag{3.50}$$

where $$\vec{E}^1 = \vec{E} + \vec{V} \times \vec{B} \tag{3.51}$$

and $$\vec{E} \cdot \vec{B} = 0 \tag{3.52}$$

and for a fluid,

$$\rho \frac{d\vec{V}}{dt} = \vec{F} + \vec{J} \times \vec{B} \tag{3.53}$$

where ρ = density, F = mechanical force. Cole(1971) gets a neutral wind velocity of,

$$\vec{V} = \frac{\vec{E} \times \vec{B}}{B^2} + \frac{R_1}{B^2} (\vec{F}_\perp - \frac{d\vec{V}_\perp}{dt}) + \frac{R_2}{B^2} \vec{B} \times (\vec{F} - \frac{d\vec{V}}{dt}) \tag{3.54}$$

where $$R_1 = \frac{\sigma_1}{\sigma_1^2 + \sigma_2^2} \tag{3.55}$$

$$R_2 = \frac{\sigma_2}{\sigma_1^2 + \sigma_2^2} \tag{3.56}$$

The steady state expression is then,

$$\vec{V} = \frac{\vec{E} \times \vec{B}}{B^2} + \frac{R_1 \vec{F}_\perp}{B^2} + R_2 \frac{\vec{B} \times \vec{F}}{B^2} \tag{3.57}$$

The mechanical forces involve Coriolis and gravitational acceleration, ion drag, tides and viscosity. The ion drag, (F_i), and viscosity, (F_μ), are the only significant forces in the vicinity of a major auroral substorm and are given by,

$$F_i = m\nu_{in} (V_i - V_n) \tag{3.58}$$

$$F_\mu = \frac{m\mu}{\rho} \frac{\partial^2 V_n}{\partial z^2} \tag{3.59}$$

where μ is the coefficient of viscosity which is calculated in the atmosphere program of section 2.7. The time constant to approach the steady state is also given by Cole (1971) as,

$$\alpha^{-1} = \frac{\rho}{\sigma_1 B^2} \tag{3.60}$$

The amplitude, extent, and duration of ionospheric winds can then be calculated throughout the ionosphere for the model auroral zone ionospheres and electric fields.

The heat produced by the system in the form of Joule dissipation of electric currents is given by,

$$Q = \vec{j} \cdot \vec{E} = \sigma_1 E^2 \tag{3.61}$$

which also can be calculated throughout the current system models and compared with other sources. The temperature rise resulting from Joule heating and absorption of energetic charged particles could

be calculated from the heat balance equation, but uncertainties in loss and transport mechanisms at present are too large.

The computer program flow diagram for the calculation of the meridian profile is shown in Figure 3.3. The appropriate ionosphere models calculated by the program in section 2.7, are read from the magnetic tape and stored; the current, winds and heating are then calculated as a function of height for each profile and stored. The integrated currents are checked against the current calculated from the integrated conductivity and average electric fields for the profile. The magnetic field of the ionosphere-electric field model is calculated and compared with the observed magnetic field variation which has been corrected for currents induced in the earth.

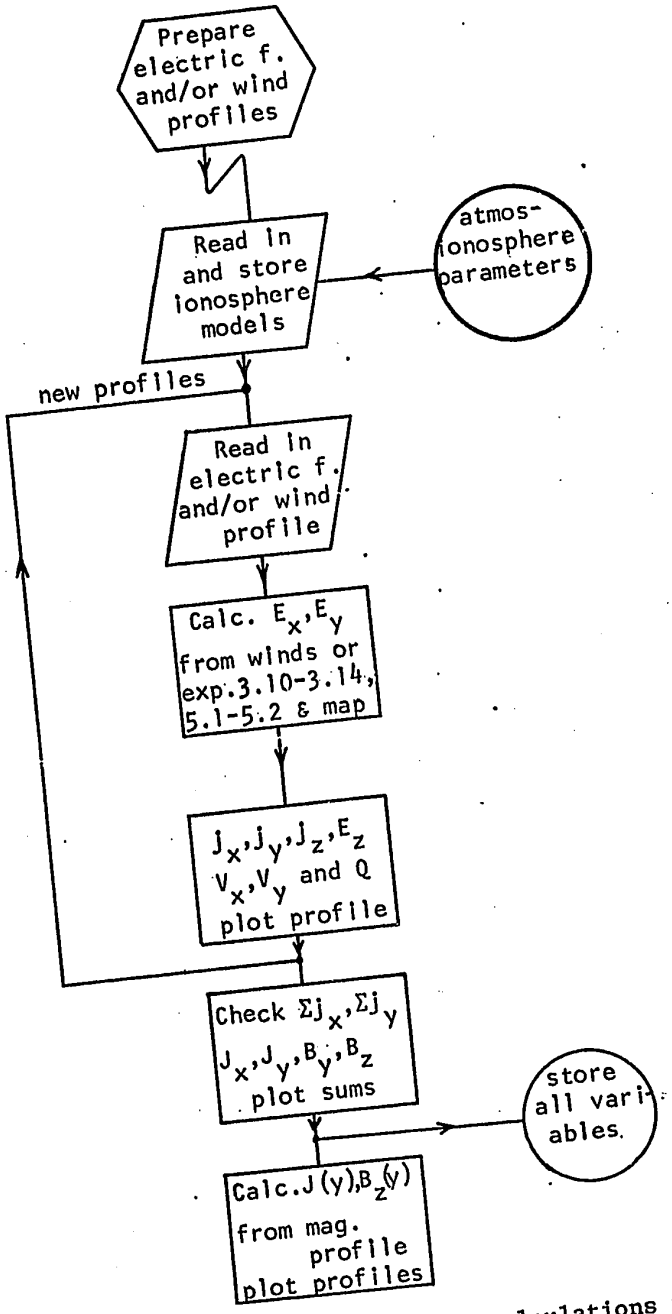

Figure 3.3 Flow diagram of the calculations for the currents, winds and heating for a meridional section.

CHAPTER 4

CURRENT FLOW FOR AURORAL MODELS

The current flow in an auroral electrojet can now be calculated from detailed models of the electron density and electric fields in a disturbed auroral ionosphere. An auroral ionosphere model is constructed by combining the appropriate height profiles of the electron density corresponding to the arc brightness and width across the auroral zone. The electron density profiles have been constructed in section 2.51 from observations and in 2.53 from theoretical considerations of electron equilibrium conditions. The cross section of the auroral oval in the meridian plane can be modelled incorporating such features as multiple arcs with varying widths and brightnesses to quiet conditions with no visible aurora. The conductivity, electron and ion temperatures, and other parameters have been calculated for each profile so auroral models of these variables are also available directly from the model of the auroral ionosphere. The electric field must be modelled from the limited observations or theoretical expectations of the current flow or electric field behavior across arcs. Because in the ionosphere conductivity is a second order tensor and the electric field is a vector, many combinations of these variables are possible, each resulting in different current patterns. Simple models showing the current flow patterns for a Pedersen (direct) type of electrojet and for a Hall current are developed. The current flow resulting from a combined Pedersen and Hall current system is also modelled.

4.1 The Ionosphere Model

The ionosphere model was constructed from the analytic expression 2.62 for the electron density as a function of height and auroral brightness rather than from observations which have generally not been related to the auroral brightness. The model is intended to show the general characteristics of a quiescent auroral ionosphere consisting of two arcs. The two simple identical arcs which are shown in Figure 4.1 have a width of 10 km, and an apparent brightness of 50 kR with symmetrical side lobes of luminosity due to scattering of the precipitating electrons. The peak volume emission rate of the arc is 50 Gp/m^3s (gigaphotons per cubic metre second) while the side lobes consist of 3 columns of 5 km width with emission rates of 20, 10 and 5 Gp/m^3s. Enhanced regions are observed to the north and south of arcs for 500 km or more and are modelled by 1 and 2 Gp/m^3s auroral glows on either side of the arcs. The emission rates are for the bright green auroral atomic oxygen line at $\lambda 5577$. The electron density of the double arc ionosphere model is contoured in Figure 4.1. The arcs have peak electron densities of 0.9 T/m^3 at a height of 113 km.

The brightness of an arc is proportional to the width of the arc for a fixed volume emission rate so that two arcs which have apparent brightnesses of 100 kR could result in different electrojets from similar electric fields. The first 100 kR arc, for example, could be 20 km wide with a peak volume emission rate of 50 Gp/m^3s while a second arc could be 10 km wide with a volume emission rate of 100 Gp/m^3s. If the electric field in an arc is

inversely proportional to the peak volume emission rate of the arc (Aggson, 1967), then the first arc would carry twice the current of the second, thinner but more intense arc. Variation in the direction and magnitude of the electric field offers sufficient complexity so that only the simpler model of two identical arcs will be considered for the study of current flows.

The conductivity for the ionospheric model shown in Figure 4.1 has been calculated using the procedure developed in Chapter 2 and the neutral atmosphere discussed in section 2.4. The specific (parallel) conductivity is contoured in Figure 4.2. The arcs and magnetic field lines are assumed vertical instead of being inclined 7° toward the equator. The specific conductivity increases rapidly with height throughout the auroral E region of the ionosphere. The specific conductivity in an arc is enhanced by approximately a factor of 5 in the E region and a factor of 3 in the F1 region to a value of 30 S/m (siemens per metre) at 230 km. The contours of the Pedersen conductivity are shown in Figure 4.3 for the ionosphere of Figure 4.1. The maximum value of the Pedersen conductivity in the arc occurs at 125 km and is 0.84 mS/m. The conductivity in the arc is about a factor of 5 greater than in the E region adjacent to the arc, while in the F region the ratio is 3:1. The magnitude of the Pedersen conductivity at 230 km in the arc is 17 μS/m. The Hall affect conductivity contours are shown in Figure 4.4 for the ionosphere of Figure 4.1. The Hall conductivity reaches a maximum of 2.5 mS/m at 110 km and is approximately 3 times greater than the peak value of the Pedersen conductivity,

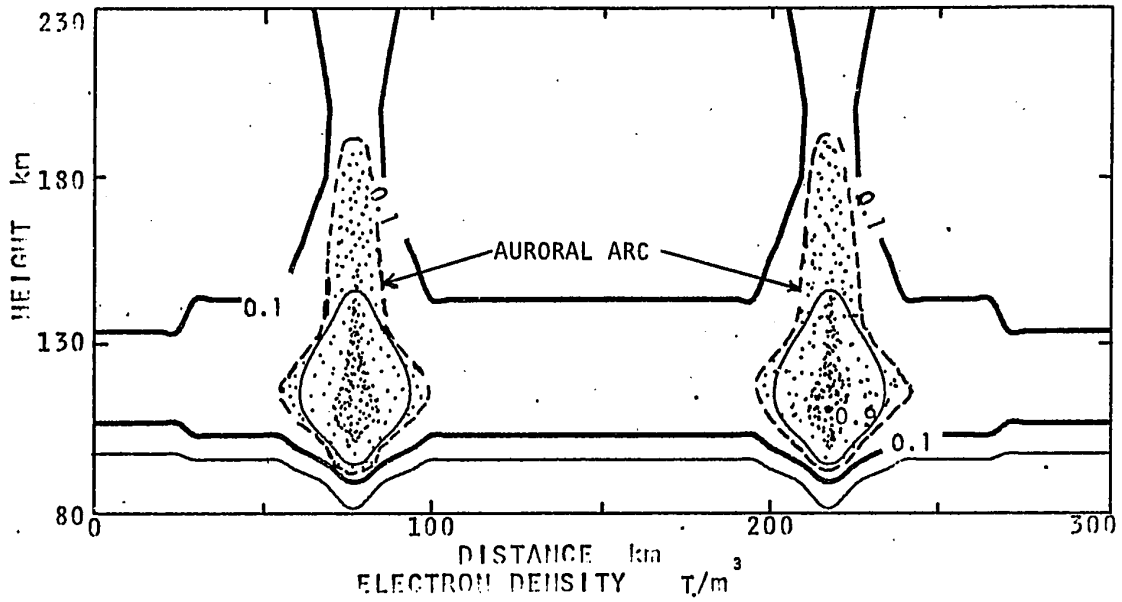

Figure 4.1 Contours of the logarithm of electron density of a meridional cross ... section having two identical auroral arcs of 50 kR. The outline of the arcs are shaded.

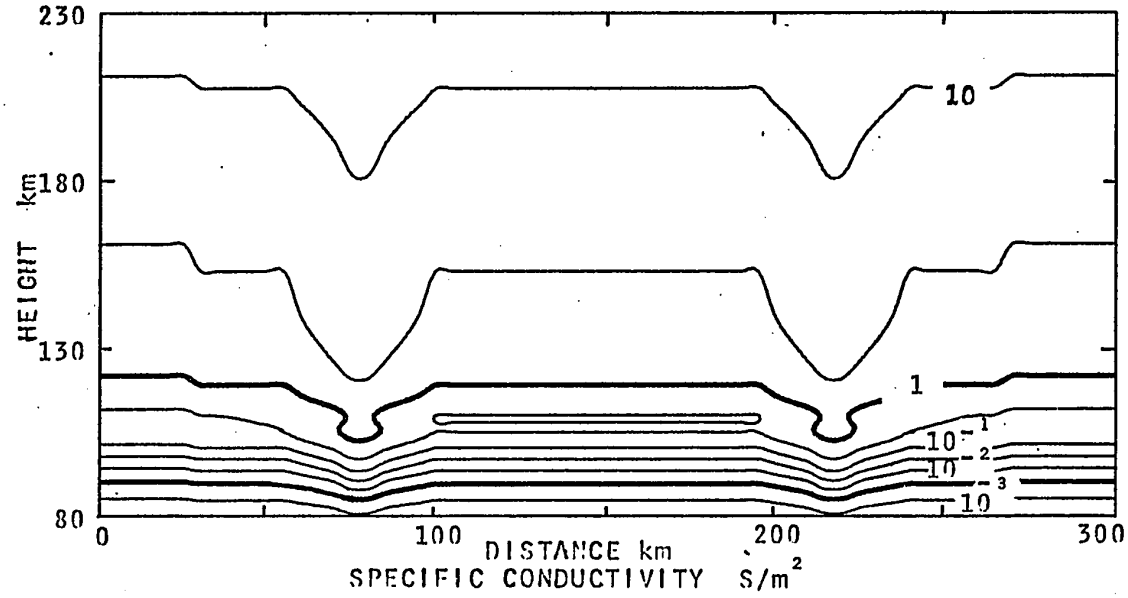

Figure 4.2 The specific (parallel) conductivity of the ionospheric section of Figure 4.1, , contoured on a logarithmic scale.

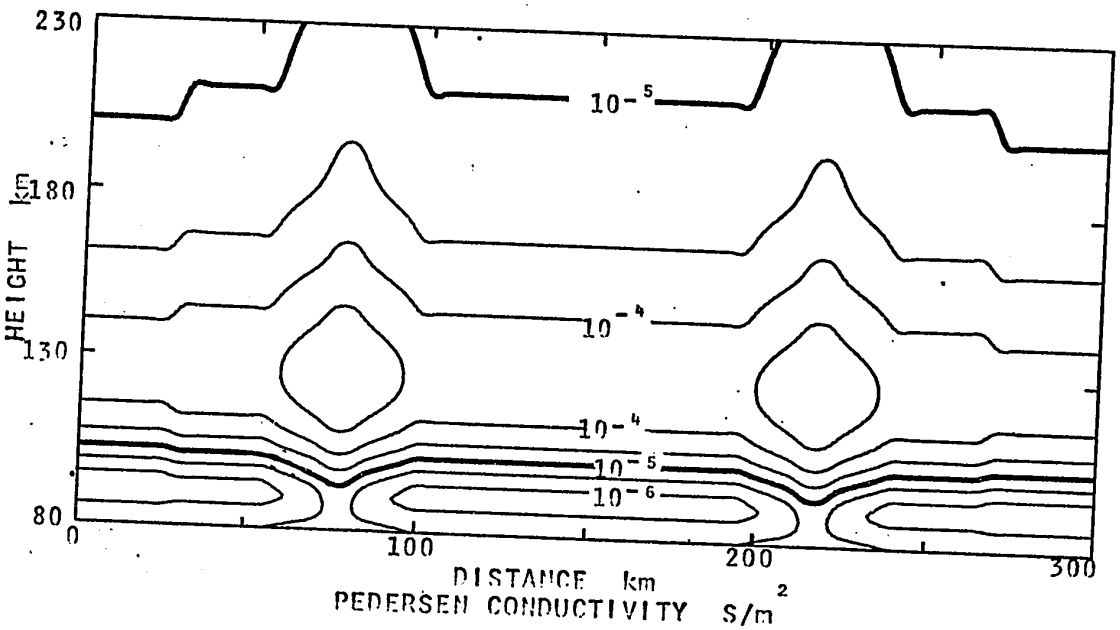

Figure 4.3 The logarithm of the Pedersen conductivity, contoured for the meridional section of Figure 4.1.

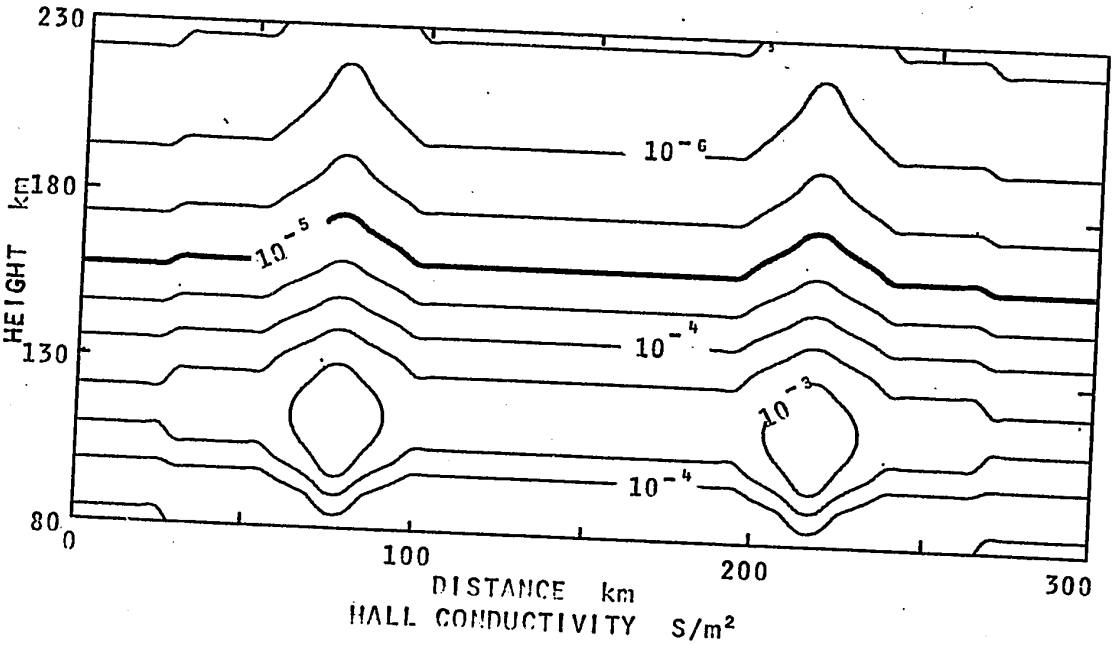

Figure 4.4 The Hall conductivity of the meridional section of Figure 4.1 , contoured on a logarithmic scale.

but at 100 km the Hall conductivity is 7 times greater than the Pedersen conductivity. However, the Pedersen conductivity dominates the Hall conductivity above 130 km. The different types of auroral forms result from differing electron precipitation patterns which will produce dissimilar auroral ionospheres and resultant conductivity profiles and ratios.

The variation of the components of the conductivity normal to the magnetic field can be seen in Figure 4.5 for the same auroral section. In this figure the logarithm of the Hall and Pedersen components of the conductivity has been used for plotting the arrows. The lengths of the arrows are proportional to the currents if the electric field is constant across the section. The electric field is westward in Figure 4.5 with its Pedersen current component, which is directed into the paper, rotated 90° to the vertical for plotting. The arrows are in the meridian plane at 100 km, representing the dominance of the Hall component, but quickly rotate to the west above 130 km where the Pedersen conductivity is largest. The enhanced conductivity in the arcs is apparent from the longer arrows. Similarily a constant northward electric field has the eastward Hall component controlling the current below 130 km. The northward meridian current dominates above 200 km in Figure 4.6. The integrated conductivities for the auroral section of Figure 4.1 between 80 and 230 km are shown in Figure 4.7.

The integrated Hall conductivity is 2.5 times that of the Pedersen conductivity but the integrated specific conductivity is approximately 10^4 that of the Hall conductivity. The ratios of the

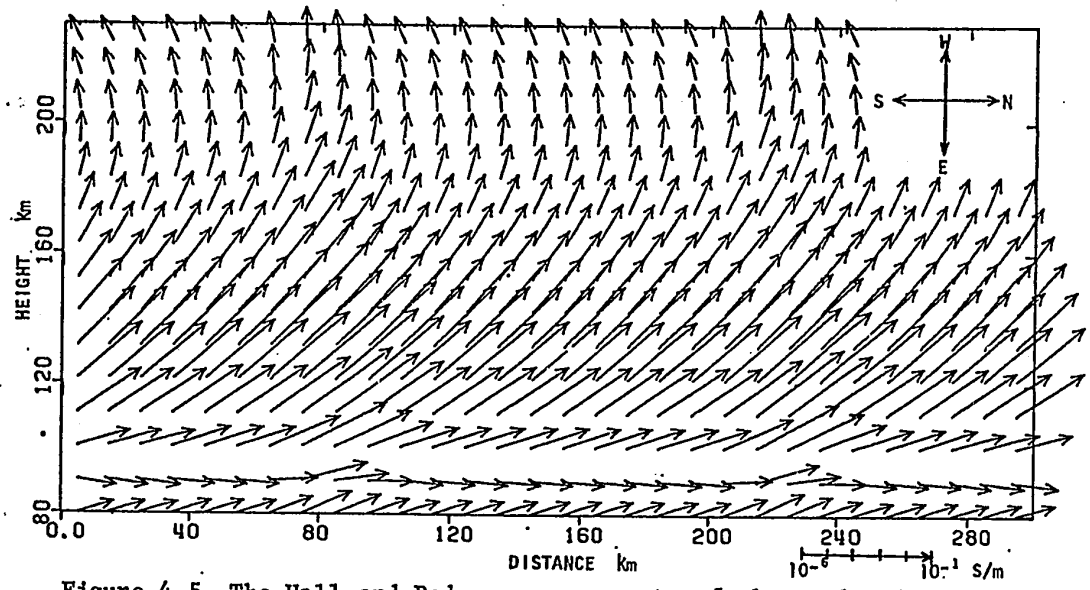

Figure 4.5 The Hall and Pedersen components of the conductivity tensor represented by arrows for a westward electric field. The Pedersen component is in the direction of the electric field, which is westward, and has been rotated 90° to the vertical for plotting. The logarithm of the components is plotted.

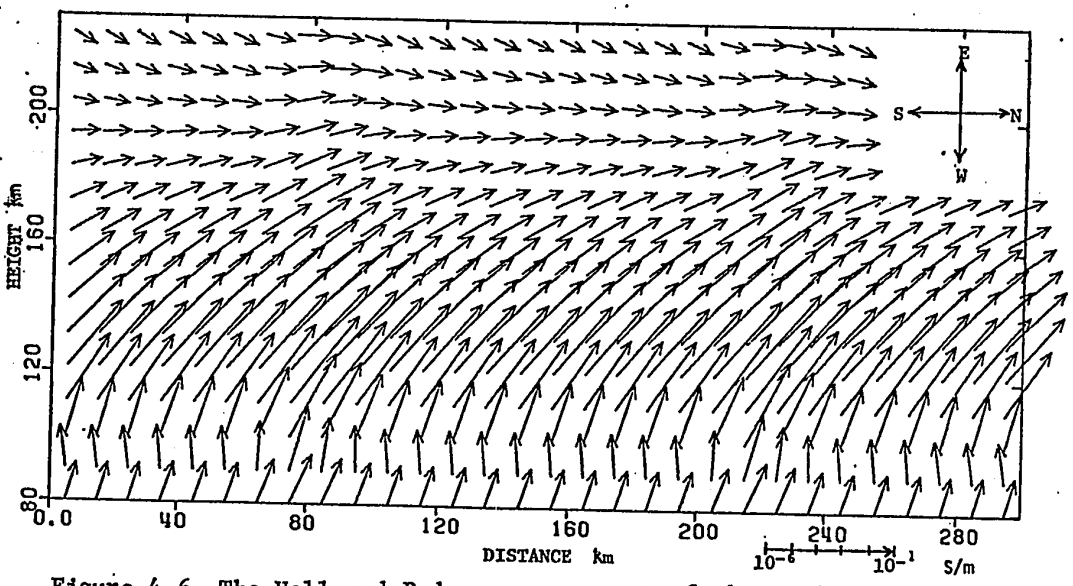

Figure 4.6 The Hall and Pedersen component of the conductivity tensor are represented by arrows the same as in Figure45 but with the electric field in the north or meridian direction. The Hall component is towards the east and has been rotated 90° to the vertical for plotting.

integrated Hall and Pedersen conductivity are nearly the same for all types of auroral columns due to the simple expression 2.62 for the electron density profiles. The Hall conductivity inside the arc is a factor of 7 greater than in the immediate region surrounding the arc while the Pedersen conductivity shows an increase of 5. Electric fields applied to any of these ionosphere profiles will result in currents differing from each other only in magnitude. The horizontal current vector will rotate with increasing height and change in magnitude as seen in Figures 4.5 and 4.6 for an electric field which is constant with height and direction. The components of the current as a function of height are shown in Figure 4.8 for the column indicated by a P in Figures 4.9 and 4.10. The vertical electric field and the current with its vertical gradient are also shown in Figure 4.8. The field-aligned current is determined from the divergence-free condition and is consequently a function of the horizontal current flow across the column boundary as well as the conductivity and electric field within the column. The Hall current in the meridian, j_y, is greatest while the westward electrojet, j_x, is being driven by only a westward electric field of 5 mV/m.

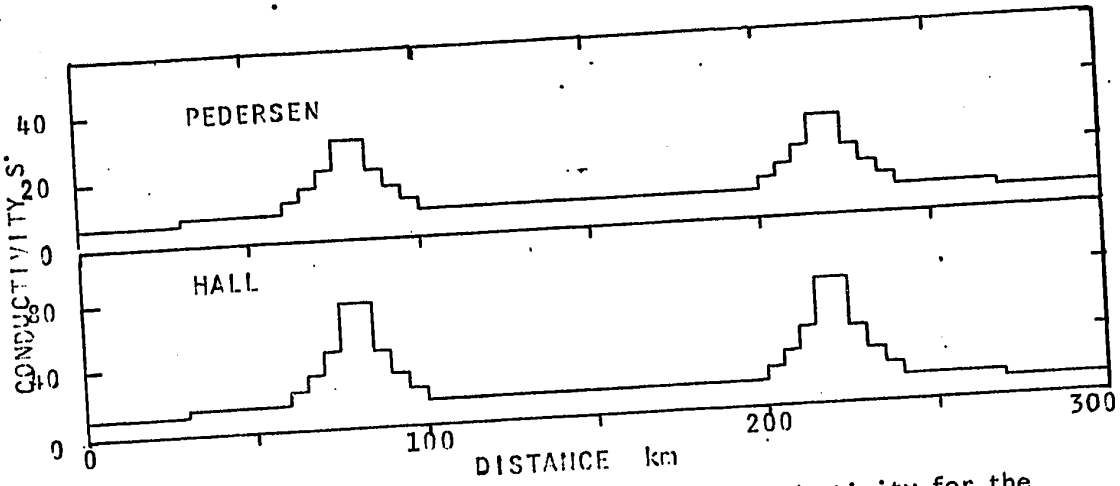

Figure 4.7 The integrated Pedersen and Hall conductivity for the meridian section of Figure 4.1 with the "steps" corresponding to the columns of the model.

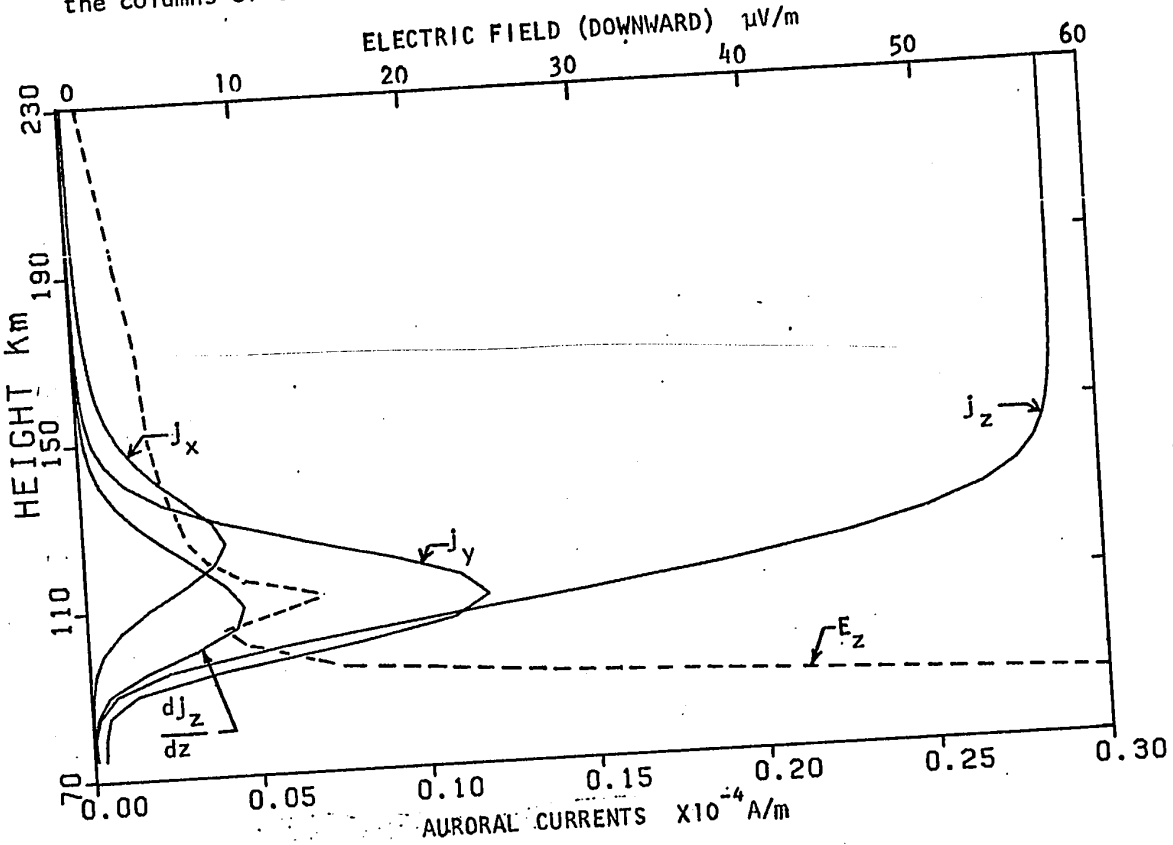

Figure 4.8 A typical height profile of the components of the current and the rate of change of the vertical component of current with height for section P in Figures 4.9 and 4.10. The vertical electric field is dashed and requires the top scale.

4.2 Current Distributions for Constant Electric Fields

The current flow through the auroral section for the simple case when the electric field is constant across the arc is shown in Figures 4.9 and 4.10. The two cases for the auroral electrojet consisting only of a Hall current and a Pedersen current are shown for each arc in the figures. The current distribution, assuming constant electric fields, could result from steady winds blowing across the arcs or a magnetospheric source which overwhelms any ionospheric effects or is isolated from any return current effects. An induced field of the equivalent of 5 mV/m could result from a 100 m/s wind in the E region of the ionosphere if no polarization occurs. Other possible sources of the electric field are the solar wind streaming past the magnetosphere causing a dawn to dusk electric field across the tail or convection within the magnetosphere. The contours of the two types of electrojets in Figure 4.9 show the currents confined mostly to the arcs. The Hall current is approximately 3 times greater in strength than the Pedersen current and occurs lower in the E region of the ionosphere. The Hall current density inside the arcs is 6 times that of the ambient region. The flow of current across the electrojet and along the magnetic field lines for the two cases is shown in Figure 4.10 for the electrojets of Figure 4.9. The flow across the direct current electrojet (indicated by a P at 80 km) is a Hall current and for the westward electrojet the northward Hall current must have a downward field aligned sheet current on the equatorial edge and vertical field aligned current on the polar side of the arc.

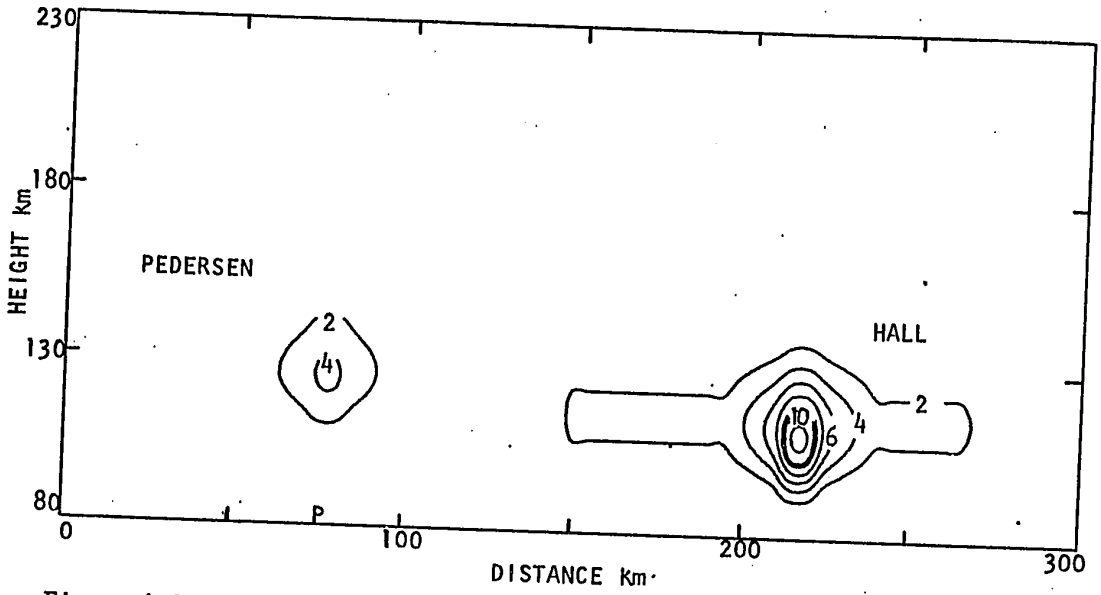

Figure 4.9 Contours of the current density of a meridional section of an auroral zone with a 5 mV/m constant electric field across the arcs driving a direct (4μA/m) and Hall (12μA/m) electrojets.

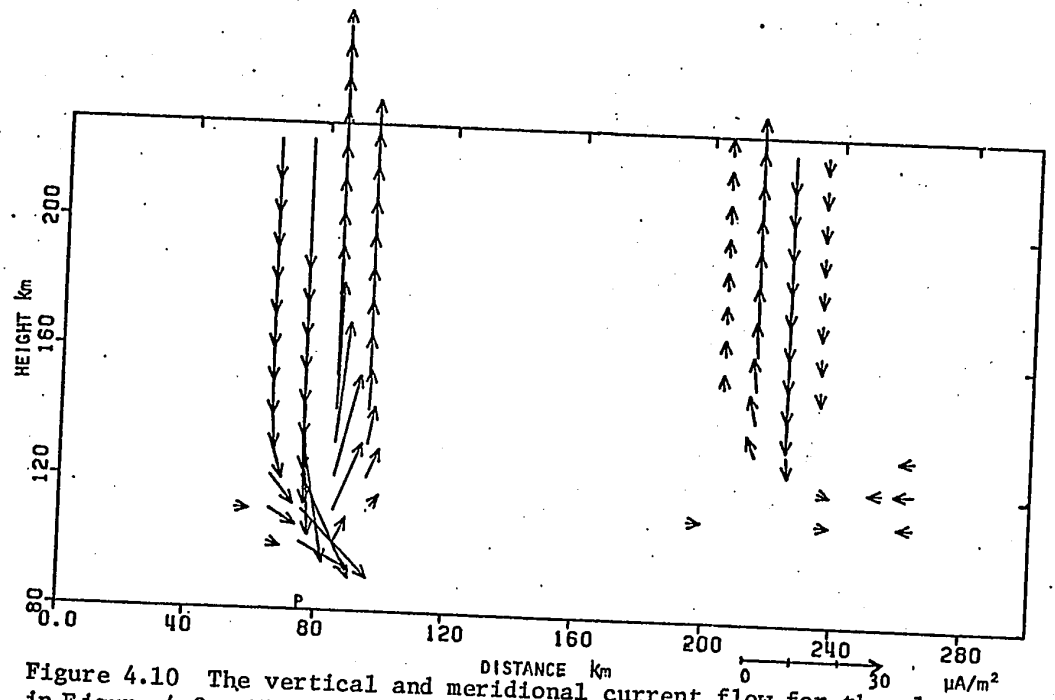

Figure 4.10 The vertical and meridional current flow for the electrojets in Figure 4.9. The direct current model at P has the larger field-aligned currents which result from the Hall meridional current.

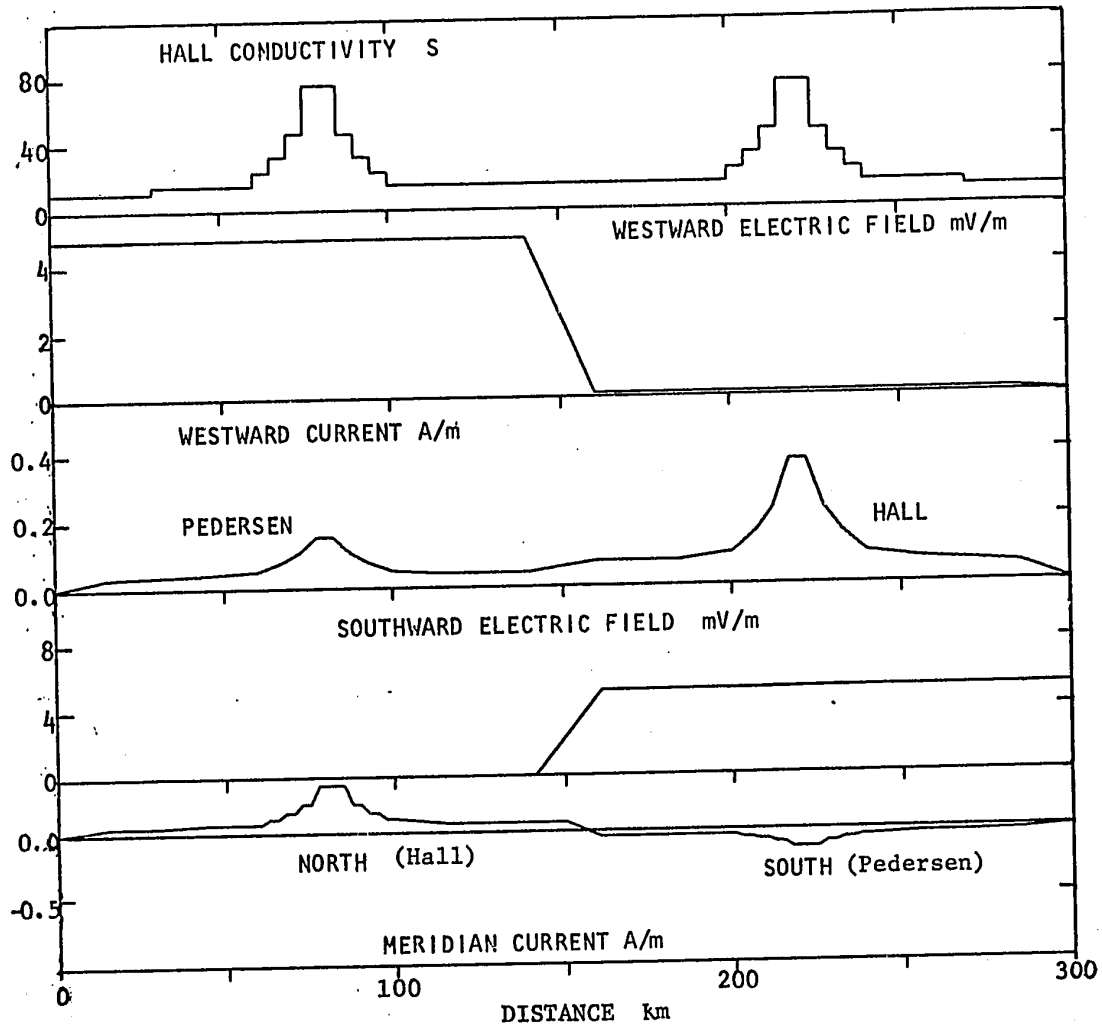

Figure 4.11 The distribution of the integrated currents and average electric fields for the currents in Figures 4.9 and 4.10. The location of the arcs is indicated by the total Hall current for the section.

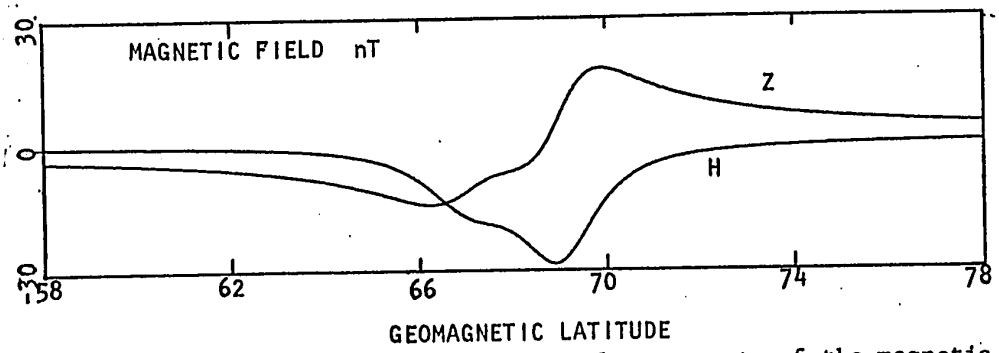

Figure 4.12 The horizontal and vertical components of the magnetic field for the current model of Figure 4.9 with the -29 nT peak corresponding to the Hall electrojet.

These field-aligned currents are a direct result of the reduced conductivity and/or electric field outside the auroral zone or arc. The flow of current across the Hall electrojet is a Pedersen current which is in the opposite direction to the previous case, flowing down the field lines on the northern edge, south across the arc, then up the field lines on the southern side. The magnitude is approximately a factor of 3 less than for the previous Hall cross current. The integrated horizontal currents for the section are shown in Figure 4.11. The electric field and current as a function of distance across the section for the direct and Hall electrojets are in the upper figure while the lower figure shows the current in the meridian plane. The magnitudes of the two different electrojets can be readily compared in Figures 4.9 - 4.12 for the case of constant electric fields across the auroal zone and the arcs. The perturbation magnetic field produced by the electrojet current distribution of Figure 4.9 is shown in Figure 4.12. The two currents have been separated an additional 100 km for the calculation of the H and Z magnetic field components simply to resolve the peaks and magnitudes associated with each arc. The separation of the currents is of no consequence for theoretical models, but the resolved magnetic fields for each electrojet aid in understanding the mechanisms involved and their relation to magnetic field observations of polar magnetic substorms.

The arrows shown in Figure 4.10 can be replaced by streamlines as they represent the magnitude and flow direction of planar vectors. Figure 4.12a shows the same information as Figure 4.10 but now the flow direction is indicated by the continuous curved arrow and the magnitude by the spacing width of the flow lines. The computer program was developed at NCAR (Lackman, 1970) and is a considerable advancement over representation by straight arrows or using two contour plots of the magnitude of each component.

In reality the electric field variation across the auroral zone is possibly due to current requirements (Boström, 1964) or proportional to the auroral brightness (Aggson, 1967). Observations of the electric field by satellites also show large spatial variation across the auroral zone (Cauffman and Gurnett, 1971). The observations of Aggson (1967) and Westcott et al.(1969) generally indicate an anticorrelation of the electric field with auroral brightness; thus the current system in the arc is perhaps some function of the arc brightness. Other reasonable conditions would be for the current to be nearly constant flowing across an arc with a small component flowing up the arc to compensate for the influx of electrons causing the arc. The constant current flowing across an arc is developed for the Pedersen and Hall driven electrojets. Polarization is thought to occur within the arc and is modelled for the case when the westward electric field is reduced within the arc. Models of these conditions were constructed using the same ionosphere in Figure 4.1 for the study of their current flows.

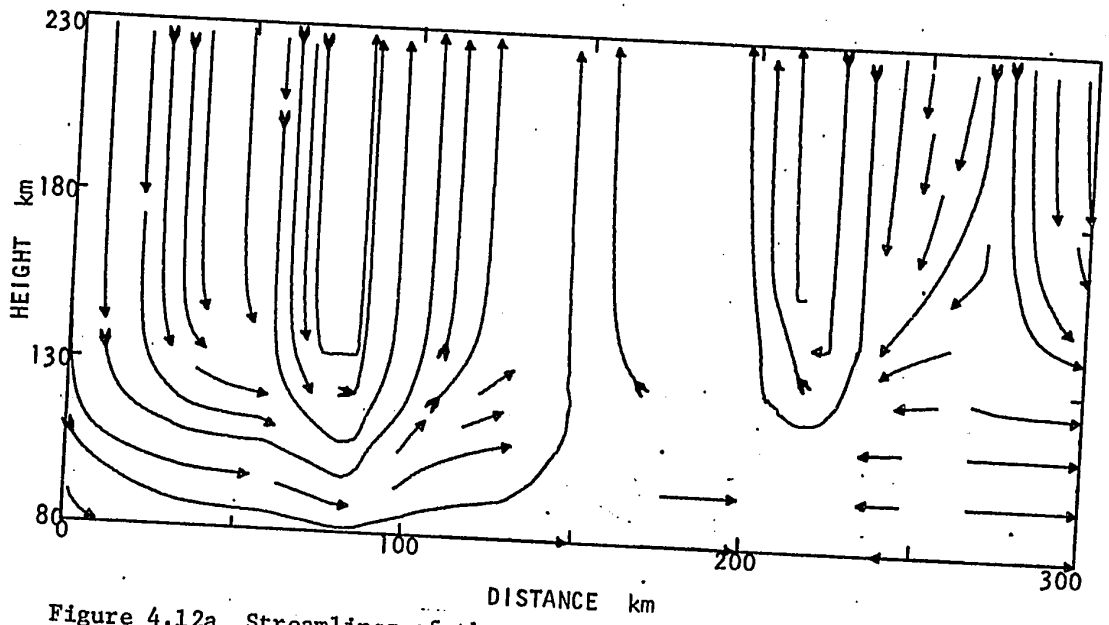

Figure 4.12a Streamlines of the meridional current flow in Figure 4.10. The arrows show the direction of flow while increasing current density is represented by streamlines closer together. Current flow is ∿0.29μA/m between streamlines.

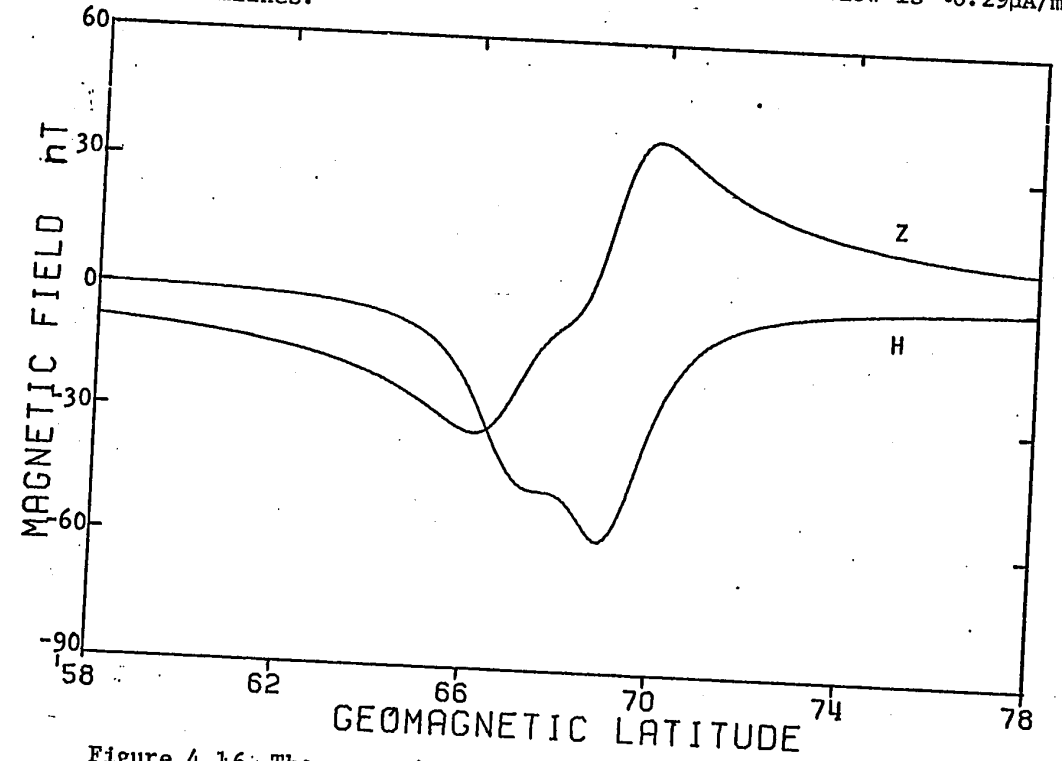

Figure 4.16 The magnetic field for the sheet and polarized model electrojets in Figures 4.13 - 4.15.

4.3 Pedersen Current Models

The same model ionosphere as in section 4.1 was used for constructing two types of Pedersen electrojets. The model for a meridional section of the Pedersen current driven by only a westward electric field and then by a combined westward and polarized electric field is contoured in Figure 4.13. The streamlines for the horizontal and vertical flowing currents are shown in Figure 4.14 while the average electric fields and integrated currents, and Hall conductivity for the section are shown in Figure 4.15. The westward electric field across the arc was continuously reduced towards the center of the arc such that the current density across the arc remained constant and equal to that outside the arc. The electric field in the immediate center of the arc was further reduced to simulate field aligned currents compensating the precipitating auroral electron flux. The maximum current density is 4 $\mu A/m^2$ while the integrated current is 0.16A/m and can be represented by a thin sheet approximately 150 km across at a height of 128 km with a total current of 23 kA. The magnetic field resulting from the sheet current ($\pm$45nT) is very similar to that of a line current (Walker, 1964) and is shown in Figure 4.16 superimposed with the magnetic field from the larger electrojet (-60 nT) which has the additional polarized electric field. The Hall meridional current flowing across the arc is nearly constant (Figure 4.15 bottom) when the westward electrojet is constant across the arc. The field-aligned current (Figure 4.14) flows downward on the equatorial side of the arc and upward on the polar side of the arc.

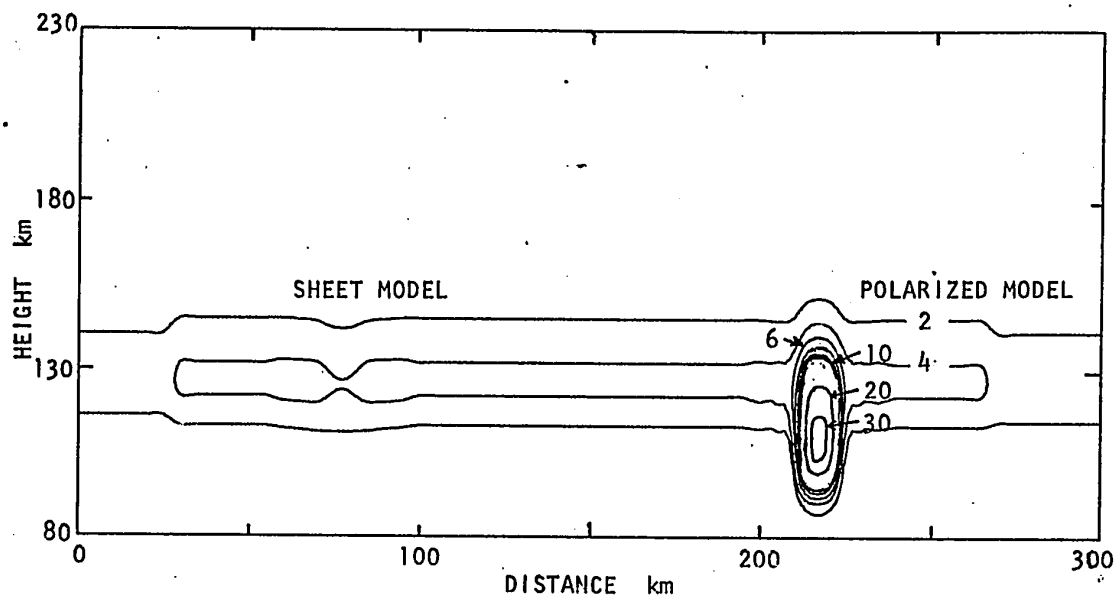

Figure 4.13 Contours of the current density for a Pedersen electrojet (4 μA/m) and a polarized electrojet (30 μA/m).

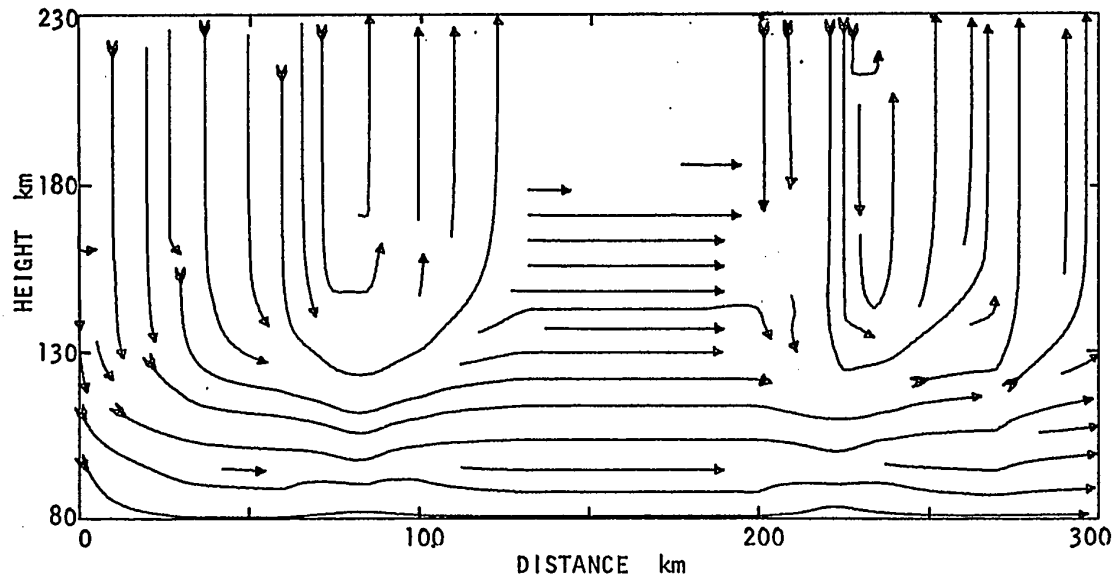

Figure 4.14 Streamlines of the meridional current flow for the auroral electrojets in Figure 4.13. Current flow is ∿0.18μA/m between streamlines.

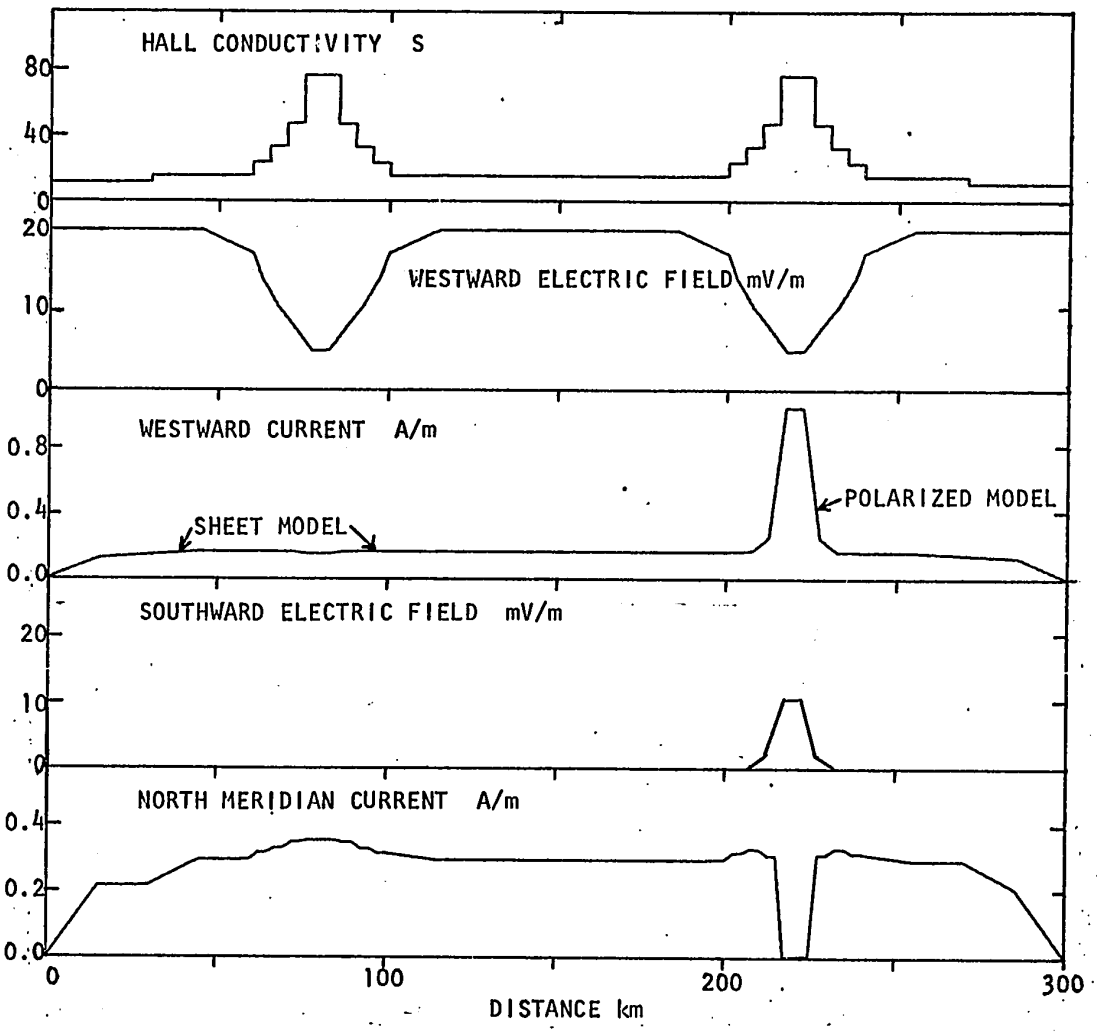

Figure 4.15 The components of the horizontal electric field and integrated current density and Hall conductivity as a function of the distance across the auroral zone. The models are for a direct westward sheet current and a polarized electrojet.

The westward electric field for the polarized electrojet in Figures 4.13 - 4.15 is the same as for the sheet current model; the polarizing electric field is in the meridian and is determined from expression 3.14. The induced polarized electric field is modelled for the central portion of the arc only and not for the wings or side lobes of the arc, which would cause an even more intense electrojet. The large polarized electric field results from the Hall to Pedersen ratio of the conductivity of 2.5 and adds a significant Hall current to the electrojet. The current inside the arc increases by a factor of 7 over that of the Pedersen sheet current model. The peak current density in the second arc (see Figure 4.13) is 30 $\mu A/m^2$ and the current integrated up the arc is 1.0A/m. The total current in the arc is 10.3 kA while the total current in the arc's adjacent regions is 22.7 kA. Large field-aligned currents occur at the edges of the arc to fulfill the current continuity conditions. The current is up the field lines on the equatorial side of the arc and down the field lines on the polar side. The current density of these field-aligned currents is approximately 50 $\mu A/m^2$, an order of magnitude more than for the field-aligned currents associated with the sheet current model. Field-aligned currents this large have been proposed by Armstrong and Zmuda (1970) to explain an 800 nT geomagnetic disturbance observed by a polar orbiting satellite at an altitude of 1100 km (see Figure 4.21). However the antiparallel currents were separated by 300 km and not the 10 km width of the arc. The total electric field in the polarized arc is 12.5 mV/m which is slightly higher than the ~5-10 mV/m that is generally observed. If polariz-

ation occurs it would have to be reduced in magnitude to probably not more than 30% of the value given by expression 3.14 to fit the present limits of observed electric fields and magnetic fields.

4.4 Hall Current Models

The electric fields of a transient nature observed in the vicinity of auroral arcs during substorms are generally directed southward with magnitudes ranging from 10 mV/m to 50 mV/m and occasionally more than 100 mV/m. These southward electric fields would cause a westward Hall current to flow in the vicinity of the arcs, and also within the arcs themselves, depending on the strength and direction of the electric field in the arc.

The model ionosphere consists of the same two parallel auroral arcs separated by about 130 km as in section 4.1. The variation in the electric field across the first arc is the same as that for the Pedersen sheet current model discussed in section 4.3, although, now it is purely southward in the meridional plane. The model in the second arc has the meridional current flowing across the arc which is constant in magnitude. The contours of current density for the two arcs are shown in Figure 4.17, and the streamlines for the meridional current flow are shown in Figure 4.18. The current systems for each arc are similar to the sheet current model shown in Figure 4.13 although the magnitudes of the Hall currents are greater by a factor of three. The first arc has a maximum current density of 11 $\mu A/m^2$ (see Figure 4.19) at 110 km, and the current density distribution as a function of height leads to a height-integrated density of 0.36 A/m and a total current within the 10 km wide arc of 3.6 kA. The height-

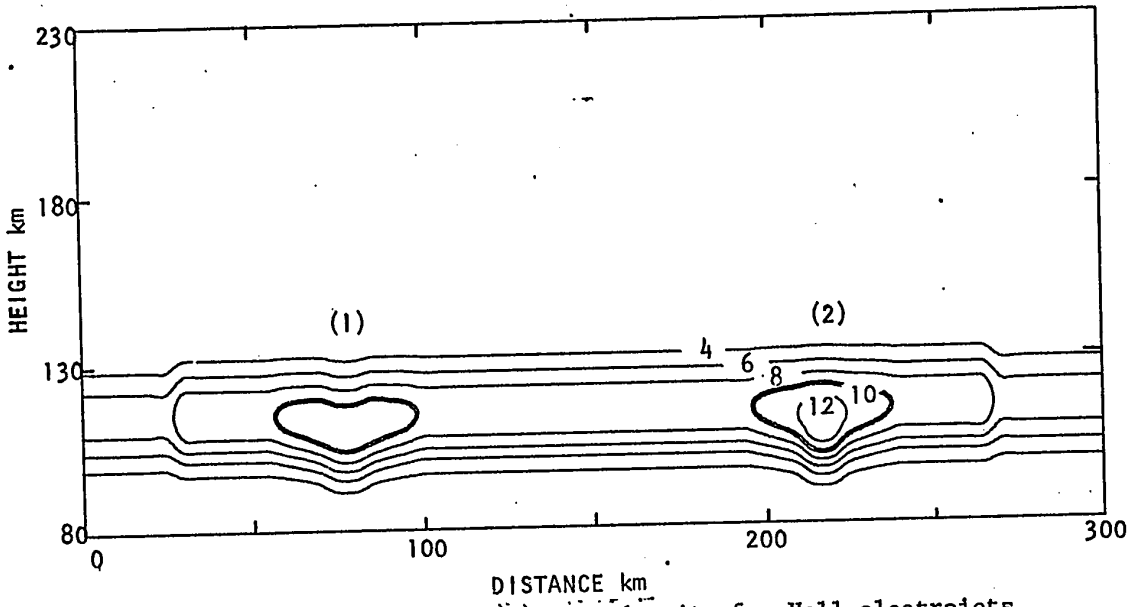

Figure 4.17 Contours of the current density for Hall electrojets resulting from (1) a meridian electric field the same as for the direct sheet current model and (2) a constant meridional electric field across the arc (12 μA/m).

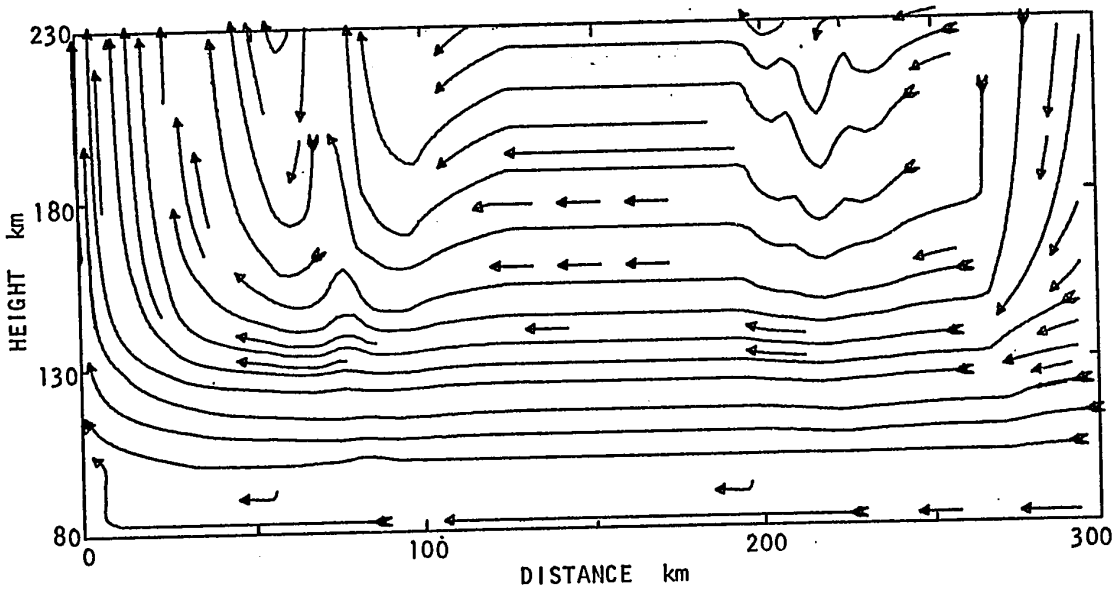

Figure 4.18 Streamlines of the meridional current flow for the Hall electrojets in Figure 4.17. Current flow is ∿0.57μA/m between streamlines.

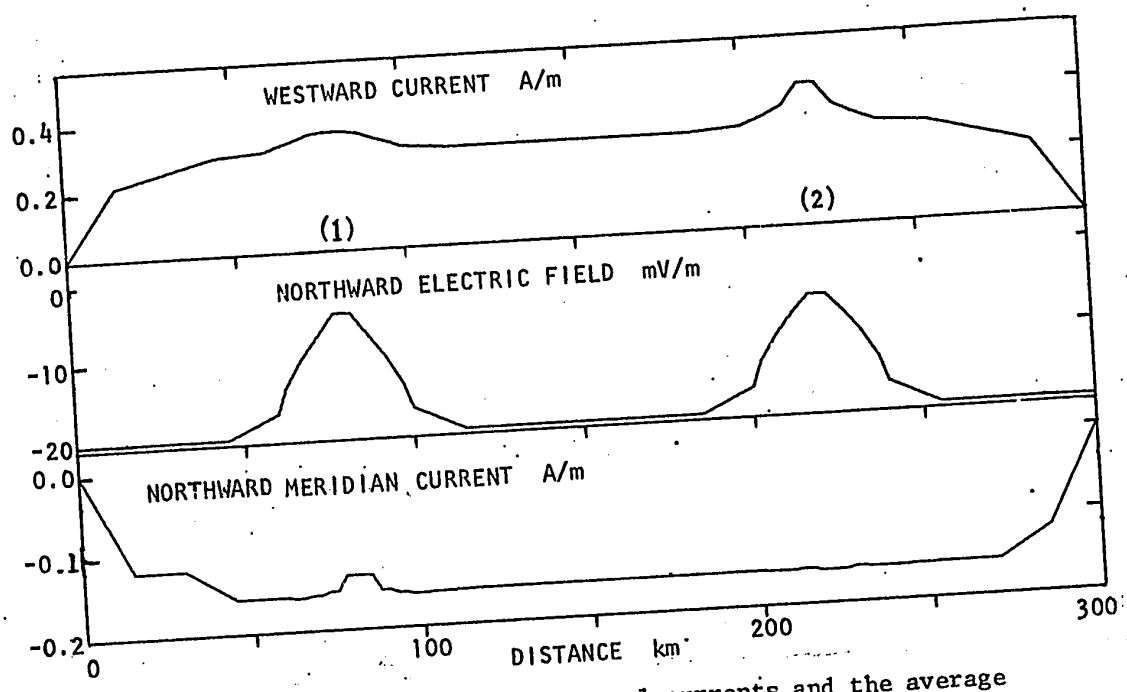

Figure 4.19 The integrated horizontal currents and the average meridional electric field across the arcs for the Hall electrojet models of Figure 4.17.

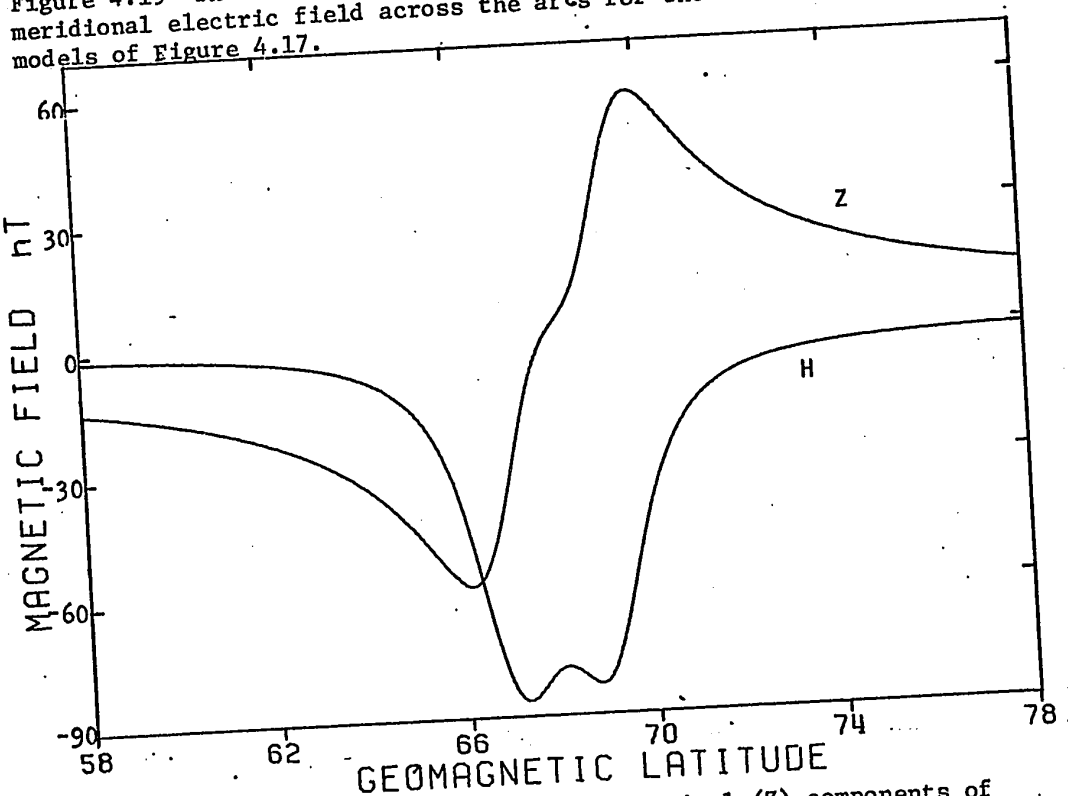

Figure 4.20 The horizontal (H) and vertical (Z) components of the magnetic field of the Hall electrojet models in Figures 4.17-4.19.

integrated current density in the region surrounding the arc is 0.3 A/m, however the total current flowing in this region is 40 kA which is a factor of 11 greater than the total current within the arc. This large ratio results from the larger size of the adjacent region and the more intense electric field in that region. The total current which may flow, assuming the Hall current model, is twice that which may flow assuming the Pedersen current model for a given magnitude of the electric field and the ionosphere model of section 4.1. For the Hall current model, vertical sheet currents flow up the field lines on the equatorial side of the inner edge of the arc and down the field lines on the poleward side. However the field-aligned current directions are reversed on the outer edges of the arc. The magnetic field perturbation pattern for this current system is shown in Figure 4.20 and features a peak magnitude of -82 nT at the earth's surface. The current system associated with the second arc shown in Figure 4.17 produces a maximum magnetic field perturbation of -86 nT.

The antiparallel currents flowing vertically in the arc probably do not exist; none have been observed, and they can be eliminated from the first Hall current model by having the meridional current constant across the arc. The meridional electric field inside the arc was altered slightly to meet this requirement, and with no westward electric field the electrojet is entirely a Hall current. The Hall electrojet for the constant meridional current model is enhanced about 25% over the current for the surrounding regions. The maximum current density is 13.7 $\mu A/m^2$ (Figure 4.7)

and has a height integrated value of 0.43 A/m. Otherwise the electrojet is the same as in the first Hall current model. The Pedersen current in the meridian across the arc (bottom diagram, Figure 4.19) has a height-integrated current of about 0.16 A/m southward; this is consistent with the observations of Armstrong and Zmuda (1970) (see Figure 4.21). The intense field-aligned current on the equatorial side of their model current system can be accounted for by either decreasing the electric field or the conductivity by a factor of about 2 in a distance of 20 km. Thus the model of a Hall electrojet driven by a southward electric field with a constant southward meridional current seems to best fit the observations compared to the other models proposed in this chapter, although only detailed observations can resolve the possible models.

A Hall electrojet driven by an electric field 5 times that of the above model was constructed to model current flow during moderate geomagnetic storms. The same arc model was used but the electric field outside the arc was 100 mV/m and decreased to 24 mV/m inside the arc. The total electrojet current is ~0.5 MA for the two arcs and adjacent regions. The maximum rate of Joule heating was ~0.5 $\mu J/m^3 s$ (section 4.6) while the maximum magnetic field perturbation at the earth's surface was -420 nT.

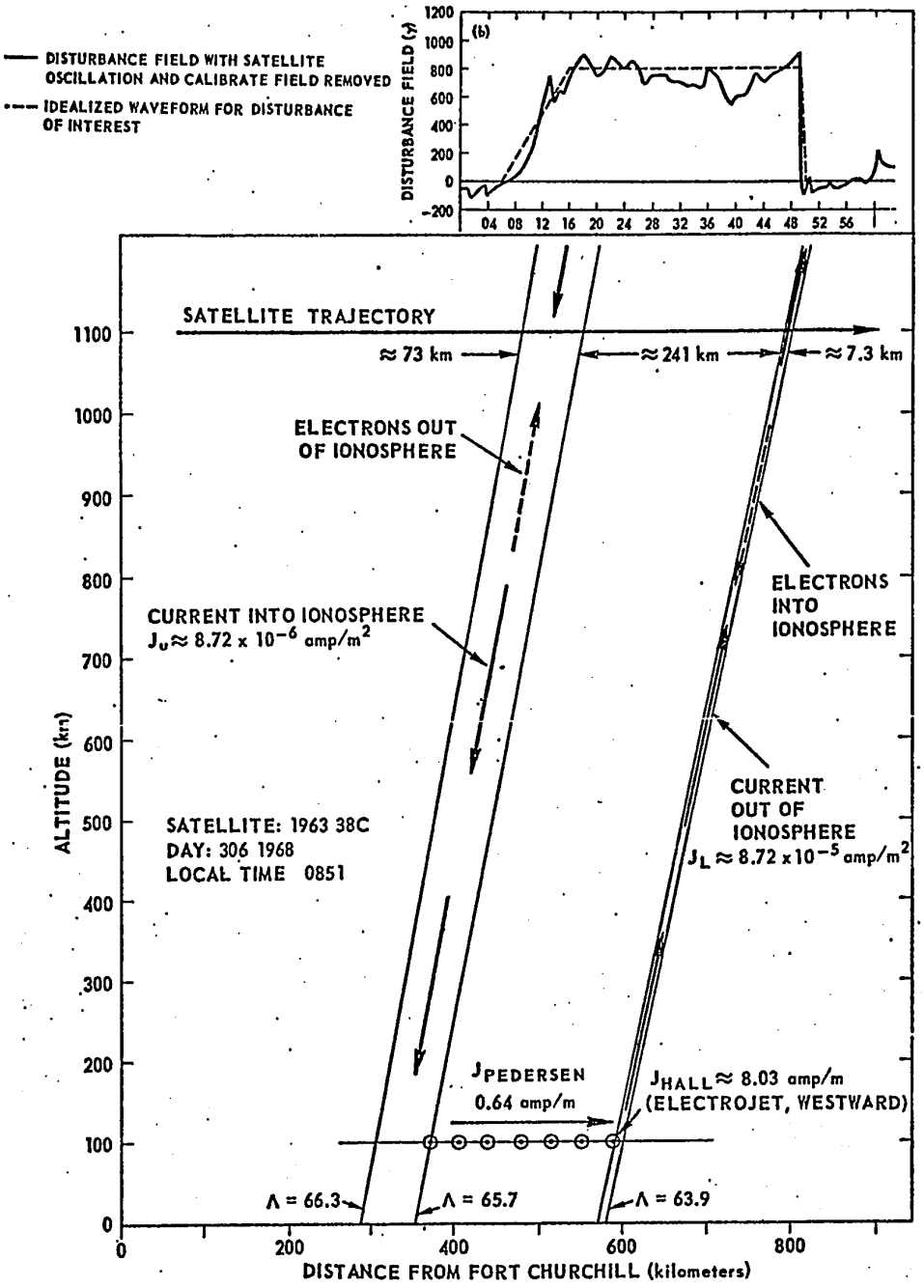

Figure 4.21 The observed transverse magnetic disturbance detected by satellite (top) and model of the currents system (bottom); after Armstrong and Zmuda (1970).

4.5 Maximum and Minimum Electrojets

The rotation of the electric field relative to the arcs and the auroral zone will change the magnitude of the electrojet non-linearly. For example, maximum current will flow in the auroral channel when the vector sum of the Pedersen and Hall currents are in the direction of the channel. The same electric field used for the Pedersen sheet current model was used for the maximum and minimum electrojet models; thus the magnitude of the different currents can be compared. The angle of rotation of the horizontal electric field vector to produce the maximum westward current is determined from the tangent of the integrated Pedersen and Hall conductivity. The current ratio varies slightly for the different ionosphere profiles but an average value of 12° is adequate for the angle of rotation. The southward electric field must then be reoriented 12° to the west of south to produce the maximum auroral electrojet (shown in the first 150 km, Figure 4.22). The components of the electric field and integrated current as a function of the distance across the arc are shown in the first half of Figure 4.23. This westward electrojet is 8% more intense than the Hall current electrojet in section 4.4; the two models have electric fields of the same magnitude.

The minimum westward electrojet occurs when the westward component of either the Pedersenor Hall current cancels the eastward current of the opposite component. Exact cancellation of these currents requires slight changes in the direction of the electric field across the arc. The east-west current is minimized when the

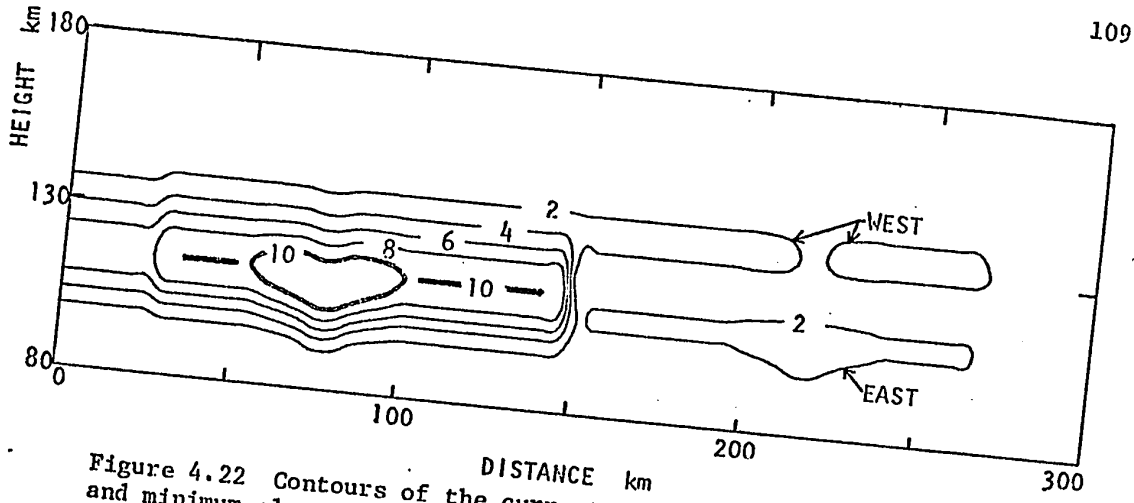

Figure 4.22 Contours of the current density for maximum and minimum electrojets due to rotation of the electric field.

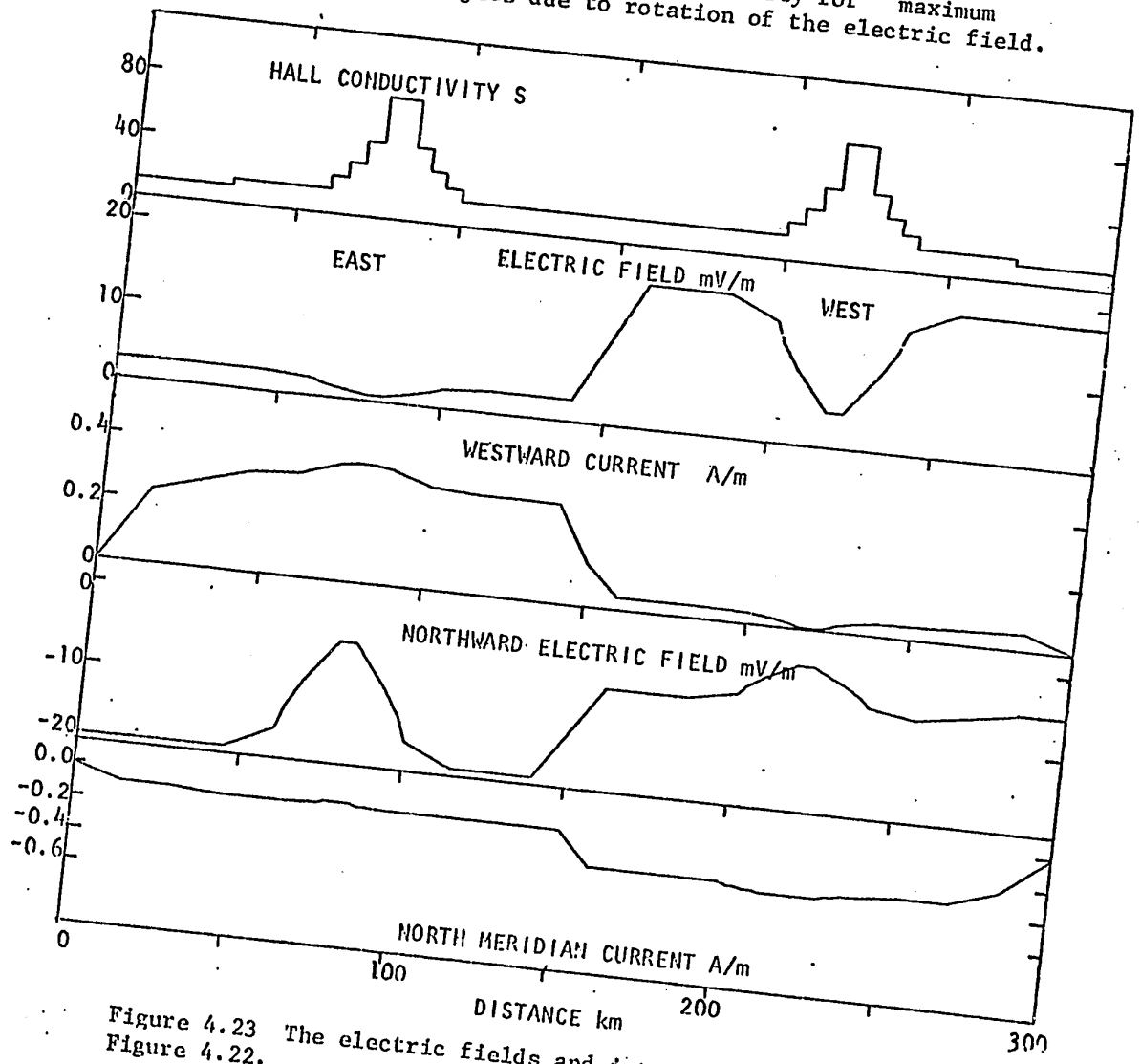

Figure 4.23 The electric fields and integrated currents for Figure 4.22.

electric field is in either of two directions. The relative magnitude of the Pedersen and Hall currents in the ionosphere depends on the height conductivity profile and occurs for this model when the electric field is 68° west of north and 68° east of south. The currents in the meridional plane are assumed to flow along the field lines upon reaching the edge of the auroral ionosphere. The contours of the electrojet current which result from the variations in conductivity for the different ionosphere models are shown in the 150 to 300 km section of Figure 4.22. The electric field variation and integrated currents for this model are also shown in the 150 to 300 km section of Figure 4.23. An interesting feature of Figure 4.22 is the approximately equal components of the Hall (110 km eastward) and Pedersen currents (130 km westward), flowing in opposite directions, and respectively increasing and decreasing inside the arc. Large field-aligned currents flow downward on the north side of the arc in the second model, upward on the southern side, and upward between the arcs. Antiparallel currents flow in the arc of the first model.

4.6 Heating and Winds from Currents

Joule heating of the ionosphere can be calculated from equation 3.61 which describes the scalar product of the current with the electric field. The contours shown in Figure 4.24 are of the Joule heating for the Hall electrojet, meridional and field-aligned currents in Figure 4.17 and 4.18. The maximum heating occurs outside the arcs as predicted by Cole (1971). The maximum heating rate for the substorm is 80 nJ/m^3s at 125 km or a column heating rate of 50 mJ/m^2s;

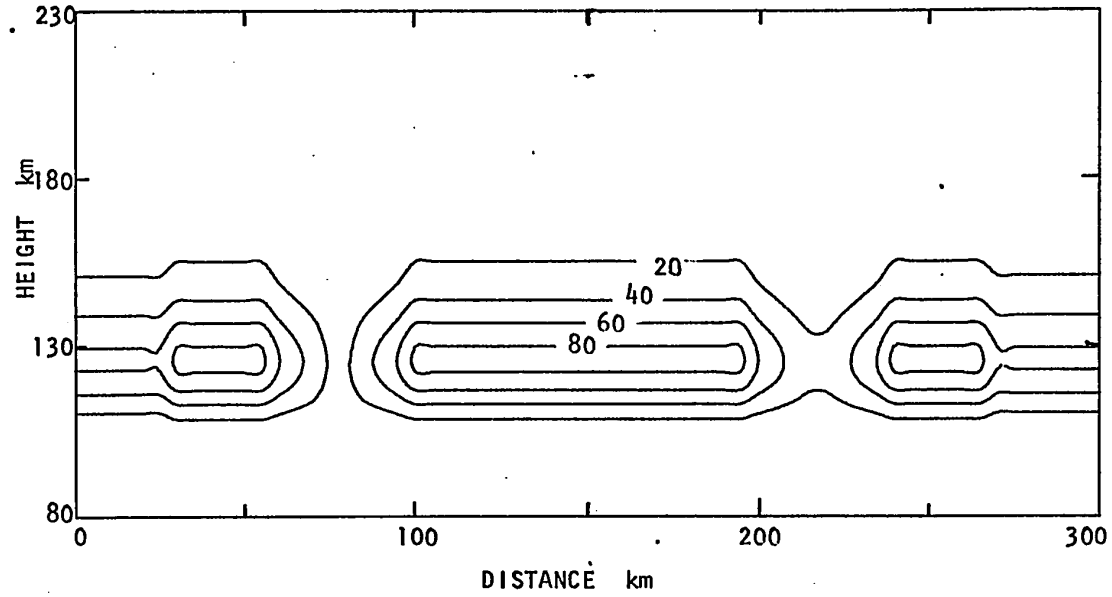

Figure 4.24 Contours of joule heating (nJ/m^3s) caused by the currents for the Hall electrojet in Figures 4.17 - 4.19.

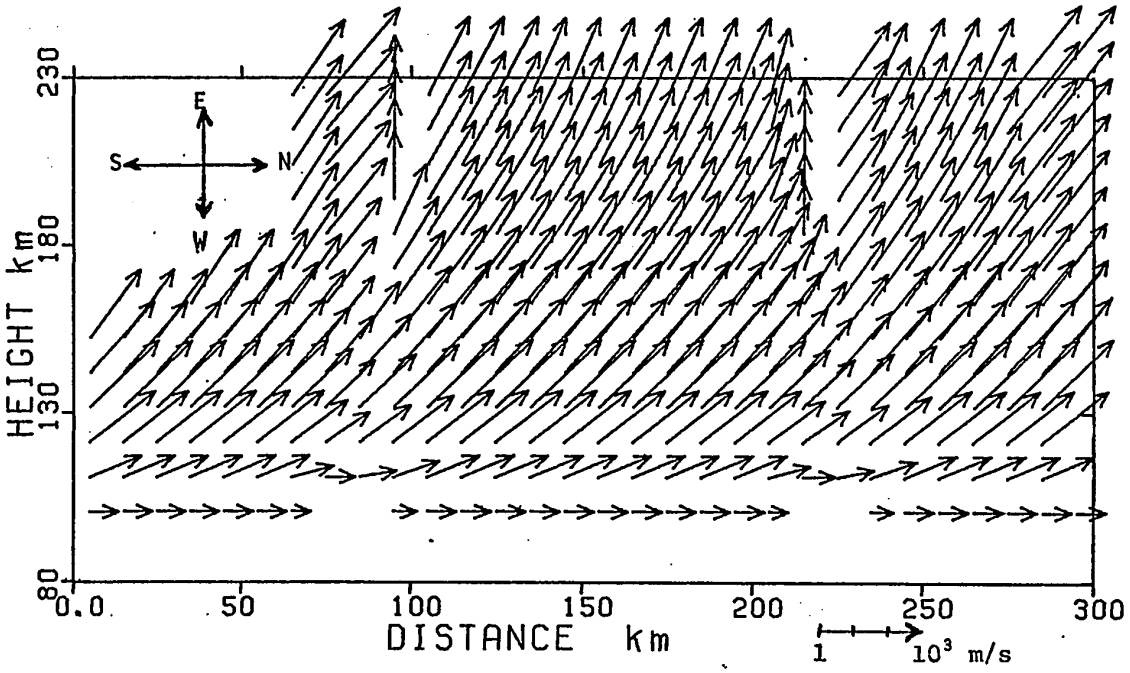

Figure 4.25 Horizontal winds resulting from electric fields for the Hall electrojets in Figures 4.17 - 4.19.

this is the same figure obtained by Cole (1971) for heating in the day time E-region assuming a 100 mV/m electric field normal to the ambient magnetic field. For auroral conditions he estimates heating rates a factor of 10 to 100 more than the above during major geomagnetic storms which is comparable with the 0.5 $\mu J/m^3 s$ obtained for the storm in section 4.4. The heating rate for storms is capable of causing significant changes in the meteorology and aeronomy of the upper atmosphere (Cole, 1971).

The electric fields in the auroral ionosphere will cause neutral winds in the F region by means of ion drag forces. These winds will redistribute the ionization in the F region (possibly causing the "troughs" observed by the Isis and Alouette satellite topside ionospheric sounders) and also will alter thermospheric motions through the process of momentum transfer. The neutral winds were calculated by expression 3.57 for the two Hall current models (shown in Figures 4.17 and 4.18) and are represented in Figure 4.25 by arrows with the east-west component rotated to the vertical for plotting. The logarithm is taken before plotting to encompass the dynamic range and direction of the winds. The winds in the lower E-region (100 km) are northward at about 10 m/s increasing to ~100 m/s at 125 km. At altitudes of 140 km the winds are northeastward at ~200 m/s but rotate to the east at 200 km reaching velocities of 200-500 m/s. The winds are ~50 m/s and to the east at 150 km, immediately above the arcs.

CHAPTER 5

AURORAL CURRENTS

5.1 Observations and Ionosphere Model

The dynamics of the electrojet and the limitations of magnetic analysis account for the ambiguity of the current system for polar magnetic substorms deduced from magnetograms. There are two possible paths for the return current of the electrojet: one is through the ionospheres in the polar cap and midlatitude regions, and a second is along magnetic field lines to the magnetosphere. These paths are difficult to resolve using solely magnetic field observations because of the similar magnetic variation patterns caused by the current flowing in the two circuits. The magnitude and location of the field-aligned currents are not known, nor is the cause of these currents. Another unknown is the contribution of auroral arcs to the enhancement of the electrojet and field-aligned currents. The driving mechanism of the auroral electrojet and the resultant field-aligned currents is central to the understanding of the dynamics of the auroral ionosphere and polar magnetic substorms as well as their relationship to the magnetosphere. Combining the information on electric fields, electron densities, and magnetic fields obtained simultaneously along a meridional profile can provide some of the answers as well as independent checks. The spatial distribution of ionization could not be determined for the August 3, 1969 substorm, however the electric and magnetic fields were measured at a few locations along the meridian. The direction of the currents, the relative contributions to the current by different electric fields,

and ionosphere models can be compared using the two independent methods. The development of a substorm and the undulations during its lifetime could be functions of variations in the ionosphere or in the direction and magnitude of the electric field.

Shown in Figure 5.1 are the locations of the electric and magnetic field observation points for the joint project of Drs. F.S. Mozer and G. Rostoker. Electric field measurements were obtained from 4 balloon-borne probes at each of the 6 sites for a maximum of 24 hours for each flight. During the 2-week experiment the magnetic field was monitored continuously by fluxgate magnetometers (Serson, 1957) and recorded in digital form on magnetic tape at each site.

The three electric field components were sampled at 1/2 second intervals. Later the data was despun from the rotating balloon and oriented into geomagnetic coordinates. The theory and validity of magnetospheric electric field measurements by balloon-borne probes is discussed by Mozer and Serlin (1969), Mozer and Manka (1971), and Mozer (1971). The electric fields were mapped through the ionosphere from D region heights of 75-80 km using expressions 2.69 and 2.70. Figures 5.2a and b show the electric field variations to be continuously turbulent and seemingly independent of the magnetic field fluctuations.

The three orthogonal components of the magnetic field were digitized at 1 second intervals and recorded in a nonstandard form on computer magnetic tape. Nonstandard digital recording was used to provide a second parity and magnetic component identification check.

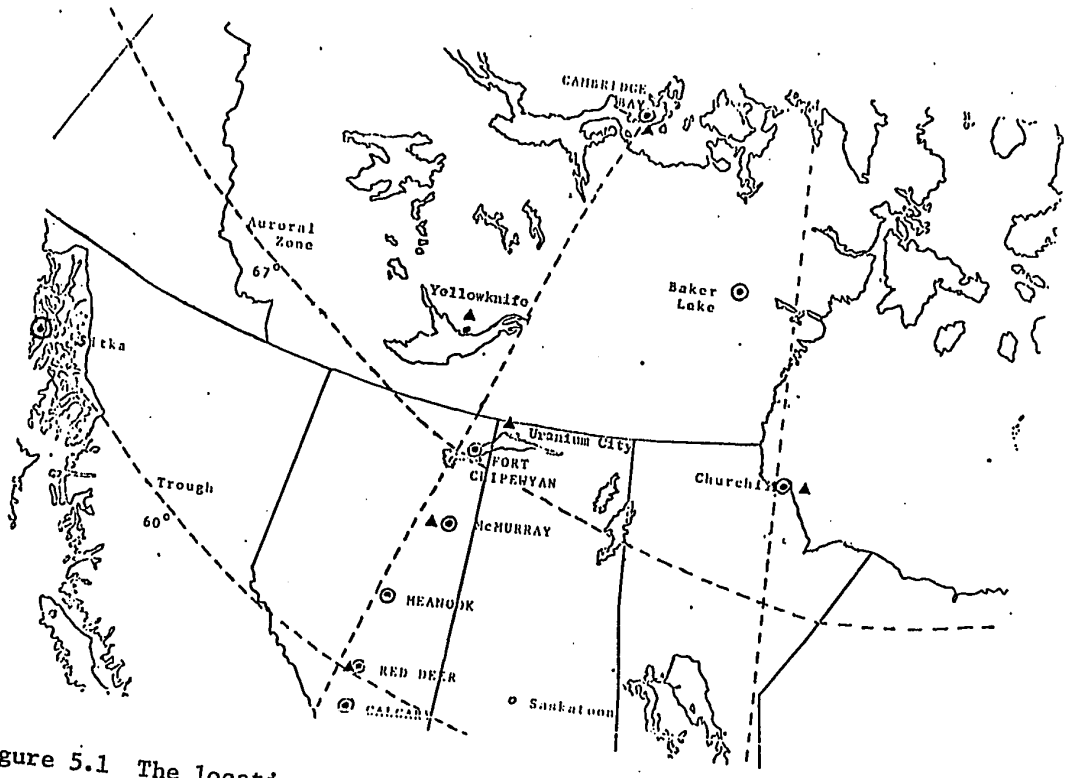

Figure 5.1 The locations of magnetic variation stations, ⊙, and balloon, ▲, borne electric field probes along a meridian across the auroral zone.

Before digitization, the analogue signals were filtered to prevent aliasing during the recording (Samson, 1971). The magnetometers have a noise level of less than 1 nT and the fluxgate detectors were buried to reduce their thermal drifts. The time from a WWVB receiver was recorded directly onto the magnetic tape in a digital form every 16 hours. Later, the time signal was decoded by a specially developed computer subroutine when the magnetic tapes were being decoded (due to the nonstandard recording) and edited before storing the data in a normal computer format. Except when power failures occur the time was generally accurate to within ± 0.1 seconds. The WWVB radio signal is not affected by magnetic storms or auroral displays so it could be received most of the time.

The magnetometers and balloon launch sites were located along a meridian (302°E) in the corrected geomagnetic coordinate system. Such an array facilitates cross-sectional studies and also development of polar magnetic substorms and the aurora. The model current system incorporating the observed electric field can be compared directly with the current system from magnetic field analysis for the same cross-section.

The magnetic field variations shown in Figure 5.2b for August 3, 1969 indicates an abrupt substorm commencement at 0900 UT with the magnetic field subsequently decreasing to -200 nT at Ft. Chipewyan in the H (magnetic north) component. During the substorms the variations at Cambridge Bay and Meanook were generally less than -20 nT. Electric and magnetic field observations at Churchill and the magnetic

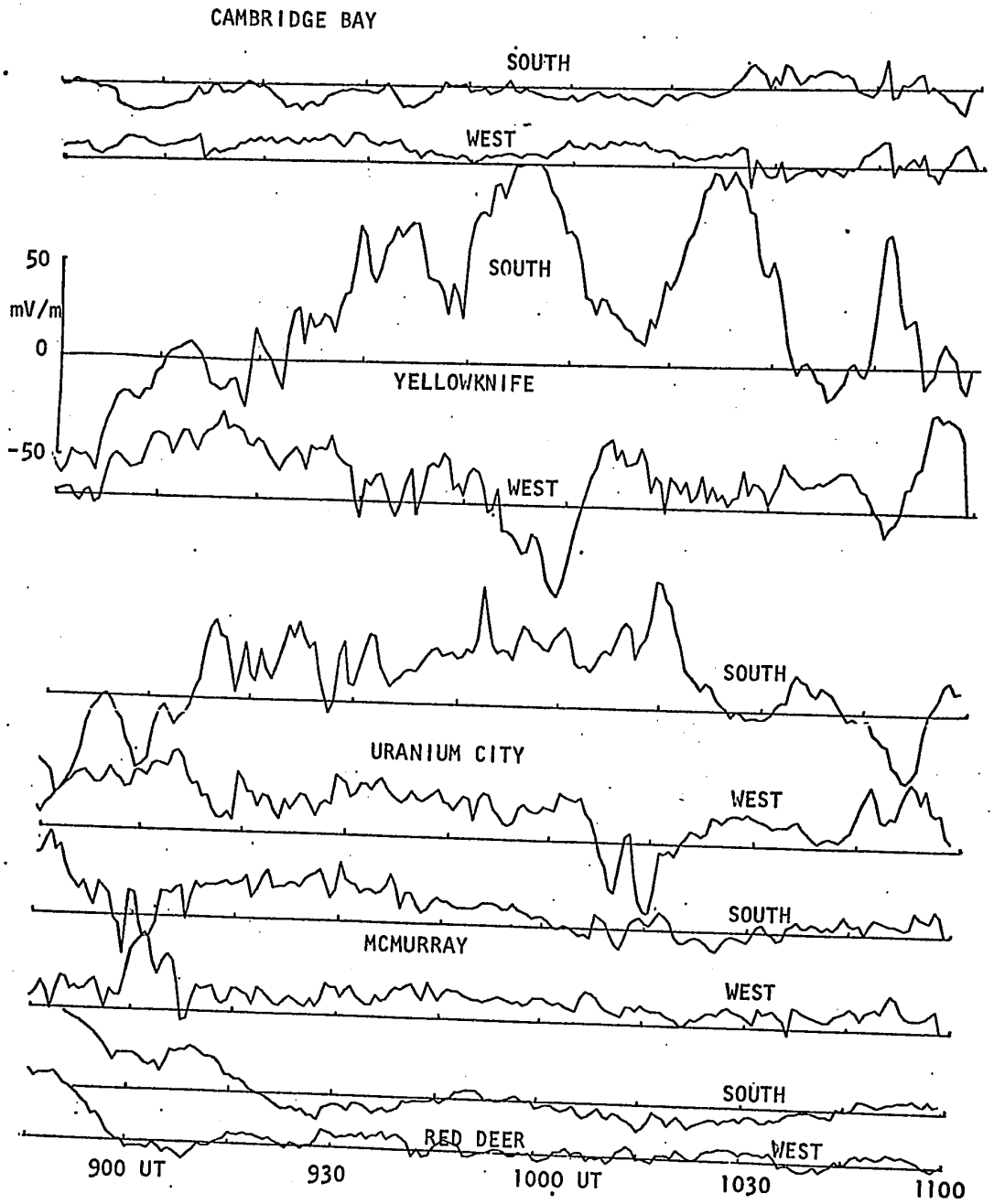

Figure 5.2a The time variation of the ionospheric horizontal electric field components as measured by balloon-borne probes at stations along a meridian across the auroral zone.

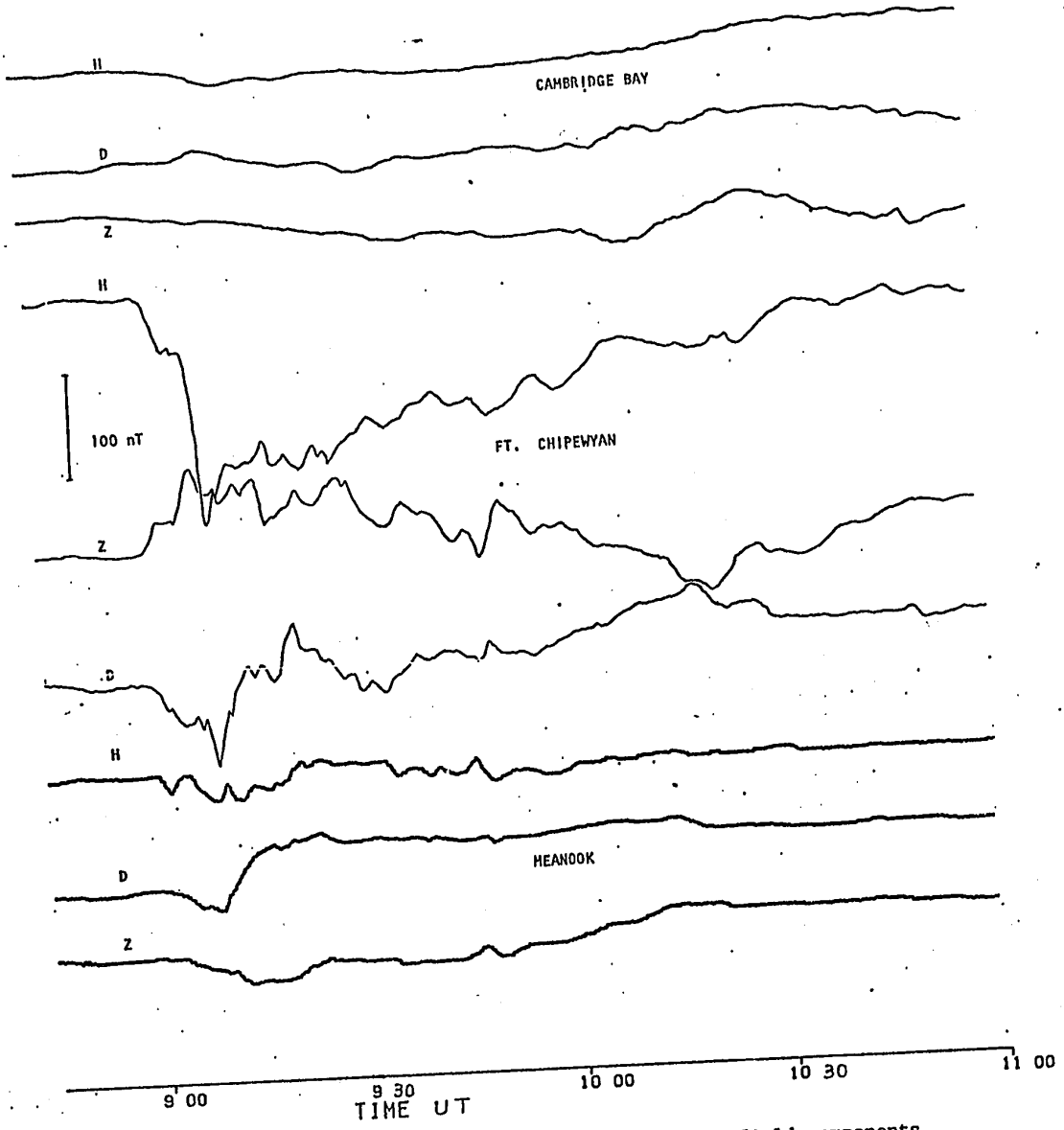

Figure 5.2b The time variation of the geomagnetic field components at stations along a meridian across the auroral zone. H is magnetic north, D is magnetic east and Z is vertical.

observatory data at Baker Lake were also used to aid in understanding the spatial and temporal development of the substorm. The electric field variations in Figure 5.2a appear to have no relation to the substorm in Figure 5.2b. For example, the large enhancement in the electric field at Yellowknife at 1000UT would drive an electrojet current 4 times that which would occur at 0945 UT; however, magnetic field variations at Ft. Chipewyan indicate the current is less at 1000 UT. At 0900UT the commencement of the substorm is also not correlated with any sudden change in the electric field occurring at any of the observation sites. However, the electric field does change direction from northwest, the direction for producing a minimum electrojet, to southwest, the condition for a large Hall and Pedersen driven westward current. The varying magnitude and direction of the electric field when combined with a dynamic ionosphere can produce a complex system of east and west electrojets, and field-aligned currents.

The conductivity for the ionosphere-electric field models of the electrojet were constructed from atmospheres and ionospheres which probably occurred during the substorm. For the calculation of collision frequencies used in the conductivity expressions, the model atmosphere was a summer model for 60° latitude using a solar flux value of 188 and the planetary magnetic index Ap, of 14. The method of calculating the atmosphere from temperature and mean molecular weight height profiles is discussed in sections 2.3 and 2.4. Table 1 lists the input parameters for the model atmosphere and some of the calculated quantities. The atmosphere model is probably a close approximation

to the actual conditions. Visual observations were used to model the ionosphere but the same twin arc structure was also retained for comparison with the previous theoretical models and for comparison of the electrojets. The ionosphere profiles were calculated from expression 2.62 and then combined to form appropriate model cross sections of the auroral zone ionosphere. To make the resultant east-west current similar to the current obtained from magnetic field analysis the models of the arcs and the regions adjacent to the arcs were varied in size and brightness. The integrated meridional and electrojet currents flowing in the arcs were assumed to have the same current density as the currents in the region adjacent to the arc. The model combines the features of the Pedersen sheet current model in section 4.3 and the Hall current model in section 4.4 and is a reasonable estimate of the conditions inside the arc. These currents are then independentof the arc's brightness but are now dependent on the currents in the region adjacent to the arc. The nondiscrete auroral regions surrounding arcs possibly extend for several hundred kilometers and probably coincide with the less turbulent electric field observations which the balloon-borne detectors effectively measure. The electric field components inside the arc were calculated from the following expressions,

$$E_x = \frac{\Sigma_p J_x - \Sigma_H J_y}{\Sigma_p^2 + \Sigma_H^2} \qquad (5.1)$$

$$E_y = \frac{\Sigma_H J_x + \Sigma_p J_y}{\Sigma_p^2 + \Sigma_H^2} \qquad (5.2)$$

where Σ_p and Σ_H are the integrated Pedersen and Hall conductivities inside the arc, and J_x and J_y are the integrated currents adjacent to the arc.

5.2 Auroral Currents During a Substorm

The polar magnetic substorm on August 3, 1969 is modelled by constructing appropriate ionosphere cross-sections having a conductivity distribution such that the observed electric field will produce a current equal to that inferred from magnetic field analysis. Profiles were constructed at 7.5 minute intervals during the 1 hour substorm period. The first latitude profile at 0900 UT immediately precedes the sudden commencement of the polar magnetic substorm and shows the observed electric field configuration producing a minimum east-west current. The current model is similar to the minimum electrojet model in section 4.5, having a large meridional current flow through the two bright arcs. As in section 4.1, the ionosphere model consists of the same 50 kR arcs but the adjacent regions are 1 kR instead of the previous 2 kR; otherwise all the dimensions and parameters are the same. The arcs are assumed to be at 70° initially, then moving southward to about 67° before the substorm. Shown in Figure 5.3 are the integrated Pedersen and Hall conductivities and the electric field components used to model the current system. The maximum electric fields correspond to the observations by the Yellowknife probe and

and the minimum fields inside the arcs have been calculated from expressions 5.1 and 5.2. The other observed electric fields along the meridian are shown in Figure 5.5. The westward electric field outside the arcs was assumed constant across the section at 20 mV/m but the northward component decreases from 9 mV/m on the equatorial side of the arcs to 6 mV/m on the polar side of the arcs.

The resultant electrojet has an integrated westward current of 25 mA/m in the southern arc and 55 mA/m in the northern arc (Figure 5.3). In Figure 5.4 the current density contours in the cross-section show a small eastward electrojet ($1\mu A/m^2$) flowing below 110 km while the westward electrojet ($2\mu A/m^2$) is at 130 km. The eastward electrojet is approximately 20% of the 10.6 kA westward electrojet. In Figure 5.3 the meridional current decreases only slightly from 0.27 A/m to 0.25 A/m with increasing distance across the arc. The meridional current is 10 times that of the electrojet and flows down the magnetic field lines on the equatorial side of the arcs, northward through the ionosphere and up the magnetic field lines on the polar side of the arcs (Figure 5.5). The current density determined from magnetic field analysis (section 3.2) is also shown in Figure 5.3. The current distribution has been calculated from observations of the magnetic field variations along the meridian and has been corrected for induction using an identical current mirrored at a depth of approximately 315km.

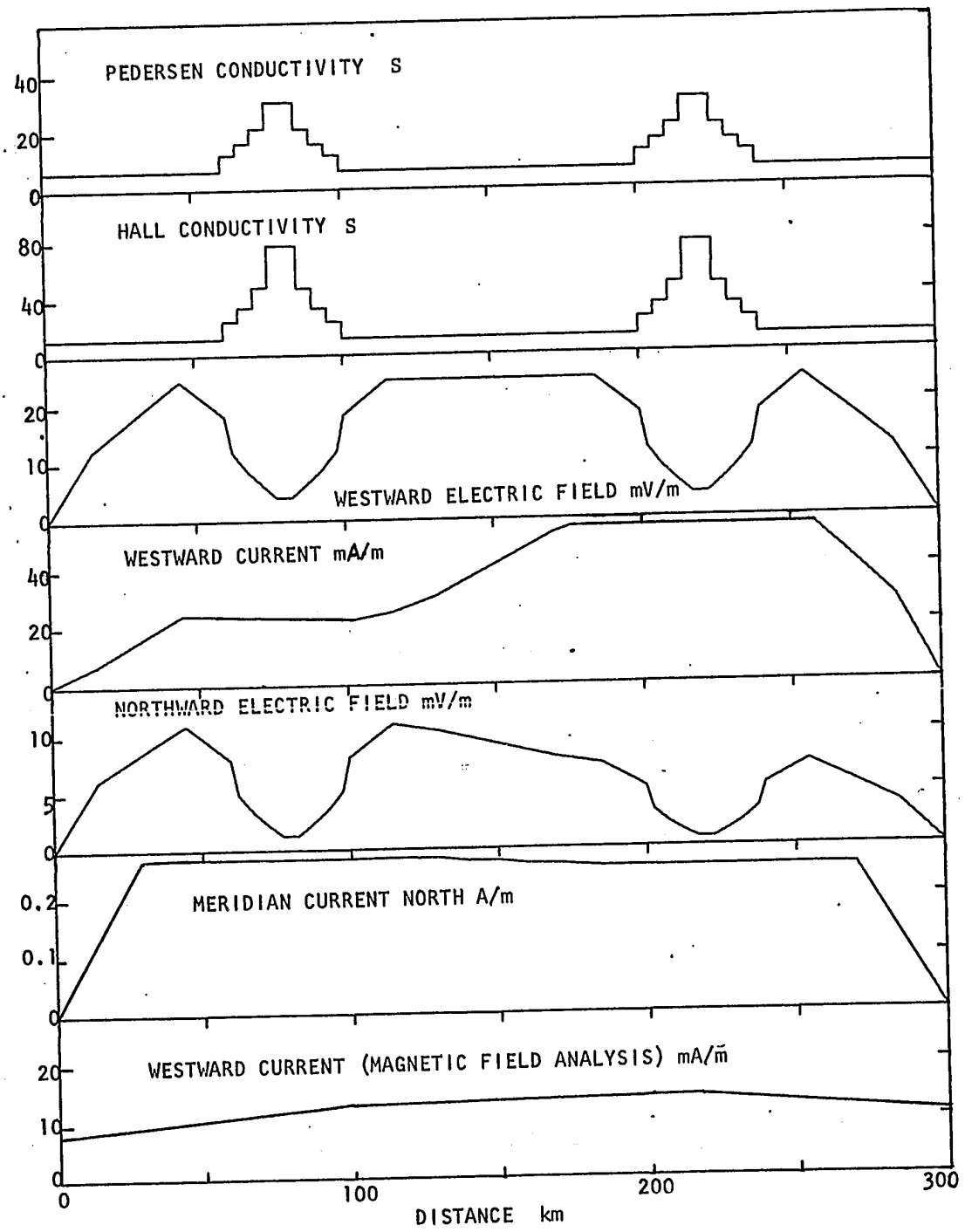

Figure 5.3 Variations of the conductivity and electric field and the resultant currents as a function of the distance across a meridian section of the auroral zone. The current deduced from magnetic field analysis after corrections for currents induced in the earth is shown in the lower diagram. The models are presubstorm at 0900 UT August 3, 1969.

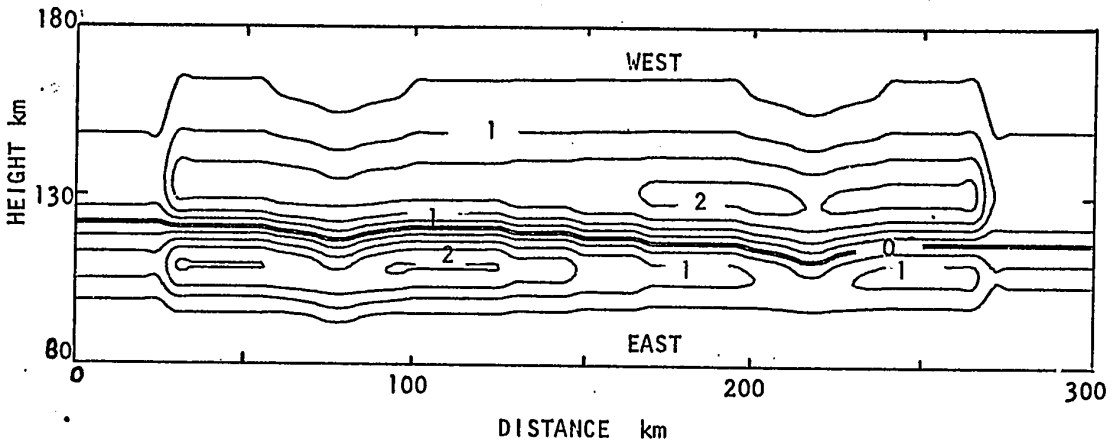

Figure 5.4 Contours of the electrojet current density ($\mu A/m^2$) in the meridian plane for the presubstorm model (Figure 5.3). The westward electrojet above 125 km is larger than the eastward electrojet even though they both have peak current densities of $2\mu A/m^2$.

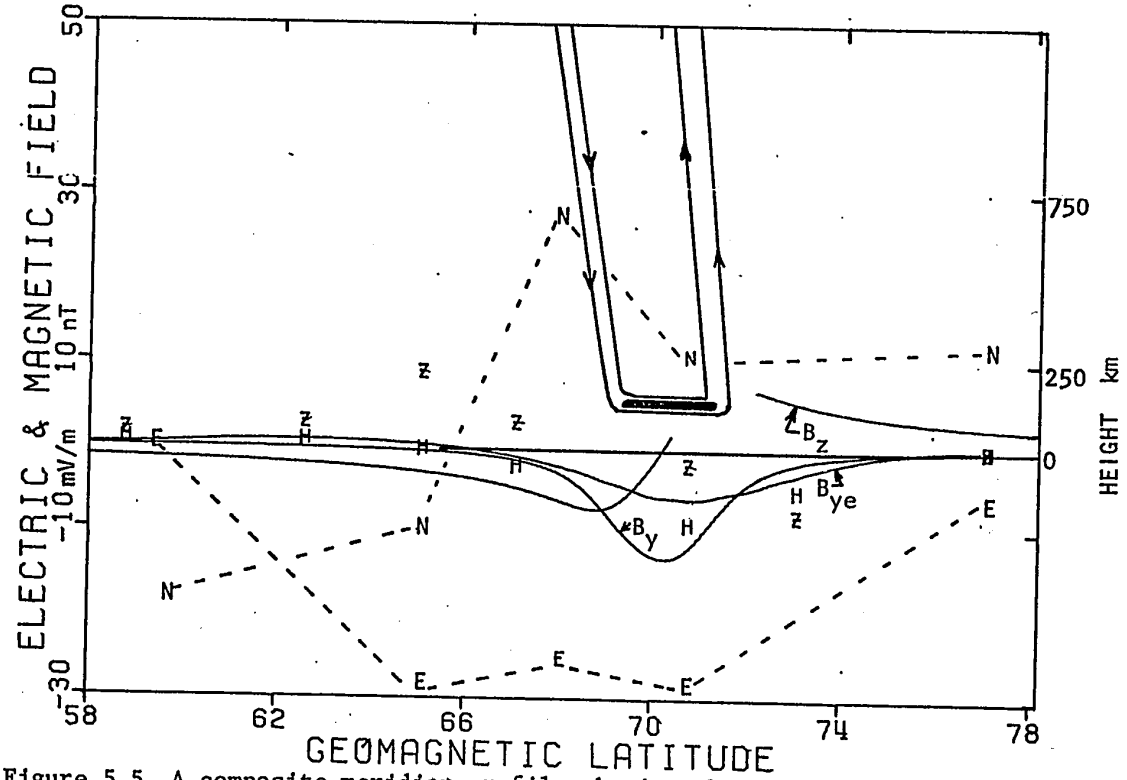

Figure 5.5 A composite meridian profile showing the variation in the northward (N) and eastward (E) electric fields, the observed horizontal (H) and vertical (Z) components of the magnetic field, and the horizontal component (B_{ye}) of the electrojet calculated from the observed magnetic fields with correction for induction. The horizontal (B_y) and vertical (B_z) components of the auroral model electrojet (shaded) are also shown together with the field-aligned current flow. H and Z at 71° and 73° are estimates.

In Figure 5.3 the current profile obtained from the magnetic field analysis is smoothed and distributed over a larger region because of the inherent resolution limitations in the analysis. Magnetic field analysis of ground based observations also cannot uniquely identify the short meridional currents connected to the antiparallel field-aligned sheet currents.

The composite diagram in Figure 5.5 shows the ionosphere electric field model of the current system as well as the magnetic field latitude profile and the eastward (E) and northward (N) profiles for the electric field components. The observed northward horizontal (H) and vertical (Z) components of the magnetic field variation are shown together with the horizontal (B_y) and vertical (B_z) components of the magnetic field of the ionosphere electric field current model and finally the latitude profile of the horizontal component (B_{ye}) of the ionosphere electrojet determined from magnetic field analysis. Direct comparison of the two magnetic field profiles (B_y, B_{ye}) can be made as they are calculated from the two independently obtained auroral electrojets. The poor comparison of B_y and B_{ye} in Figure 5.5 can readily be accounted for by the errors in baseline determinations in magnetic field analysis and the unknown spatial distribution of the electron density in the auroral ionosphere and of the electric field. Small changes in the direction of the electric field or in the electron density of the ionosphere model could produce an electrojet with a magnetic field, B_y, exactly the same as B_{ye}. The main feature of the ionosphere electric field model is the small electrojet even though two bright auroral arcs are present as well as a

typical auroral zone electric field. The low magnitude of the electrojet is due to the angle of the electric field with respect to the channel of auroral ionization, causing the Pedersen and Hall components of the current system to nearly cancel.

The meridional profile at 0907 UT corresponds to the polar magnetic substorm shortly after the onset of its expansive phase, during which the Ft. Chipewyan magnetometer recorded -200 nT. The ionosphere model for the section was similar to previous models which have the region surrounding the arcs corresponding to glows of 2 kR (Figure 5.6). At Yellowknife and Uranium City the westward electric field is 30 mV/m and the meridional component of the electric field is now southward and varies from 11 mV/m to 7 mV/m across the section (Figures 5.2a, 5.6). Constant meridional and electrojet currents inside the arcs are assumed and the unknown electric fields calculated from expressions 5.1 and 5.2. The current in the resultant electrojet was 107 kA producing a magnetic field of -128 nT, while the ionosphere current from magnetic field analysis had a magnetic field of -134 nT. For the two electrojets the corresponding current densities are 0.4 A/m and 0.35 A/m (Figure 5.6). For the ionosphere electric field model in Figure 5.7 the maximum current density is $10\mu A/m^2$. The electrojet is 280 km in width extending from 100 km to 150 km in height with the maximum current density at a height of 133 km. The field-aligned current flow is downward on the equatorial side of the arcs and also between the arcs; it subsequently flows northward through the ionosphere where the integrated current density is 0.35 A/m (Figure 5.6), and

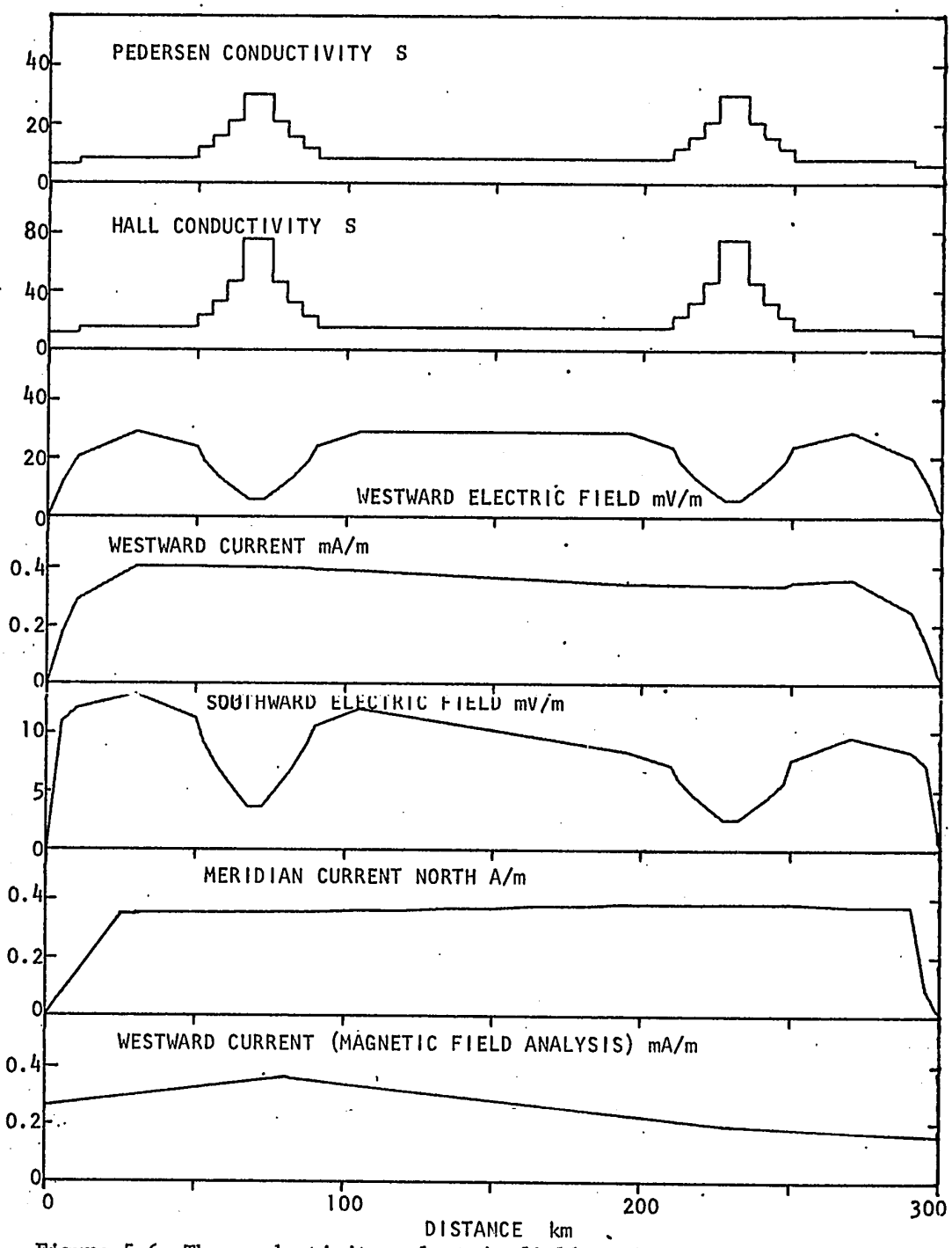

Figure 5.6 The conductivity, electric fields and resultant currents and the westward current deduced from magnetic field analysis as a function of the distance. The model is for the main phase of the substorm at 0907 UT.

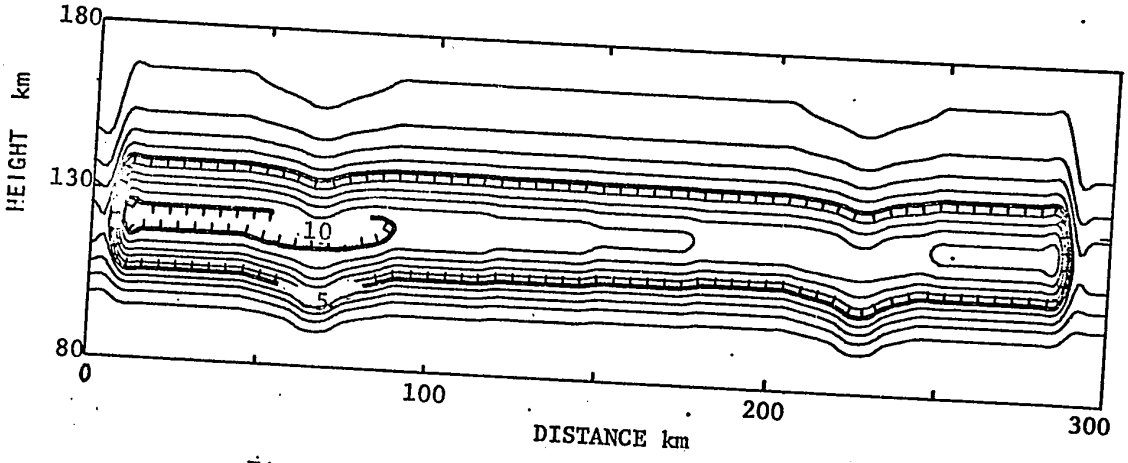

Figure 5.7 Contours of the current density ($\mu A/m^2$) for the model westward electrojet in Figure 5.6.

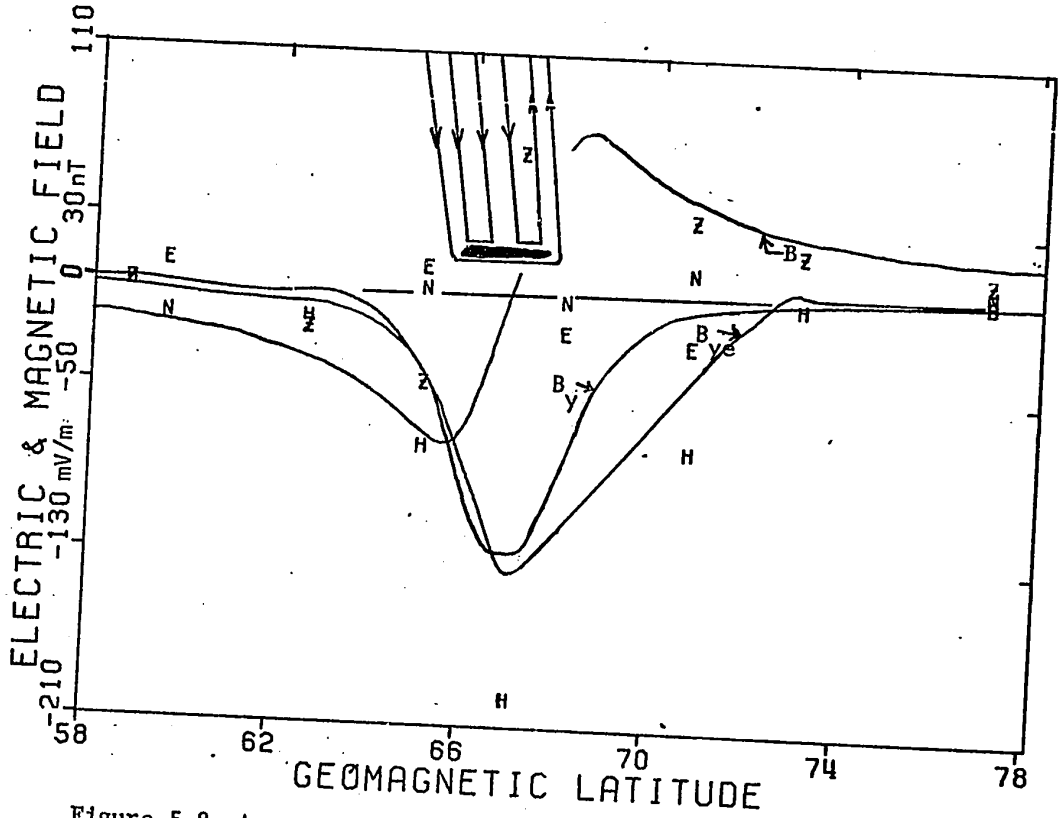

Figure 5.8 A composite meridian profile for the substorm models in Figures 5.6 and 5.7 with nomenclature the same as in Figure 5.5.

finally there is an intense upward current flow on the polar side of the arcs (Figure 5.8). The close similarities between the magnetic field profiles (Figure 5.8) of the ionosphere electric field model (B_y) and the magnetic field analysis model (B_{ye}) is fortuitous, considering the scant data for both models.

The magnitude of the H component of the polar magnetic substorm gradually decreases to ~ -50 nT by 1007 UT. The electric field remained fairly constant and is in the southwest direction at Uranium City but increases to ~100 mV/m southward at Yellowknife. The southward component of the electric field at McMurray decreased until at 1007 UT it was negligible (Figure 5.2a). The variation in the vertical (Z) component of the magnetometer at Ft. Chipewyan is small indicating the center of the electrojet is over the station. An example of the current system during the decay phase of the substorm is the cross-section at 0915 UT. The ionosphere for the section is the same as at 0907 UT (Figure 5.9), but the westward electric field is now 25 mV/m and the southward component decreases from 11 mV/m to 4 mV/m (Figure 5.9). The resultant westward electrojet current (Figure 5.9) was 91 kA with a maximum current density of 11$\mu A/m^2$ occurring at a height of 112 km. This current density decreased to 7$\mu A/m^2$ while increasing to an altitude of 125 km towards the poleward side of the cross-section. As shown in Figure 5.10, the meridional current in the ionosphere was 0.3 A/m northward, resulting from current flowing down the magnetic field lines on the equatorial side of the electrojet and upward on the poleward side.

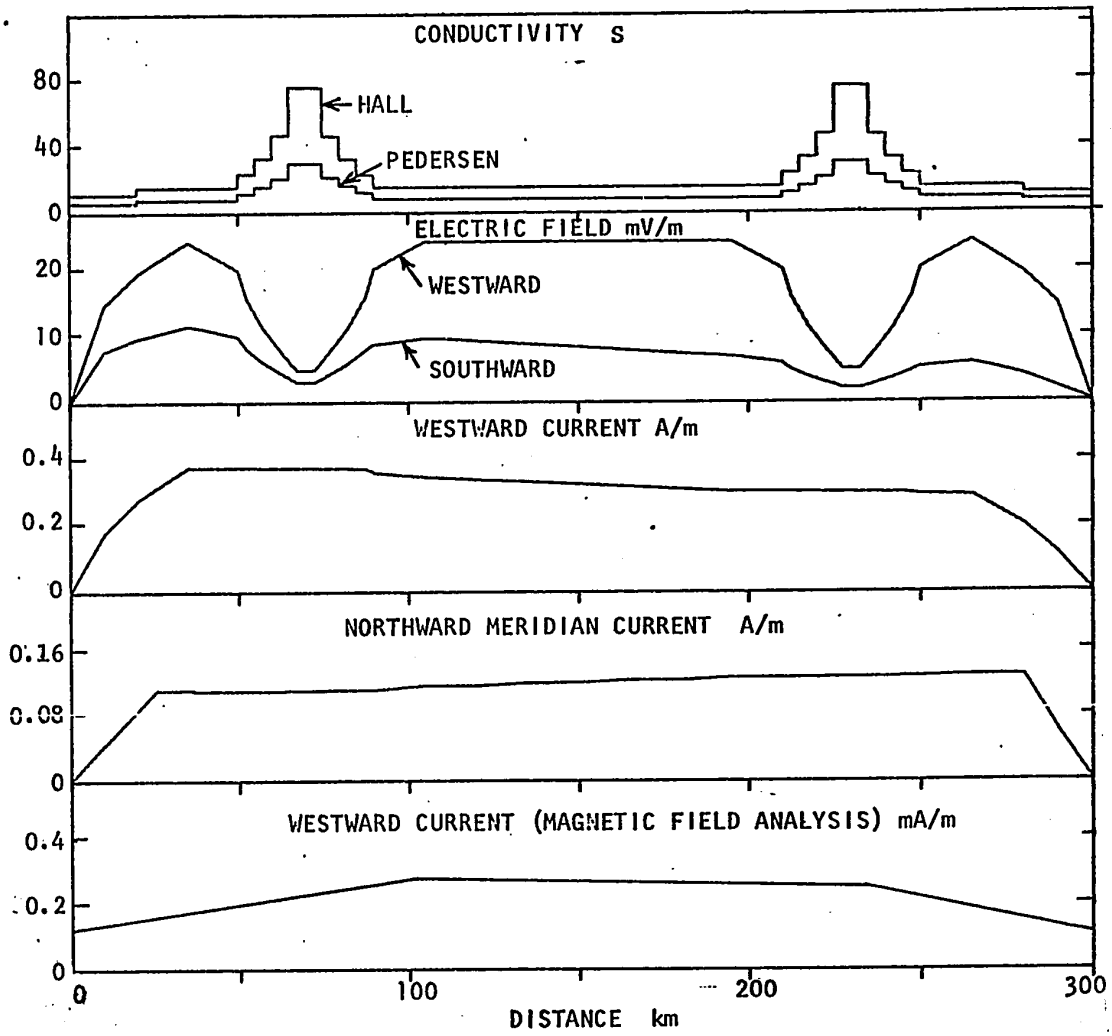

Figure 5.9 The variation of the conductivity, electric fields and currents at 0915 UT after the main phase of the substorm.

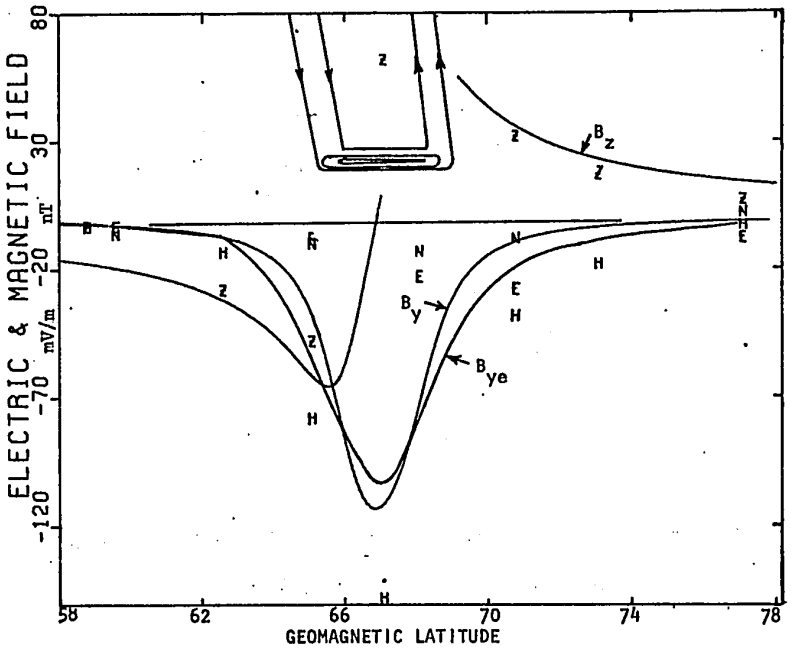

Figure 5.10 The variations of the electric and magnetic fields across the auroral zone for the electrojet of Figure 5.9 with nomenclature the same as for Figure 5.5.

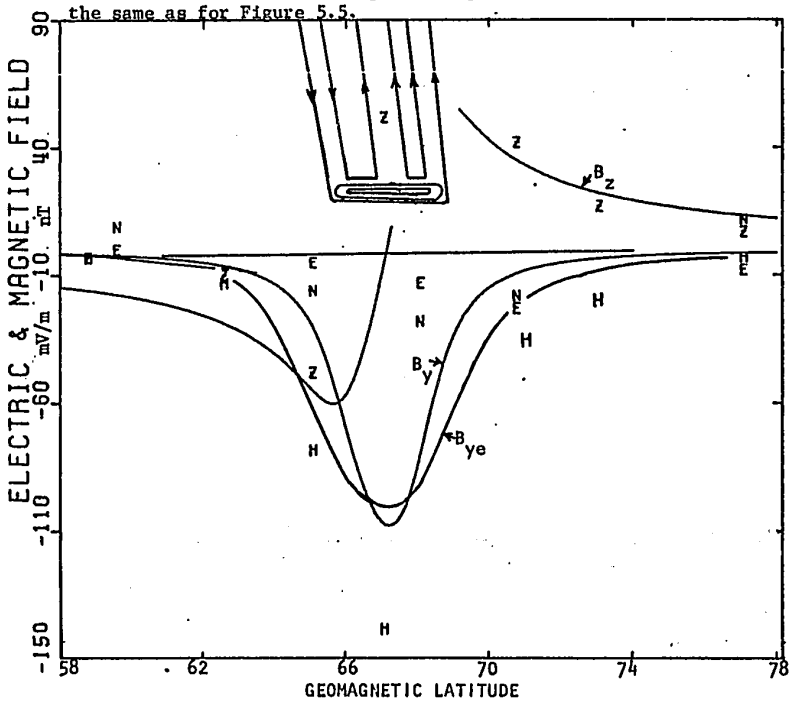

Figure 5.11 Latitude profile of the auroral parameters and resultant currents for the substorm at 0922 UT (Figure 5.12) having current flowing up the field lines between the arcs; nomenclature is the same as for Figure 5.5.

The magnetic field from the ionosphere electric field model (B_y) is -111 nT under the arcs. This is comparable to the magnetic field (B_{ye}) of -105 nT due to the ionosphere current (Figure 5.9) derived from analysis of the magnetic field variations across the auroral zone (Figure 5.10).

An example of a situation where current flows up the field lines between the arcs occurs at 0922 UT. Except that the auroral ionosphere is 20 km narrower than in the previous case, its cross-sectional structure is the same as that at 0915 UT (Figure 5.12). The westward electric field is 20 mV/m while the southward component increases across the section from 10 mV/m to 22 mV/m. The resultant westward electrojet current increases to 0.4 A/m at the northern edge of the current system where the meridional current decreased to 0.08 A/m. Figure 5.11 shows the meridional current circuit is completed by a downward field-aligned current on the equatorial side of the arc (resulting from a decrease in the ionization and the electric field), and in upward flowing current between the arcs (due to the increasing southward component of the electric field), and on the polar edge of the arcs (caused by an abrupt decrease in the ionization). The magnetic field produced by the ionosphere electric field current model is in agreement with the observed magnetic field analysis model (Figure 5.11).

The remaining sections from 0930 to 1007 UT are all similar in form with the strength of the electrojet gradually decreasing due to a decreasing conductivity associated with the weakening aurora. The large 100 mV/m southward electric field at Yellowknife during this

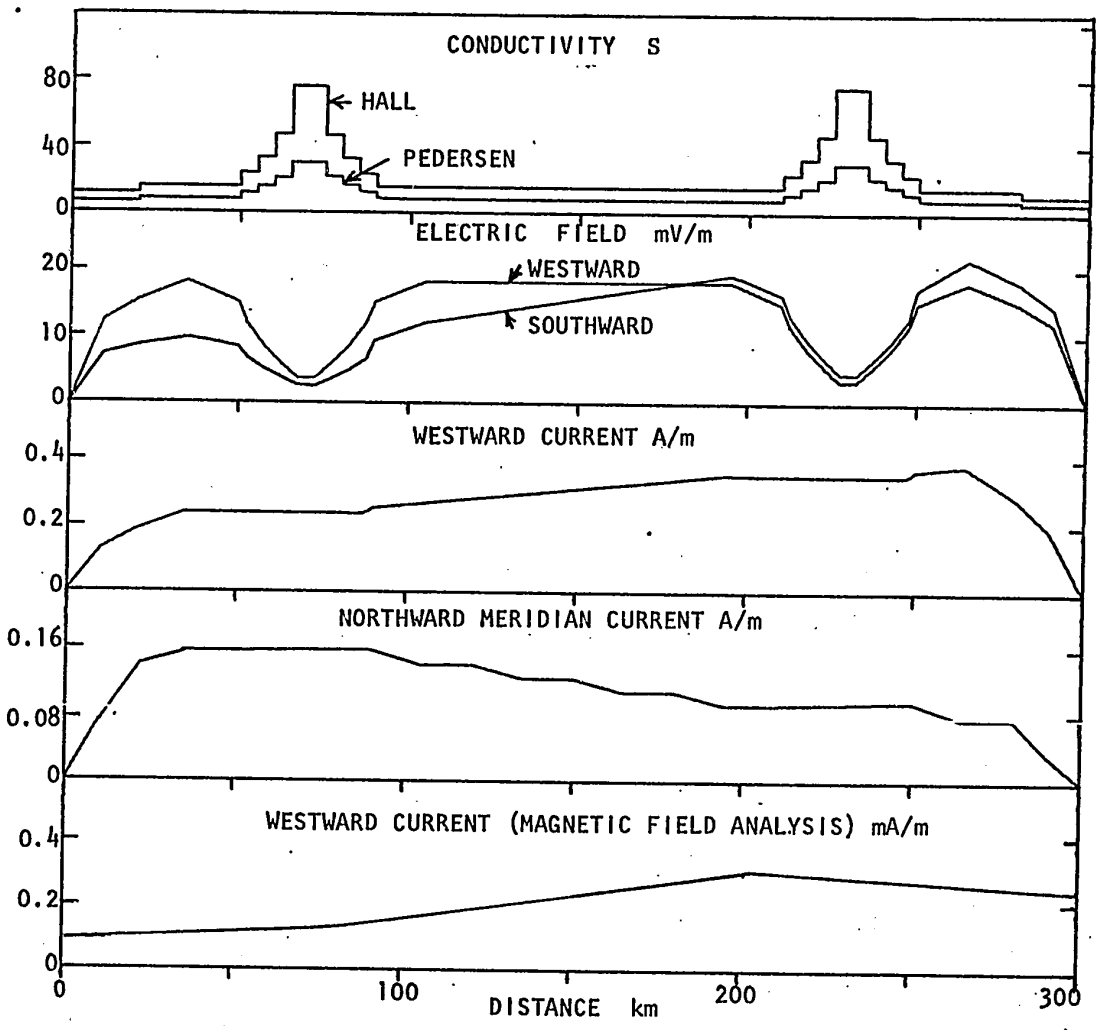

Figure 5.12 The variation of the conductivity, electric fields and currents at 0922 UT.

time, (which would drive a meridional current system consistent with that observed by Armstrong and Zmuda (1970)), is not effective because of the low ionization in that region. The ionosphere model required to fit the observed electric fields and magnetic fields consisted of two diffuse subvisual 2 kR arcs surrounded by a typical auroral zone night sky without aurora (see Figure 5.13). The electric field at 1007 UT is nearly the same as for the model at 0922 UT. The westward component is now 12 mV/m and the southward component increases from 18 to 29 mV/m towards the north. Inside the subvisual auroral glows, the electric field is calculated from expressions 5.1 and 5.2. A small eastward component of the electric field is required inside the second region of auroral glow to maintain constant meridional and electrojet current density across the section. The maximum westward current density is 0.1 A/m while the southward meridional current is 0.06 A/m. The field-aligned current (Figure 5.15) flowed down on the polar side of the arcs then returned to the magnetosphere in the region between the faint arcs. The total current in the electrojet (shown in Figure 5.14), is 26 kA which produces a magnetic field of -31 nT at the earth's surface comparing favourably with the -35 nT magnetic field from the electrojet as determined from the observed magnetic variations.

Magnetic field variations of the order of 50 nT are often present after a substorm and can be readily explained by the subvisual arc model and average auroral zone electric fields. Larger magnetic variations could be expected after storms and substorms

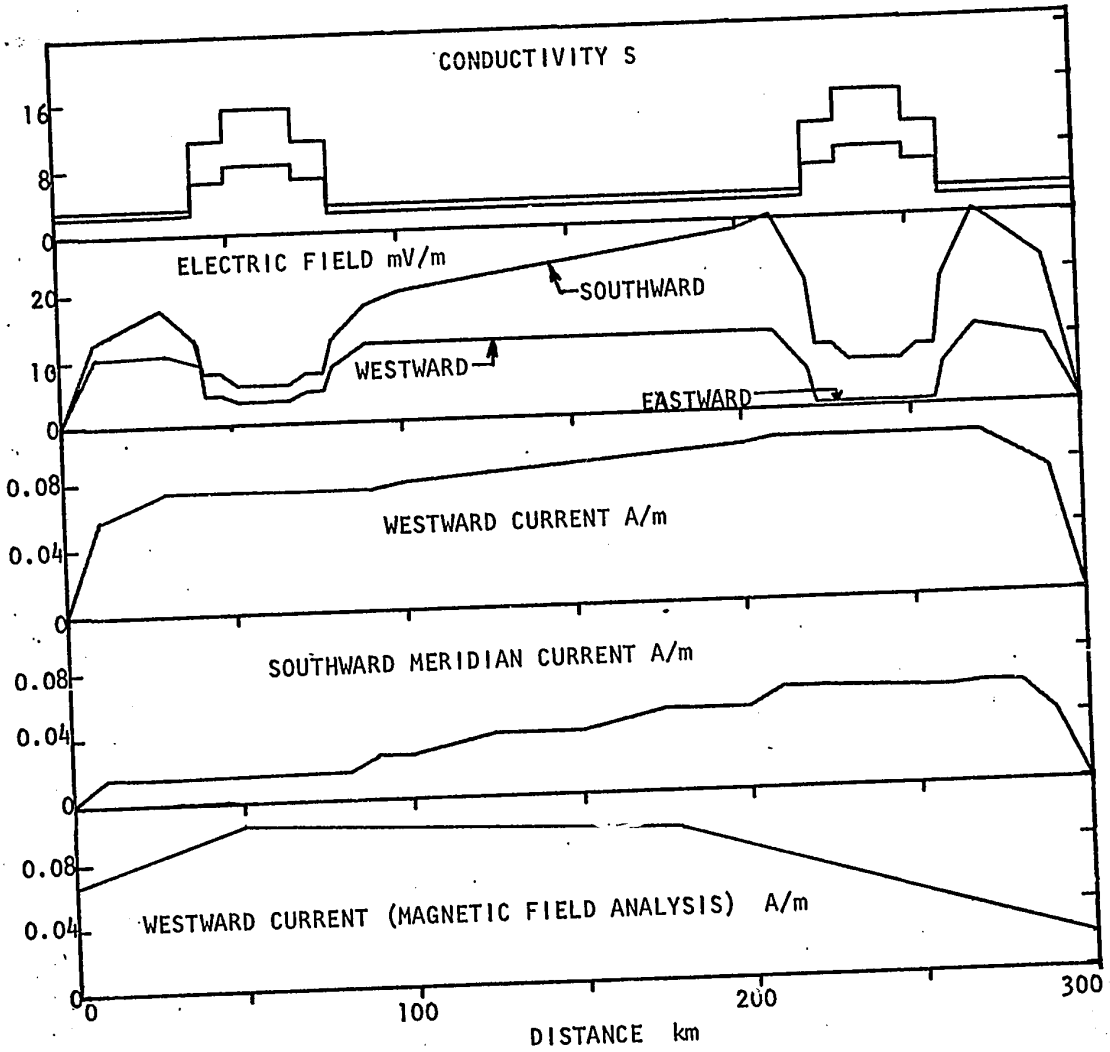

Figure 5.13 Variations of the conductivity across the auroral zone for a subvisual aurora at 1007 UT. The significant electric field, however, drives a substantial current.

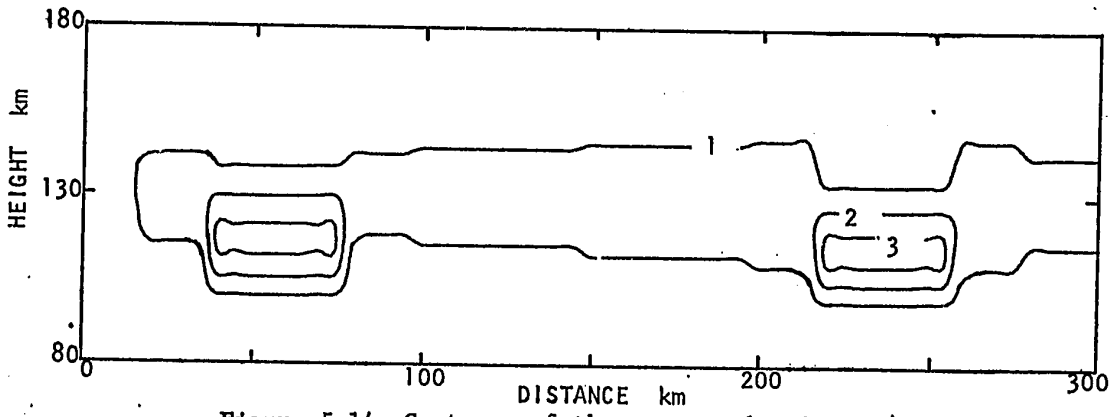

Figure 5.14 Contours of the current density μA/m for the post storm electrojet model in Figure 5.13.

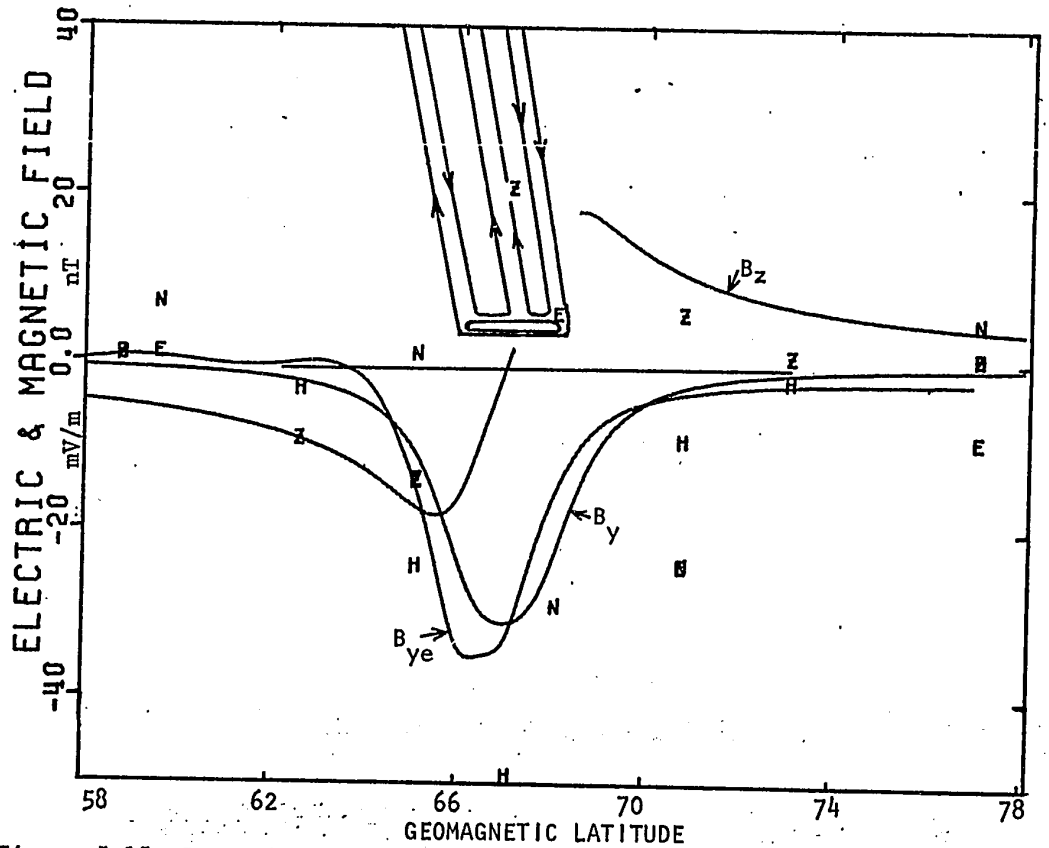

Figure 5.15 Composite meridian profile of the electric fields and magnetic fields of the electrojet models of Figure 5.13.

which have been accompanied by bright active aurora. Because of the larger latitudinal extent of magnetic storms, electrojets could flow in other than the east-west directions, producing significant fluctuations in both of the horizontal components of an observing magnetic station. Enhanced magnetic variations are also observed at dawn (Mayaud, 1967) and are probably due to the order of magnitude increase in the E layer ionization by solar radiation.

5.3 Field-aligned Currents

The return path of the auroral electrojet was postulated by Birkeland (1908, 1913) to follow the magnetic field lines into the magnetosphere. These currents have not been observed as yet, possibly because of their short duration of probably not more than ten minutes and possibly because of their small spatial distributions or ambiguity due to other currents. The magnetic declination variation patterns observed on the earth have been interpreted in terms of field-aligned currents (Bonnevier et al., 1970, Kisabeth and Rostoker, 1971), but can also be interpreted by ionospheric currents (Fukushima, 1969). The Birkeland currents can be determined from the ionosphere-electric field models by assuming divergence free conditions for the electrojet. Cross sections constructed at intervals during the substorm in the previous section can be assumed as typical samples of a westward travelling surge. Substorm current systems have a length of ~1000 km. Changes in the current flowing from one cross section to another must be completed by an equivalent current flow into the region between the cross sections. This current must flow along the field lines

because the conductivity and the electric field are too low for significant currents to flow in the midlatitude or polar ionospheres. The field-aligned current was computed using expression 3.17 over 5 km of the cross section from 80 to 230 km in height and 300 km across for each of the 10 sections.

The field-aligned current and the ionosphere electrojet were then integrated across the section at each height. The integrated currents for the longtitudinal section are shown in Figure 5.16 as arrows. The more intense current flows upward immediately after the commencement of the substorm until the peak of the expansive phase of the substorm. This interval of time is approximately 10 minutes and may correspond to a westward displacement of 100 - 200 km. Because the field-aligned current is distributed over this longtitudinal distance and also has latitudinal width of ~250 km, the area occupied by the 107 kA electrojet at 0907 UT is ~25 Mm^2 implying a field-aligned current density of ~5$\mu A/m^2$. The magnetic field of the distributed field-aligned current is ~130 nT at satellite heights. However, at the same time, field-aligned sheet currents occur on either side of the Birkeland current (Figure 5.17) and for a meridional current of 0.4 A/m (Figure 5.6) the magnetic field between the sheet currents is ~500 nT. The Birkeland current would thus contribute only a small magnetic field variation that would skew the rectangular shape of the magnetic field pattern between the sheet currents.

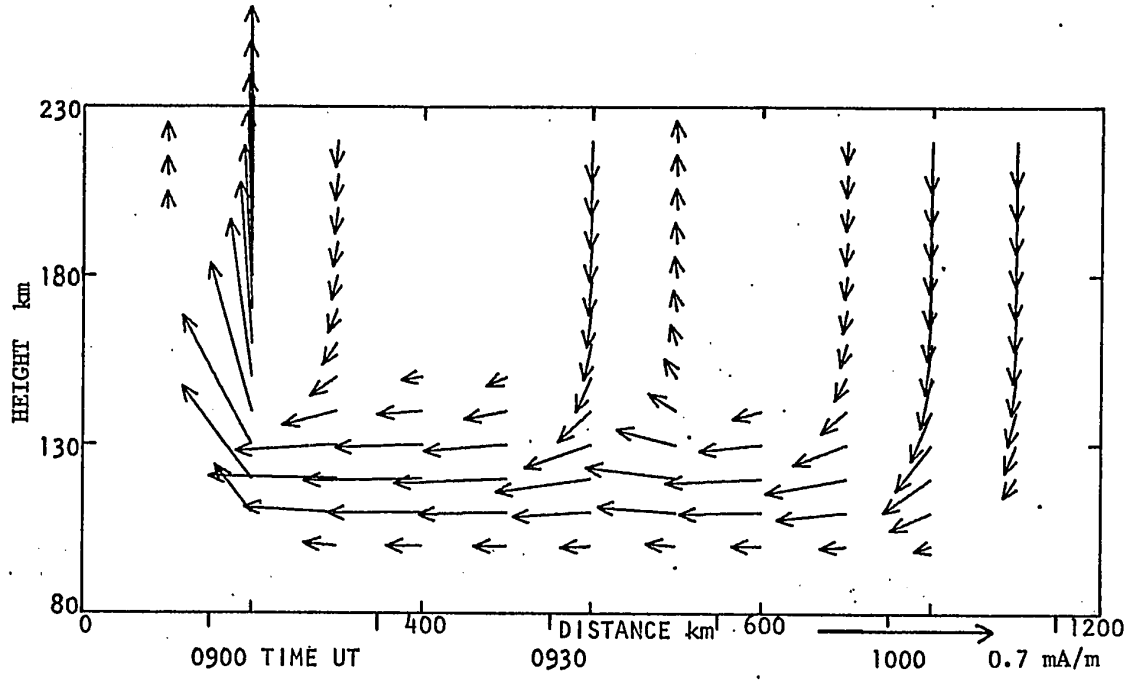

Figure 5.16 The total electrojet and Birkeland field-aligned current in a longitudinal plane or as a function of time. The direction and magnitude of the current is indicated by the arrows.

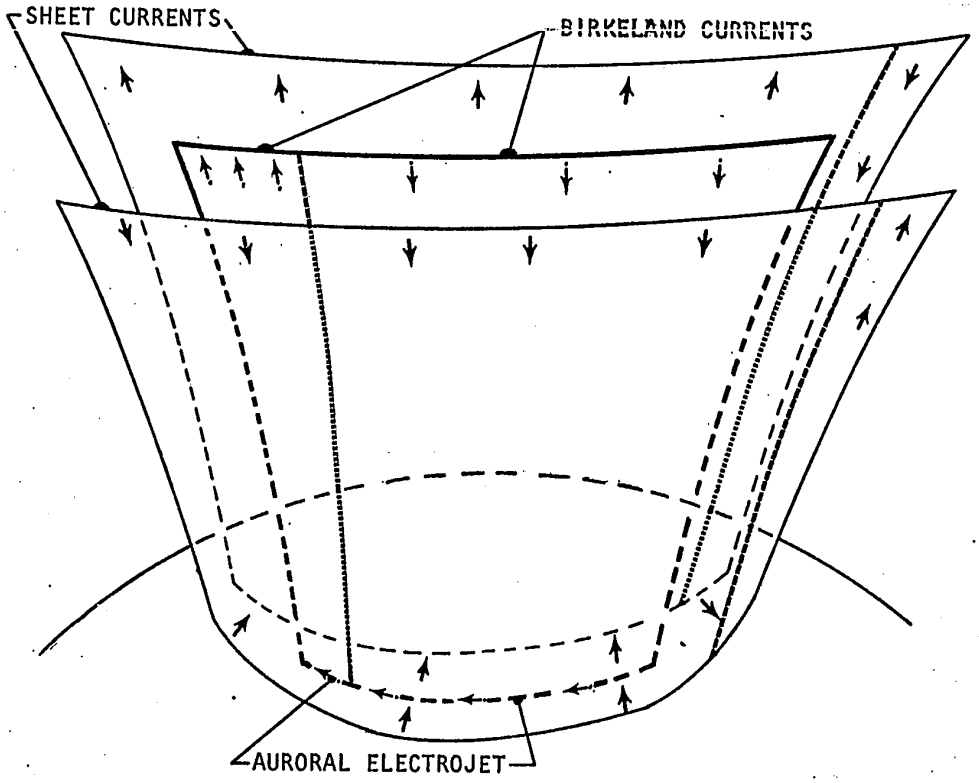

Figure 5.17 The relative positions of the auroral electrojet, linked to a Birkeland current system which is immersed between two antiparallel sheet currents. The whole system is moving westward at 100-300 m/s.

The Birkeland field-aligned current flowing into the ionosphere electrojet occurs during the decay phase of the substorm and is much less intense. The substorm subsides over the period of an hour, during which it's current system may have moved 500 - 1000 km. The field-aligned current density in the decay phase is then $\sim 0.4 \mu A/m^2$ resulting in a negligible field variation at the satellite. The meridional current across the arcs decreases to about 0.1A/m during the decay of the substorm and would result in an $\sim$125 nT disturbance between the sheet currents. In the final section at 1007 UT the meridional current in the ionosphere has changed to a southward direction (Figure 5.13) with a magnitude of 0.05 A/m. It flows only around the northern arc, giving a distance between the field-aligned sheet currents of $\sim$150 km and a resulting magnetic field perturbation of $\sim$60 nT at satellite heights.

The complete system of currents flowing in the ionosphere and along the magnetic field into the magnetosphere is depicted in Figure 5.18 for the substorm of August 3, 1969. The currents have been calculated from appropriate models of the auroral ionosphere, the observed electric fields in the vicinity of the arcs, and from the theoretical models of the current flow across the arcs. The westward electrojet's magnetic field perturbation pattern is similar to that observed along the meridian with induction effects taken into account. The Birkeland field-aligned current has a variation pattern in the eastward magnetic field component consistent with that observed on the ground by the latitudinal array of stations. Finally, the

magnetic field of the antiparallel sheet currents has the same rectangular variation pattern as observed by Amstrong and Zmuda (1970). The magnetic field for the Birkeland current and the partial ring current were calculated using expressions 3.33 - 3.45 and are shown in Figure 5.18. The central meridian of the line current model (Bonnevier et al., 1970) corresponds to ~0907 UT. The contribution of the Birkeland current and the partial ring current to the magnetic perturbation pattern is ~15 nT or ~11% of the maximum perturbation. Correction for this contribution to the observed magnetic field perturbation would reduce the magnitude of the electrojet by a similar amount. The system of currents proposed in this section satisfies present observations but could be supplemented with additional weaker current systems that are not readily detectable. Such currents could result from localized regions of enhanced conductivity or electric fields during auroral and magnetospheric conflagrations.

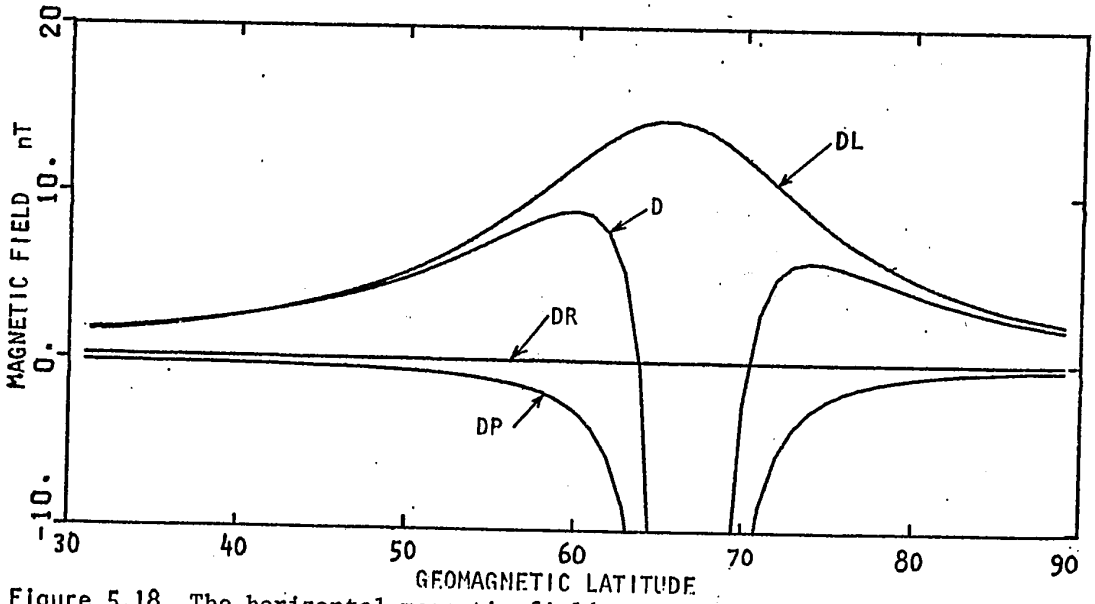

Figure 5.18 The horizontal magnetic field component, H, along the central meridian on the earth's surface of an ionospheric DP, Birkeland DL, and a partial ring current DR as well as their sum D. The line current model has a longitudinal width of 30° and a magnitude of 107 kA.

CHAPTER 6

CONCLUSIONS

A method has been presented to facilitate the study of ionospheric current systems from either theoretical considerations or from observations. Model current systems can be constructed from measurements of the electric field and ionospheric parameters and verified with models from magnetic field analysis. The computer programs developed for calculating and displaying the currents, their parameters and their interactions can be used to determined theoretical current flow during polar magnetic substorms. Determination of the ionospheric conductivity requires a detailed study of the gyro- and collision-frequencies of the ions and electrons. Observations of ionospheric parameters, electric, and magnetic fields are required over a large volume of the auroral region for modelling the current systems. The cause of the auroral electrojet is explained in terms of its driving mechanism, and the resultant magnetic fields predicted from the current systems fit the present observations.

Exact expressions for the gyrofrequency and collision frequency were studied to determine their contributions to the conductivity. The gyrofrequency was calculated from accurate models of the geomagnetic field and from a height dependent mean molecular weight profile. The electron collision frequency was determined from expressions involving each of the constituents of the neutral atmosphere and a nonthermal equilibrium plasma. The negative and positive ion collision frequencies were also calculated from expressions

involving each of the constituents of the neutral atmosphere and a nonthermal equilibrium plasma. The negative and positive ion collision frequencies were also calculated from expressions for each of the height dependent gas constituents of the upper atmosphere and their temperature dependent cross sections for momentum transfer. The neutral atmosphere density and temperature for the collision frequency calculation, were determined as a function of height for the appropriate season, latitude, time and thermosphere. An expression for the electron density in the auroral ionosphere as a function of the height and auroral brightness was developed from theoretical considerations using the electron continuity equation. The expression encompasses the large dynamic range of the electron density during auroral displays, while maintaining a simple and smooth relationship with the auroral brightness and height. This expedient method of obtaining the volume distribution of the electron density from photographs or auroral scanners, significantly simplifies the construction of auroral ionospheres and the observational requirements. Expressions were also determined for the height dependent negative ion density and for the electron temperatures as a function of the height and auroral brightness. The ion temperature was determined from the thermal imbalance between the electrons and neutral particles.

The electric field was determined from observations and from theoretical considerations of the current flow. The electric field was mapped along magnetic field lines to the ionosphere from the point of observation. Electric fields were also determined in the

auroral arcs from assumptions of the continuity of current flow across the arc boundaries.

The auroral cross section in the meridional plane was assumed sufficiently thin so that changes in the current density of the electrojet were negligible. Solution of the field-aligned sheet currents was then obtained by assuming a divergence-free current system. The electric field along the magnetic field lines was calculated from the field-aligned current. The magnetic field of the ionospheric electrojet was calculated along the meridian and this compared favourably with the observed magnetic variations which had been corrected for effects from currents induced in the earth. The electrojet cross sections constructed during the substorm were assumed typical of the spatial extent of the substorm thus permitting the Birkeland field-aligned current to be solved by assuming divergence-free conditions for the electrojet.

A twin arc model of the auroral ionosphere was constructed in order to compare different current systems for simple electric field models. Auroral electrojets driven by only a meridional electric field produced a Hall current three times that of the Pedersen electrojet driven by a direct electric field of the same magnitude. For an electric field constant in strength across the arc, the current density inside the arc is six times that in the surrounding diffuse aurora. Observations indicate the electric field in an arc is considerably less than in the adjacent regions. A Pedersen electrojet was modelled such that the current density

across the arc was constant and equal to that outside the arc, which resulted in a horizontal sheet current flowing westward through the ionosphere. The westward electric field inside the arc was approximately 1/5 that in the diffuse aurora. A polarization electric field in the arc was added to the Pedersen sheet current model and resulted in the current in the arc being enhanced by a factor of 7. The large antiparallel field-aligned currents at the edge of the polarized arc have not been observed and are probably not physically tenable, so the amount of polarization is likely small. Theoretical models of Hall electrojets were also made having reduced electric fields inside the arc. The first model had the same ionosphere and electric field configuration as the Pedersen sheet current model and resulted in twice the current density. The second Hall electrojet model had the meridional current density constant across the arc and resulted in a 25% increase in the current density in the arc. Both Hall current models and the Pedersen sheet current model fit the observations, so the real current system, which could also be a combination of Hall and Pedersen current, could only be resolved by detailed measurements within the arc.

The auroral zone ionosphere is essentially a channel 300 - 700 km wide and extending 1000 km or more from dusk to dawn. The maximum current will flow in the channel when the vector sum of the Pedersen and Hall currents is in the direction of the channel. This occurs when the electric field is 12° west of south for a westward electrojet and 12° east of north for an eastward electrojet and results in an 8% increase in magnitude over a purely Hall current.

Minimum current will flow in the direction of the channel when the Pedersen and Hall currents cancel, which occurs when the electric field is approximately 68° west of north or 68° east of south. The meridional current is maximum for a null electrojet and also results in maximum antiparallel field-aligned currents on either side of the arc region. The field-aligned current results from a decrease in either the conductivity or the driving electric field or from coincident small reductions in both parameters.

The rate of Joule heating from the currents for a small substorm was the same as the heating during the day. A moderate storm has a Joule heating rate six times that of the small substorm and is potentially capable of affecting the meteorology of the upper atmosphere. Current induced winds for the small substorm model were northward at 10 m/s at an altitude of 100 km increasing to 200 m/s above a height of 140 km. The maximum wind and heating rate was not within the arc, but in the large region of auroral glow adjacent to the arc; consequently the whole of the auroral zone ionosphere and upper atmosphere is affected.

Current systems for a substorm were modelled from electric field observations and a theoretical auroral ionosphere to fit magnetic field variations along the same meridian. The main features of the substorm were caused by changes in the electric field direction. The electric field direction before the commencement of the substorm was in the configuration for a minimum electrojet current. During the expansive phase of the substorm the electric field direction

changed to produce a large westward electrojet. The electrojet then consisted of equal contributions from Hall and Pedersen currents. The typical auroral ionosphere model required a small electric field in the arcs to obtain an electrojet consistent with that predicted by ground based magnetic variations. The electrojet model had constant current density across the arcs and was similar to a sheet current approximately 280 km wide and flowing between 100 and 150 km in height. The current flowing in the meridional direction required sheets of field-aligned current on either side of the electrojet for current continuity. The rectangular magnetic field variation observed with orbiting satellites would also result from the antiparallel sheet currents and has similar magnitude and spatial extent as those calculated for the models.

Decreasing conductivity and a gradually weakening electric field characterizes the decay phase of the substorm. The small electric field in the arcs is still required to limit the magnitude of the electrojet to that inferred by magnetic field analysis, which has been corrected for induction to approximately 2/3 of the observed field. The westward component of the electric field remains more constant in time and space than the meridional component. Hence the latter can more readily alter the elctrojet and field-aligned current flow. An ionosphere of low conductivity was required for the final stage of the substorm because the electric fields had decreased little during the substorm and remained in the direction for optimum current flow. The model ionosphere consisted of an auroral free ionosphere surrounding two very weak diffuse aurorae. Within these arcs

the electric field was also reduced so the resultant electrojet would conform with that inferred from magnetic field analysis. The meridional current in the final stage was southward and opposite to that during the decay phase of the substorm; furthermore current reversals in the adjacent field-aligned sheet currents also appear to be necessary.

Electrojet cross sections constructed for the substorm disturbance time were assumed to be representative of a westward travelling current system, which enabled the Birkeland current to be solved from current continuity requirements. The Birkeland current flowed upward during the expansive phase of the substorm with a density and associated magnetic field perturbation 1/4 that of the enclosing antiparallel sheet currents. Birkeland currents flow into the ionosphere during the decay phase of the substorm in the form of a sheet 200 km wide and possibly 800 km long. This Birkeland current density was a factor of 10 less and the magnetic field was approximately 1/5 that of the upward flowing Birkeland current. The downward flowing Birkeland current was also immersed in antiparallel sheet currents which have twice the magnetic field variation as the Birkeland current at satellite heights. However, the magnetic fields of the antiparallel sheet currents cancel outside the region enclosed by the currents, permitting observation of magnetic perturbations of the Birkeland currents.

The polar magnetic substorm analysis required many assumptions; while a crude fit to the observed electric field and magnetic field perturbation pattern was achieved, other related measurements were not available so conclusive proof of the relationship between field-aligned currents and the ionospheric auroral electrojet was not possible. The method of analysis is capable of providing insight into the physics, mechanisms, and dynamics of ionospheric current systems, and field-aligned currents and linkages to the magnetosphere, as well as possible auroral mechanisms. Present technology can incorporate many of the appropriate instruments in one satellite or rocket whose measurements must be coordinated with ground based data for a complete delineation and understanding of the currents. Data obtained from latitudinal arrays are well suited for merging with observation from polar orbiting satellites. The satellite data together with the ground based data could then be expected to provide answers about the configuration of the three-dimensional ionospheric-magnetospheric current system associated with auroral phenomena. The relationship among currents, particle precipitation and electric and magnetic fields together with the behaviour of the ionosphere and upper atmosphere are essential for understanding our inner space environment.

BIBLIOGRAPHY

Aggson, T.L., 1967. Probe measurements of electric fields in space. Aurora and Airglow, ed. by B.M. McCormac, Reinhold Publishing Corp., New York, p.293.

Aggson, T.L., 1969. Results of magnetospheric electric field measurements. Abstracts, Conference on Electric Fields in the Magnetosphere, Rice University, Houston.

Akasofu, S.-I., 1968. Polar and magnetospheric substorms. Springer-Verlag, New York.

Akasofu, S.-I. and S. Chapman, 1967. Geomagnetic storms and auroras. In Physics of Geomagnetic Phenomena, Academic Press, New York.

Arendt, P.R., 1969. Comparison of the topside ionosphere during magnetic storms of various types. Planet. Space Sci., 17, p. 1993.

Armstrong, J.C. and A.J. Zmuda, 1970. Field-aligned current at 110 km in the auroral region measured by satellite. J. Geophys. Res., 75, p.7122.

Atkinson, G., 1970. Auroral arcs: result of interaction of a dynamic magnetosphere with the ionosphere. J. Geophys. Res., 75, p.4746.

Axford, W.I., 1969. Magnetospheric convection. Rev. Geophys. 7, p.421.

Axford, W.I. and C.O. Hines, 1961. A unifying theory of high-latitude geophysical phenomena and geomagnetic storms. Can. J. Phys., 39, p.1433.

Banks, P., 1966. Collision frequencies and energy transfer, electrons. Planet. Space Sci., 14, p.1085.

Banks, P., 1966. Collision frequencies and energy transfer, ions. Planet. Space Sci., 14, p.1105.

Belon, A.E., G.J. Romick and M.H. Rees., 1966. The energy spectrum of primary auroral electrons determined from auroral luminosity profiles. Planet. Space Sci., 14, p.597.

Birkeland, K., 1908. The Norwegian aurora polaris expedition, 1902-03, 1, Sec.1, Christiania.

Birkeland, K., 1913. The Norwegian aurora polaris expedition, 1902-03, 1, Sec. 2, Christiania.

Block, L.P., 1965. On the distribution of electric fields in the magnetosphere, 65-10. Royal Inst. of Technology, Stockholm.

Bonnevier, B., R. Boström and G. Rostoker, 1970. A three-dimensional model current system for polar magnetic substorms. J. Geophys. Res., 75, p.107.

Boström, R., 1964. A model of the auroral electrojet. J. Geophys. Res., 69, p.4983.

Brace, L.H., H.G. Mayr and K.K. Makajan, 1970. A polar maximum of electron concentration at 1000 km altitude. J. Atmosph. Terr. Phys., 32, p.1945.

Bryant, D.A., G.M. Courtier, G. Skovli, H.R. Lindalen, K. Aarsnes and K. Måseide, 1970. Electron density and electron flux in a glow aurora. J. Atmosph. Terr. Phys., 32, p.1695.

Cauffman, D.P. and D.A. Gurnett, 1971. Double-probe measurements of convection electric fields with the Injun-5 satellite. J. Geophys. Res., 76, p.6014.

Champion, K.S.W., 1967. Variations with season and latitude of density, temperature and composition in the lower themosphere. AFCRL, 67-10161.

Chan, K.L. and L. Colin, 1969. Global electron density distributions from topside soundings. IEEE, 57, p.859.

Chapman, S., 1956. The electrical conductivity of the ionosphere: A review, Nuovo Cemento, 4(10), Suppl. 4, p.1385.

Chapman, S. and J. Bartels, 1940. Geomagnetism. Oxford Univ. Press (Clarendon), London.

Cole, K.D., 1971. Electrodynamic heating and movement of the thermosphere. Planet. Space Sci., 19, p.59.

Committee on the Extension of the Standard Atmosphere, U.S. Standard Atmosphere Supplements, 1966. Government Printing Office, Washington, D.C.

Dalgarno, A., 1961. Charged particles in the upper atmosphere. Ann. Geophys., 17, p.16.

Dalgarno, A. and J.C.G. Walker, 1967. Ion temperatures in the topside ionosphere. Planet. Space Sci., 15, p.200.

Danilov, A.D., 1970. Chemistry of the ionosphere. Plenum Press, New York.

Eather, R.H. and S.B. Mende, 1971. Airborne observations of auroral precipitation patterns. J. Geophys. Res., 76, p.1746.

Föppl, H., G. Haerendel, L. Haser, R. Lüst, F. Melzner, B. Meyer, H. Neuss, H.-H. Rabben, E. Rieger, J. Stocker and W. Stöffregen, 1968. Preliminary results of electric field measurements in the auroral zone. J. Geophys. Res., 73, p.21.

Fukushima, N., 1969. Equivalence in ground geomagnetic effect of Chapman-Vestine's and Birkeland-Alfven's electric current-systems for polar magnetic storms. Rep. Ionos. Space Res., Japan, 23, p.219.

Gattinger, R., 1971. Private Communication. National Research Council of Canada, Ottawa.

Hinteregger, H.E., L.A. Hall and G. Schmidtke, 1965. Solar XUV radiation and neutral particle distribution in July 1963 thermosphere. Space Research, North-Holland, Amsterdam.

Hochstim, A.R., 1969. Kinetic processes in gases and plasmas. Academic Press, New York.

Holt, E.H. and R.E. Haskell, 1965. Plasma dynamics. The MacMillan Co., New York.

Hruška, A., 1971. Motions of the "cold" magnetospheric plasma and the polarization effect. Preprint, HAO, Boulder, Colorado, U.S.A.

Hunten, D.M., E.G. Rawson and J.K. Walker, 1963. Rapid measurement of N_2^+ rotational temperatures in aurora. Can. J. Phys., 41, p.258.

IBM Application Program, System/360 Scientific Subroutine Package, Version III, GH 20-0205-4, 1970.

Jacchia, L.G., 1964. Static diffusion models of the upper atmosphere with empirical temperature profiles. Smithsonian Astrophys. Obs., 170

Jacobs, K.G., R. Kist and K. Rawer, 1969. The electron density profile of auroral layers as observed with ESRO rockets at Kiruna. Space Res. IX, p.246, North Holland, Amsterdam.

Johnson, D.W. and A. Kavadas, 1963. A rocket-born electric field probe. Can. J. Phys., 41, p.1980.

Kisabeth, J.L. and G. Rostoker, 1971. Development of the polar electrojet during magnetic substorms. J. Geophys. Res., 76, p.6815.

Kisabeth, J. L., 1972. The dynamical development of the polar electrojets. Ph.D Thesis, University of Alberta.

Lackman, R.L., 1970. Streamline program description. National Center for Atmospheric Research, Boulder, Colorado.

Lezniak, T.W. and J.R. Winckler, 1970. Experimental study of magnetospheric motions and the acceleration of energetic electrons during substorms. J. Geophys. Res., 75, p.7075.

Large, D.B. and J.R. Wait, 1968. Theory of electromagnetic coupling phenomena in the earth-ionosphere cavity. J. Geophys. Res., 73, p.4335.

Maier, E.J. and B.C. Narasinga Rao, 1970. Observations of the suprathermal electron flux and the electron temperature at high latitudes. J. Geophys. Res., 75, p.7168.

Matsushita, S., 1967. Solar quiet and lunar daily variation fields. In Physics of Geomagnetic Phenomena, Academic Press, New York.

Matsushita, S. and J.D. Tarpley, 1970. Effects of dynamo-region electric fields on the magnetosphere. J. Geophys. Res., 75, p.5433.

Mayaud, P.N., 1967. Calcul préliminaire d'indices Km Kn et Ks ou am, an et as, measures de l'activite magnetique á l'échelle mondiale et dans les hémisphéres Nord et Sud. Annales de Geophysique, 23, no.4.

McNamara, A.G., 1969. Rocket measurements of plasma densities and temperatures in visual aurora. Can. J. Phys. 47, p.1913.

Mozer, F.S., 1970. Electric field mapping in the ionosphere at the equatorial plane. Planet. Space Sci., 18, p.259.

Mozer, F.S., 1971. Power spectra of the magnetospheric electric field. J. Geophys. Res., 76, p.3651.

Mozer, F.S. and U.V. Fahleson, 1970. Parallel and perpendicular electric fields in an aurora. Planet. Space Sci., 18, p.1563.

Mozer, F.S. and R.H. Manka, 1971. Magnetospheric electric field properties deduced from simultaneous balloon flights. J. Geophys. Res., 76, p.1697.

Mozer, F.S. and R. Serlin, 1969. Magnetospheric electric field measurements with balloons. J. Geophys. Res., 74, p.4739.

Nier, A.O., J.H. Hoffman, C.Y. Johnson and J.C. Holmes, 1964. Neutral composition of the atmosphere in the 100 to 200 kilometer range. J. Geophys. Res., 69, p.979.

Norton, R.B. and J.A. Findlay, 1969. Electron density and temperature in the vicinity of the 29 September 1967 middle latitude red arc. Planet. Space Sci., 17, p.1867.

Pitts, D.E., 1968. A computer program for calculating model planetary atmospheres. NASA, TN D-4292.

Potter, W.E., 1970. Rocket measurements of auroral electric and magnetic fields. J. Geophys. Res., 75, p.5415.

Price, A.T., 1967. Electromagnetic induction within the earth. In Physics of Geomagnetic Phenomena, Academic Press, London.

Quinn, T.P. and J.S. Nisbet, 1965. Recombination and transport in the nighttime F layer of the ionosphere. J. Geophys. Res., 70, p.113.

Ratcliffe, J.A., 1956. The formation of ionospheric layers F-1 and F-2. J. Atmosph. Terr. Phys., 18, p.260.

Reber, C.A. and M. Nicolet, 1965. Investigation of the major constituents of the April-May 1963 heterosphere by Explorer XVII satellite. Planet. Space Sci., 13, p.617.

Reddy, C.A., M. Mukunda Rao and S. Matsushita, 1969. Rocket observations of electron densities in the night-time auroral E-region at Fort Churchill, Canada. Planet. Space Sci., 17, p.617.

Rees, M.H., 1969. Auroral electrons. Space Sci. Rev., 10, p.413.

Rees, M.H. and J.C.G. Walker, 1968. Ion and electron heating by auroral electric fields. Annal de Geophys., 24, p.193.

Rishbeth, H. and O.K. Garriott, 1969. Introduction to Ionospheric Physics, Academic Press, New York.

Rostoker, G., 1966. Midlatitude transition bays and their relation to the spatial movement of overhead current systems. J. Geophys. Res., 71, p.79.

Sampson, J.C., 1971. Spectral characteristics of pc4 and pc5 geomagnetic micropulsations. Ph.D. Thesis, University of Alberta, Edmonton.

Serson, P.H., 1957. An electrical recording magnetometer. Can. J. Phys., 35, p.1387.

Stening, R.J., 1970. Joule heating and the excitation of thermo-tidal modes in the dynamo region. Planet. Space Sci., 18, p.423.

Stratton, J.A., 1941. Electromagnetic theory. McGraw-Hill, New York.

Stubbe, P. and S. Chandra, 1970. The effect of electric fields on the F-region behaviour as compared with neutral wind effects. J. Atmosph. Terr. Phys., 32, p.1909.

Swider, W., 1971. The ratio of negative ions to electrons in the D region. Transactions, A.G.U., 52, p.304.

Wagner, C.-U., 1968. The electrical conductivity in the region from 105 to 125 km. Planet.Space Sci., 16, p.353.

Walker, J.C.G., 1970. Electric field excitation of $O_2(^1\Delta_g)$ in auroras. Planet. Space Sci., 18, p.1043.

Walker, J.C.G. and M.H. Rees, 1968. Ionospheric electron densities and temperatures in aurora. Planet. Space Sci., 16, p.459.

Walker, J.K., 1964. Space-time associations of the aurora and magnetic disturbance, J. Atmosph. Terr. Phys., 26, p.951.

Warren, E.S., 1969. The topside ionosphere during geomagnetic storms, IEEE, 57, p. 1029.

Watanabe, T., 1962. Law of electric conduction for waves in the ionosphere. J. Atmosph. Terr. Phys., 18, p.135.

Weaver, J.T. and R. Skinner, 1960. A theory of ionospheric currents associated with aurora, parts 1 and 2. Can. J. Phys., 38, p.1089.

Wescott, E.M., J.D. Stolarik and J.P. Heppner, 1969. Electric fields in the vicinity of auroral forms from motions of barium vapor releases. J. Geophys. Res., 74, p.3469.